MICROFLUIDIC APPROACHES FOR DISEASED CELL SEPARATION FROM BLOOD

HOU HAN WEI

B.Eng. (Hons.), National University of Singapore, 2008

A THESIS SUBMITTED

FOR THE DEGREE OF DOCTOR OF PHILOSOPHY

DEPARTMENT OF BIOENGINEERING

NATIONAL UNIVERSITY OF SINGAPORE

2012

Dedicated to my

family and wife Sook Hwa.

ACKNOWLEDGEMENTS

First and foremost, I would like to thank my advisor Dr. Lim Chwee Teck for his able guidance and continual support during this work. He has not only been instrumental in the timely completion of my PhD work, but his constant belief in my research throughout the years has motivated me tremendously.

I would also like to express my gratitude to my co-advisor, Dr. Han Jongyoon from MIT. The countless constructive suggestions, technical advices and research directions he provided me over the years has trained me to become more analytical and technically-sound as a researcher.

At BioSystems and Micromechanics (BioSyM) IRG, I am grateful to Dr Ali Asgar S. Bhagat for supervising and mentoring me during my research years. It was fun and enjoyable working together and constantly exploring new ideas. He has been a great friend, both in and outside the lab.

In addition, I would also like to extend my sincere regards to other colleagues at BioSyM IRG for their continual support and friendship over the years, especially Dr. Narayanan Balasubramanian, Dr. Shi Hui, Dr. Li Zirui, Wendee, Sei Hein, Chin Wen, Jacky and Guofeng. It is a great pleasure working with all these wonderful individuals.

In Singapore, I thank our colleagues at Infectious Disease (ID) IRG and Global Enterprise for Micro Mechanics and Molecular Medicine (GEM4) lab including Dr. Lui Wai Yi Lena, Dr. Li Ang, Siew Chin and Xiaofeng for the substantial assistance and support they provided throughout my PhD. From Nanobiomechanics lab, I would like to acknowledge Dr. Li Qingsen, Dr. Mendoz Earnest, William, Man Chun, Surabhi, Laiyi and Yeong Yuh for their helpful discussions, support and friendship.

At MIT, I am extremely appreciative to members of the Micro/Nanofluidic BioMEMs group for their help in wafer fabrication and their warm hospitality during my stay at MIT. Dr. Gan Hiong Yap, in particular, has provided insightful suggestions for the sepsis project and has been a fantastic friend. I would also like to thank our collaborators at MIT, Drs. Ming Dao and Monica Diez-Silva for the malaria separation project, and Dr. Jacquin Niles and his graduate student, Christina Birch in the aptamer project.

Last but not least, I am grateful to my family, parents Hou Wan Hoo and Tan Chek Eng, brothers Han Siang and Han Tiong and sister Wai Ling for their unconditional love and unwavering support. I would also like to sincerely thank my wife Sook Hwa, for always being supportive, encouraging and believing in me. She definitely plays a big role in making my PhD journey more smooth-sailing and enjoyable.

Lastly, I would like to acknowledge Singapore-MIT Alliance for Research and Technology (SMART) for funding my research work and provision of the SMART graduate fellowship for financial support.

ABSTRACT

Of the ~5 billion cells per milliliter of blood, red blood cells (RBCs) account for >99% of all cellular components suspended in protein-rich plasma. Besides blood constituents, pathogenic microorganisms or diseased cells are also present in peripheral blood in different diseases, which are of clinical significances and important for fundamental research. However, presence of the large RBCs background not only complicates the elimination of diseased components (in sepsis and malaria), but also makes disease diagnosis such as detection of rare circulating tumour cells (CTCs) in blood (in cancer patients) largely ineffective. In this work, we address these issues and demonstrate that physical biomarkers (size, deformability) can be used for effective diseased cell separation from whole blood using microfluidics, leveraging on its many inherent advantages such as high sensitivity and spatial resolution, short processing time and low device cost.

We first developed a novel, high-throughput size/deformability-based microfluidic separation technique based on the microcirculatory phenomenon of leukocyte margination and applied it in sepsis (bacteria separation) and malaria (malaria-infected RBCs separation) disease. Next, we employed the principles of inertial microfluidics to demonstrate a continuous size-based CTCs isolation from blood using two different channel designs: 1) a high aspect ratio microchannel patterned with an expansion and contraction array with a “pinching” region at the channel end and 2) a two-inlet, two-outlet spiral microchannel (aptly termed as *Dean Flow Fractionation (DFF)*). Good separation performances (>80% efficiency) was achieved in all developed devices and the microfluidic approaches presented here also offer distinct advantages over current microfluidic blood separation techniques such as the ability to process whole blood directly, high-throughput separation and minimal clogging issues.

Lastly, as the developed microdevices are based on passive separation techniques (no external force field required for functionality) and allows a continuous collection of sorted

cells, we envision that these simple, efficient and cost-effective microfluidic blood separation platforms will be imperative in realizing point-of-care (POC) diagnostics and invaluable for many downstream clinical and biological applications.

Table of Content

LIST OF FIGURES

LIST OF TABLES

LIST OF SYMBOLS

a_p	=	Particle diameter	
AR	=	Aspect ratio	AR= h/w
C_L	=	Lift coefficient	
De	=	Dean number	$De= Re(\sqrt{(D_h /2R)})$
DC	=	Dean cycle	
D_h	=	Microchannel hydraulic diameter	$D_h = 2w \times h/(w + h)$
F_D	=	Lateral Dean drag force	
F_L	=	Net inertial force	
G	=	Shear rate of the fluid	$G = U_{max}/D_h$
h	=	Microchannel height	
L_c	=	Microchannel length	
L_{DC}	=	Dean cycle migration length	
ΔP	=	Applied pressure drop	
Q	=	Fluidic flow rate	
R	=	Radius of curvature of spiral	
Re	=	Reynolds number	$Re= \rho U_f D_h/\mu$
R_h	=	Hydrodynamic resistance	
U_{De}	=	Average Dean velocity	
U_f	=	Average primary channel velocity	
U_{max}	=	Maximum channel velocity	
w	=	Microchannel width	
μ	=	Fluid dynamic viscosity	
ρ	=	Fluid density	

1 Introduction

1.1 Blood composition

Blood is one of the most important biological fluids in our body and accounts for 7-8% of the body weight with an average volume of ~5 liters in human adults. It is responsible for many homeostatic functions; serving as a primary transport medium for oxygen and nutrients delivery throughput the body, removal of metabolic wastes such as carbon dioxide and urea, and regulating body pH and temperature. In addition, the circulation of immune cells through the vascular network and presence of plasma proteins (albumins and antibodies) help to defend against foreign bodies as well as repair tissue damage through formation of blood clot. As blood contains a myriad of information about the functioning of the human body, blood analysis has been a primary diagnostic test in our healthcare system where abnormalities and variations in the number, size, or maturity of blood cells are often used to indicate an infection or disease process [1].

Blood comprises ~45% volume fraction of cellular components suspended in protein-rich plasma. Red blood cells (RBCs) constitute the vast majority of all blood cells, followed by platelets and leukocytes (or white blood cells (WBCs)). For every 1000 RBCs, there are approximately 100 platelets and 1 leukocyte (**Table 1**). All blood cells are derived from hematopoietic stem cells in the bone marrow through a process known as hematopoiesis and approximately 10^{11}–10^{12} new blood cells are produced daily in healthy adults to maintain steady state levels in the peripheral circulation. The following section provides a brief introduction for each type of blood cell component.

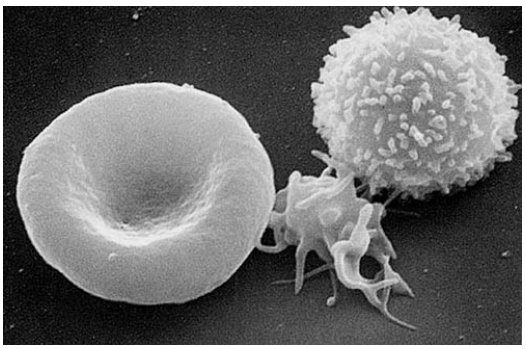

Figure 1.1. Scanning electron microscope (SEM) image of a normal RBC (left), platelet (centre) and leukocyte (right). (Source: http://web.ncifcrf.gov/)

Table 1. Comparisons between different types of blood cell.

Cell type	Average/ mL	Shape	Size (μm)
Red blood cells	~5×10^9	Biconcave disk	7-8 μm diameter 2 μm thickness
Platelets	2-5×10^8	Irregularly –shaped cell fragments	2-3 μm
Leukocytes	4-11×10^6	Spherical	7-15 μm

Red blood cells (RBCs)

A healthy RBC at rest has a biconcave shape of average diameter 7-8 μm and 2 μm in thickness (Figure 1.1). The proportion of blood occupied by red blood cells is known as hematocrit and ranges from 40-45%, depending on gender. RBCs are non-nucleated and contain large amount of hemoglobin enveloped by a thin membrane consisting of a phospholipid bilayer and an underlying two-dimensional spectrin network [2, 3]. As a consequence of the viscoelastic membrane and high surface area-to-volume ratio, RBCs are highly deformable which facilitate large reversible deformations as they transverse through small capillaries (2-3 μm) during circulation. Reticulocytes are immature RBCs with RNA contents and account for ~0.8-1% of RBCs. They are slightly larger (~8%) and less deformable than mature RBCs with a more irregular/convoluted shape. Upon release from bone marrow, reticulocytes will typically circulate in the bloodstream for about a day before maturing into adult RBCs.

Leukocytes (WBCs)

Leukocytes exist both in blood circulation and lymphatic system in our body and their primary role is to provide immune protection against foreign materials and infectious agents. Based on appearance, there are five classes of leukocytes namely (in terms of decreasing abundance); neutrophils, lymphocytes, monocytes, eosinophils, and basophils. Leukocytes vary in shapes and sizes (7-15 μm) with numerous membrane folding ("microvilli") to facilitate their deformations into small capillaries [4]. As leukocytes are nucleated and possess

a three-dimensional (3D) cytoskeleton in the cytoplasm, they are stiffer than RBCs which can have a significant influence on blood flow, especially in the microvasculature [5].

Platelets (thrombocytes)

Platelets are small, non-nucleated, irregularly-shaped cell fragments (2-3 μm) derived from fragmentation of megakaryocytes, a type of bone marrow cell. They are ~10 × stiffer than RBCs due to presence of a 3D cytoskeletal network and circumferential microtubule [6, 7]. Their main role is to maintain hemostasis by plugging leakages in blood vessel walls and initiating the coagulation cascade through secretion of multiple growth factors when activated.

1.2 Blood rheology

Blood rheology (or hemorheology) is the study of blood flow and its interactions with the surrounding environment in both macro- and microcirculation. As vessel topography varies greatly between arterioles, capillaries and veins, this leads to a wide distribution in blood pressure and velocity because of a decrease in vessel size, which corresponds to an increase in flow resistance [8] (Figure 1.2).

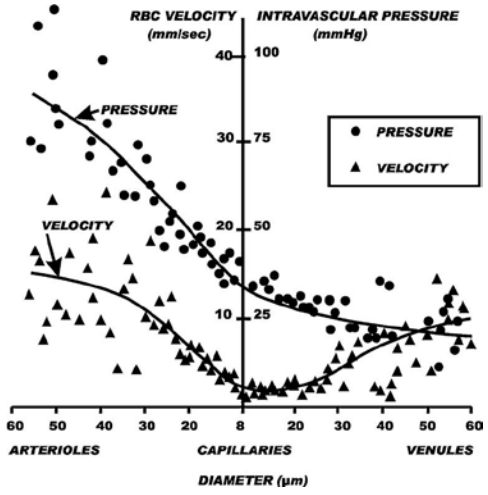

Figure 1.2. Intravascular pressure and RBC velocity distribution at different parts of the blood circulation system [8].

Due to the high volume fraction of RBCs in blood, rheological properties of blood are strongly influenced by the dynamics of RBCs. At post capillary venules where shear rates are

typically lowest, RBCs tend to adhere to each other in the presence of macromolecules (e.g. fibrinogens) to form rouleaux or aggregates which increase the blood viscosity. High shear rates (> 1 dyn/cm^2) break up these aggregates, resulting in a decrease in blood apparent viscosity [9]. In large vessels (>500 µm vessel diameter) with high flow velocities, blood is modelled as a homogenous, nearly Newtonian fluid with constant apparent viscosity [10]. On the scale of microcirculation (<500 µm vessel diameter) however, blood displays complex rheological behaviour due to the finite size of RBCs and their interactions with the channel wall. In such vessels, blood is considered as a multiphase fluid (RBCs in plasma) which exhibits unique flow characteristics such as Fåhræus effect (dynamic reduction in tube hematocrit) and Fåhræus–Lindqvist effect (decrease in apparent viscosity) with decreasing vessel diameter (Figure 1.3) [11, 12]. These effects are primarily attributed to the redistribution of RBCs across the channel with more RBCs flowing at the channel centre, leaving a layer of cell-free region next to the vessel wall [13].

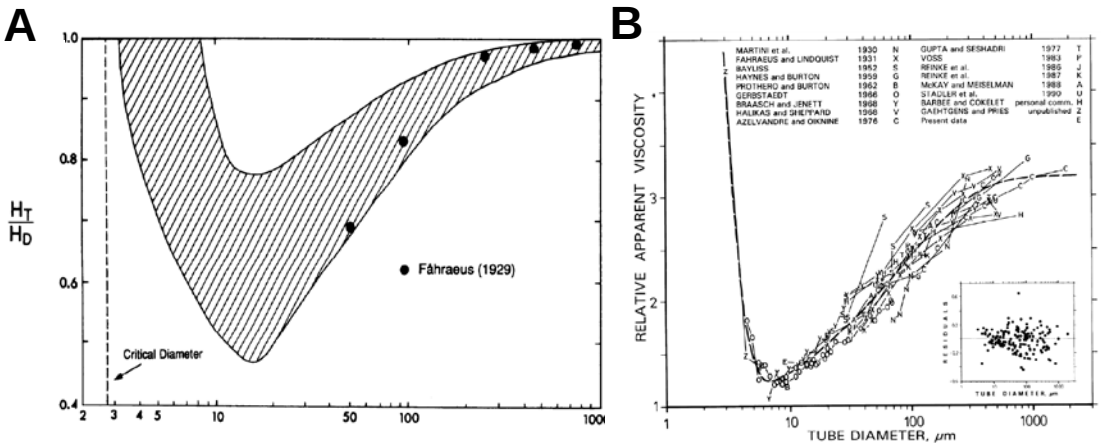

Figure 1.3. (**A**) Fåhræus effect- Reduction in tube hematocrit (H_T) with decreasing vessel size at physiological feed hematocrit (H_D) of 40-45%. Below 10 µm diameter, H_T/H_D increases towards unity again. Cross-hatched region contains all literature data with points of Fåhræus data indicated [13]. (**B**) Fåhræus–Lindqvist effect- Strong reduction in blood apparent viscosity with decreasing tube diameter from 10 µm to 2000 µm. For diameters < 10 µm, an inverse relationship is observed due to RBC deformation through the channel which results in higher flow resistance and viscosity [14].

1.3 Blood-related diseases

Blood-borne or blood-related diseases is a serious health problem not only because blood is constantly circulating throughout the body, but presence of the large RBCs background also

make disease detection and elimination of diseased cells or infectious agents largely ineffective. In this section, we highlight several blood-related diseases which remain a major problem in clinical settings and will be the focus in this work.

1.3.1 Sepsis

Sepsis is an adverse systemic inflammatory response caused by microbial infection in blood. It is the primary cause of death in intensive care units (ICU) (~751,000 cases in United States annually) with overall mortality between 28–50% [15]. Upon infection, the innate immune system responds by initiating inflammatory pathways and leukocyte recruitment to the site of infection to combat the infectious agents. However, excess production of cytokines and inflammatory mediators can trigger a widespread and uncontrolled inflammation, which can lead to septic shocks or deaths in severe cases as a result of multiple organ dysfunction [16].

1.3.2 Malaria

Malaria is one of the most severe parasitic blood-borne diseases with half of the world's population (3.3 billion) at risk and an estimated 1 to 2 million deaths annually [17]. Lack of resources in poorer countries further worsens the situation by imposing a major economic burden to tackle the disease in these affected countries [18, 19]. Of the four types of human malaria species, *Plasmodium (P.) falciparum* is the most deadly and *P. falciparum*-infected red blood cells (*i*RBCs) undergo various developmental stages (ring, trophozoite and schizont stages) in a 48-hour intraerythrocytic cycle. During this period, the parasites continuously remodel the host RBCs and export certain parasitic proteins that make *i*RBCs membranes more adhesive, thereby promoting cytoadherence [20, 21] and a progressive stiffening of *i*RBCs membrane as the parasites mature [22-26]. These parasite-induced morphological changes compromise the microcirculation [27-29] and can manifest into pathophysiological outcomes such as anaemia, metabolic acidosis or organ failure in the case of severe malaria [19, 28, 30].

1.3.3 Cancer

Cancer, one of the leading causes of death worldwide, occurs when there is a rapid and uncontrolled growth of abnormal cells. Cancerous cells are known to be more deformable than their normal counterparts which give rise to their ability to invade and migrate during metastasis (spreading of cancer) [31-34]. Presence of circulating tumor cells (CTCs) in blood is an important intermediate step in cancer metastasis and accounts for ~90% of all cancer-related deaths [35]. Clinical reports have shown that CTCs enumeration in peripheral blood from patients with metastatic carcinomas is associated with disease stages [36, 37] and can be used for clinical evaluations such as monitoring therapeutic treatment response [38]. However, as CTCs are extremely rare (~1-100 CTCs/mL of whole blood) with highly heterogeneous morphologies and molecular signatures, isolation of CTCs from blood has been a huge technical challenge, making their use as a biomarker in clinical management greatly limited [39].

1.4 Cell separation in microfluidics

Cell separation is an important sample preparatory step in many biological assays to isolate or enrich cells-of-interest from complex samples to enhance signal-to-noise ratio as well as to minimize undesirable, non-specific interactions with other cell types. In particular, separation and isolation of rare cell populations from highly heterogeneous suspensions (e.g. blood) is essential for many applications ranging from disease diagnostics to conducting fundamental studies [40, 41]. Conventional macroscale cell separation techniques include density gradient centrifugation, membrane-based filtration, fluorescence-activated cell sorting (FACS) and magnetically-activated cell sorting (MACS). Density gradient centrifugation is mostly limited to blood fractionation and separation of viruses and subcellular components. Membrane filtration is based on physical sieving of larger cells and generally suffers from clogging issues and separation applications are further limited by membrane pore size. The current method of choice for cell identification and separation is FACS in which fluorescence-

labelled cells are identified by light scattering or the presence of fluorescence signal. Target cells which are individually isolated into droplets of around 70 μm are analyzed by a detector and deflected by switching tangential electric fields to different buckets for sorting. In MACS, magnetic beads coated with specific recognition molecules (antibodies) are first incubated with the sample to allow binding between the magnetic beads and target cells via antibody–antigen interaction [42]. The desired cell subpopulation is then separated using either a strong magnetic field gradient or magnetic separation columns. This is often termed as Magnetically Actuated Cell Sorter (MACS™), a trademark of Miltenyi Biotec GmbH Company which provides commercial solutions for magnetic cell sorting. Although both FACS and MACS systems offer numerous advantages such as single cell sensitivity, high-throughput sorting and multiplexed analysis for multiple parameters [43], major technical drawbacks include complex operation procedures, contamination issues, poor cell viability and high equipment cost. Therefore there is a need to develop new methodologies which can address these aforementioned issues and remain comparable to FACS/MACS in terms of sensitivity/resolution.

With advancement in silicon microfabrication and focus in genomics research in 1980s which requires new analytical tools with higher sensitivity and resolution, there has been a rapidly growing interest in microfluidics technology (a.k.a Lab-on-a-Chip (LOC) or Micro Total Analysis System (μTAS)) as an approach to overcome these challenges. Microfluidics is a multidisciplinary field defined as the science of studying fluid flow at microscale level and development of miniaturized systems that exploit the unique physics emergent at these small scales [44]. Microfluidics is well suited for biological studies because of its small length scale which allows better control of cellular microenvironment and rapid measurements at single-cell resolution [45-48]. Compared to macro-scale cell separation methods which usually require expensive and bulky equipments, microfluidics has also emerged as an attractive alternative for cell sorting applications because of numerous advantages such as (i) high throughput, (ii) reduced sample and reagent volumes, (iii) faster processing time, (iv) high

sensitivity and spatial resolution, (v) low device cost and (vi) increased portability [43]. Moreover, miniaturization and integration of cell separation into microfluidic devices serves as a useful platform in portable point-of-care (POC) medical systems for disease diagnosis and monitoring. This will be especially important in regions where there is a lack of well-equipped clinical labs and skilled personnel [49].

1.5 Physical biomarkers for cell separation

Cell surface markers are often used to separate different cell types for immunophenotyping using FACS and MACS. This works extremely well for common and established cell types which have well-studied surface markers and homogenous surface marker expressions across the cell population. However, problems arise due to heterogeneities in surface marker expressions in certain cell types such as CTCs and stem cells and the lack of suitable surface markers for specific cell subpopulation greatly limit the separation operation [50], which advocates the need for other useful separation biomarkers.

Microfluidic cell sorting techniques take advantages of the disparities in the intrinsic properties of different cell populations to achieve separation. As mentioned earlier, diseased cells such as *i*RBCs and cancerous cells are often associated with molecular changes in cytoskeletal and membrane composition and organization, leading to physical differences in cell size, shape and deformability [51-53]. These can be readily exploited for cell sorting and isolation purposes for clinical and biological applications. A key advantage of using physical biomarkers for cell separation is the simplicity in microfluidic design and it does not require immuno-labelling or the presence of cell-specific surface markers to achieve separation. Hence, this approach is faster without sample incubation time and can be readily used to isolate rare cells that do not express known markers. Furthermore, no chemical or biological modifications are needed which makes it more economical and will be extremely useful in resource-poor settings.

1.6 Passive cell sorting in microfluidics

Microfluidic cell separation techniques can be broadly classified as active and passive separation techniques. Active separation techniques include working principles which rely on an external force field (electric field, magnetic field, and ultrasonic acoustic resonance) to function and common examples include fluorescence-based sorting (miniaturised FACS) [54-56], magnetophoresis/ magnetic sorting [57-59], dielectrophoresis [60-63], acoustophoresis [64, 65] and optical sorting [66]. Major limitations for active separation include low throughput, and sample preparation is usually required to resuspend the cell mixtures in suitable "conductive" buffer prior separation. Device fabrication is also complex due to integration of external field source into the device and this makes them difficult to integrate with other LOC systems.

For passive separation, the techniques do not require additional energy sources or equipment and rely only on channel geometry and hydrodynamic forces. Here, we focus on passive cell sorting techniques due to their inherent advantages such as higher throughput and design/setup simplicity (**Table 2**). In the following sections, various passive separation techniques (with an emphasis on physical biomarkers) will be discussed and comparisons between these techniques will be summarized in terms of their separation characteristics such as throughput, efficiency and sensitivity etc (**Table 3**).

Table 2. Comparisons between active and passive cell separation techniques.

	Active	Passive
Throughput	*10^2-10^4 cells/min*	*10^3-10^7 cells/min*
Experimental setup/ Device operation	*Complex*	*Simple*
Operation mode	*Batch/ Continuous*	*Continuous*
Channel design	*Complex*	*Simple*
Device versatility	*Yes*	*No*
Sample preparation	*Yes*	*Minimal*
Sorted cell viability	*Mostly dead*	*Mostly alive*

1.6.1 Pillar and Weir structures

The use of pillar structures is attractive for size and deformability based cell sorting. Using arrays of micro-pillar structures, Huang *et al.* described a novel method of continuous separation based on "deterministic lateral displacement" (DLD) of micron sized particles with separation resolution less than 20 nm [67] and the same group later demonstrated blood fractionation using the same technique (Figure 1.4A) [68]. By varying the inter-pillar distances and row to row shift, blood cells can be continuously separated into different outlets in a single pass through the device. However, the presence of large number of obstructions may lead to channel clogging and cell deformability could also blur the size selectivity/resolution.

Besides using carefully-designed pillar structures to deflect cells into different paths, micropillar arrays have also been used to physically isolate/trap CTCs from blood [69, 70] and also in leukapheresis [71]. Sethu *et al.* showed leukocytes depletion from whole blood without channel clogging, offering the possibility for leukocyte-depleted blood to be returned to the donor (Figure 1.4B) [71]. Using a similar approach, larger and stiffer CTCs were isolated with different gap sizes [69, 70] and the overall simplicity of pillar design makes the technique attractive for various cell sorting applications.

Weir structures are another common type of microstructure used to physically separate cells. Gaps are created in between weirs and the top cover to impede larger cells while allowing smaller cells to go through. Using a weir gap size of 3.5 μm, Wildings *et al.* successfully isolated leukocytes from blood [72] as shown in Figure 1.4C. The major drawback of such a direct filtration scheme is the clogging issues that may interfere with the separation process due to the processing of large sample volumes. As weir filters are perpendicular to the flow, larger cells may build up over time, leading to obstructions and drop in separation efficiency. To address this limitation, Chen *et al.* designed microfluidic devices with weirs structures

placed parallel to the main flow (Figure 1.4C) [73]. However, such mechanical filtration systems that separate cells by geometrical differences are less versatile as they would require design variations for different samples. Furthermore, reported studies have shown limited efficiency in the target cell isolation [72], although sufficient for carrying out further downstream assays.

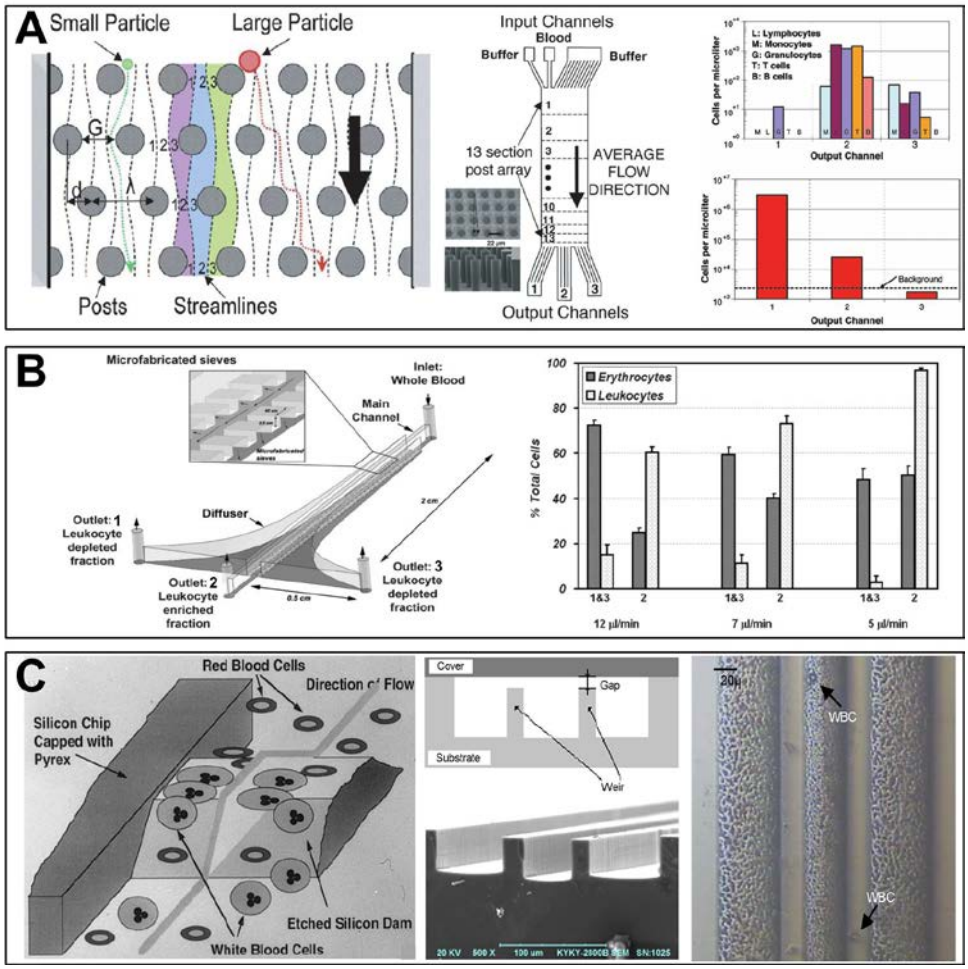

Figure 1.4. (**A**) Separation using deterministic lateral displacement. Schematic illustrating the separation principle by deterministic lateral displacement technique. Cells with diameter smaller than the critical diameter (green circle) stay within the flow streamlines, while larger cells (red circle) are displaced to the right at each obstacle. (*center*) Schematic of the fractionating device used for separating the blood components using DLD. (*right*) Leukocyte and RBC concentration at the three outlets [68]. (**B**) Schematic design of microfluidic device for leukocyte depletion using pillar-based diffusive filter. (*right*) Blood separation results indicating efficient depletion of leukocytes from blood at outlets 1 and 3 at low flow rates [71]. (**C**) Physical based separation using weir structures. (*left*) Schematic of a weir-based filter with 3.5 µm gap between the etched silicon dam and channel top for size-based cell separation. Biconcave RBCs flow through the dam structures easily while the bigger WBCs are filtered out [72, 73]. (*center*) A cross-flow based cell separation design using weir structures as size filters. (*right*) Device image after filtration illustrating the clear separation of white blood cells from blood [73].

1.6.2 Pinched Flow Fractionation

Pinched flow fractionation (PFF) is a novel hydrodynamic chromatographic technique introduced by Yamada *et al.* for continuous size-based cell separation [74]. Taking advantage of the inherent laminar flow properties in microfluidics, a dilute sample stream is pumped together with sheath buffer into the system. The microchannel design consists of a pinched segment which opens into a broadened segment with bifurcations. The width of the pinched segment is the most critical dimension as it has to be comparable to the diameter of the cells and significantly smaller than the broadened segment (Figure 1.5A). By controlling the flow rate ratio between the sample and sheath flow, cells in the sample flow are aligned to one channel sidewall in the pinched segment, with the smaller sized cells being aligned closer to the channel wall than the bigger cells. The flow profile expansion in the broadened segment then amplifies this difference in lateral positions of the center of inertia between cells of varying sizes and directs them into distinct outlets, thus achieving separation. The technique was successfully employed to achieve separation of 15 μm and 30 μm polystyrene particle mixture [74], RBCs filtration [75] and size-based sorting of emulsion droplets [76]. Recently, the group improved the technique by combining PFF with sedimentation force effect (centrifugal force) in a curved broadened segment to separate particles based on size and density [77]. PFF was also used to identify point mutations in HBB gene with functionalized polystyrene microspheres of different sizes [78]. The technique is highly versatile as cells of varying sizes can be separated effectively by tuning the ratio of the sample and sheath buffer flow rates in the same device. High separation efficiencies $\geq$ 90% with throughput of ~ 4000 particles/min have been demonstrated [75]. Drawback however includes low working flow rates as inertial forces acting on the particles tend to affect particle motion at high flow rates, affecting separation efficiency.

1.6.3 Hydrodynamic filtration

Hydrodynamic filtration is another passive separation technique introduced by Yamada *et al.* for size-based cell and particle separation [79]. In this technique, sample is pumped through a main channel having multiple side branching outlets. These side channels continuously drain liquid from the main channel, thereby aligning particles along both sidewalls of the main channel (Figure 1.5B). Similar to PFF, smaller particles are aligned closer to the sidewall than larger particles, thus resulting in their earlier filtration into the side outlets. The technique was used to demonstrate ~ 29 fold enrichment of leukocytes in blood [79]. Recently, the group also demonstrated size-based separation of liver cells with throughputs > 2×10^5 cells/min [80], as well as shape-based separation of budding yeast cells for cell-cycle synchronization [81]. Unlike PFF, the separations are based on flow profile and not channel geometry. Therefore the larger channel design minimizes clogging issues and allows higher throughput than PFF.

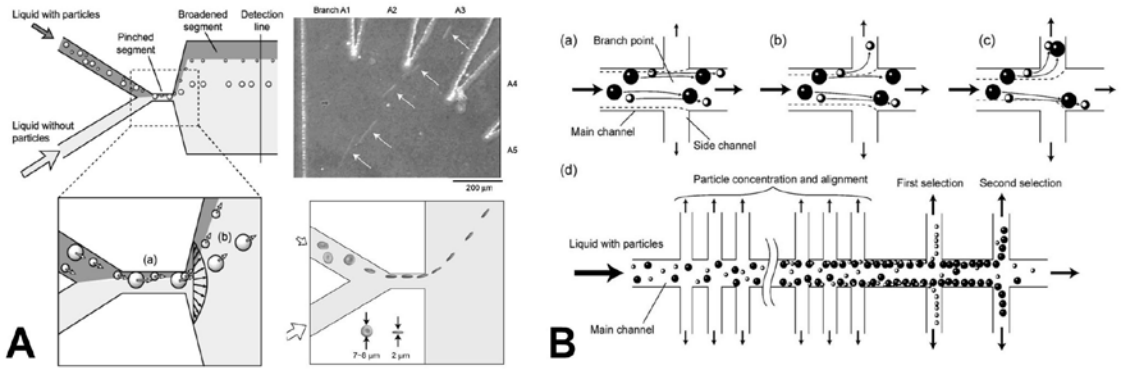

Figure 1.5. (**A**) (*left*) Schematic illustrating the principle of pinched flow fractionation. Suspended particles are aligned against microchannel sidewall in the pinched segment and are separated according to their sizes as they flow into the broadened segment as a result of expansion of the laminar flow sheet [74]. (*right*) Photograph and schematic illustration of RBCs separation (indicated by arrows) employing PFF in a microfluidic device is also shown [75]. (**B**) Principle of hydrodynamic filtration. (a)–(c) Schematic diagrams showing particle positions at a branch point at; (a) low, (b) medium, and (c) high relative flow rates. (d) Schematic diagram showing particle concentration and separation into multiple side channels [79].

1.6.4 Affinity-Based Separation

In affinity-based separation, sorting is effectively achieved by the binding of desired cells to specific molecules immobilized on the microfluidic device. Unwanted cells are permitted to

flow through without interaction and can be completely removed during the washing step. The technique is highly specific, targeting only cells that express the complementary molecules and has the ability to separate cells of similar physical characteristics (size, density). Sensitivity of the technique is greatly enhanced in microfluidic devices as surface area to volume ratio is significantly larger than macroscale adhesion assays. Such technologies have been demonstrated for separating mixed suspensions of T and B lymphocytes with high purity (>97%) (Figure 1.6A) [82]. Purity of captured subpopulations remained high when target cells concentration was low, demonstrating the high sensitivity of the system. Nagrath *et al.* also successfully isolated CTCs from peripheral blood of cancer patients using anti-EpCAM antibodies coated on microposts (Figure 1.6B) [83]. The group later changed the channel design to herringbone structures which generate secondary vortices to continuously mix blood sample and promote binding of CTCs to the coated surfaces [84]. Major limitations for affinity-based sorting include polymorphisms in target proteins, finding a suitable biomarker specific for the targeted cells and the complex surface coating chemistry involved. Furthermore, microdevices coated with proteins/ antibodies have shorter shelf life and binding performance is susceptible to environment factors such as temperature and humidity.

Although affinity-based cell separation is primarily based on presence of specific surface markers, Gleghorn *et al.* have recently developed a microfluidic device which consists of staggered obstacle arrays for both size-dependent and affinity-based capture of prostate CTCs from peripheral blood [85]. The geometrical positions of the pillars are carefully designed such that when cells impact with the pillars, the bigger prostate CTCs are displaced onto streamlines that impinge onto the next pillar while smaller blood cells continue in the original trajectory. This increases the chances of CTCs capture onto the antibody-coated pillars, resulting in a higher efficiency and capture purity.

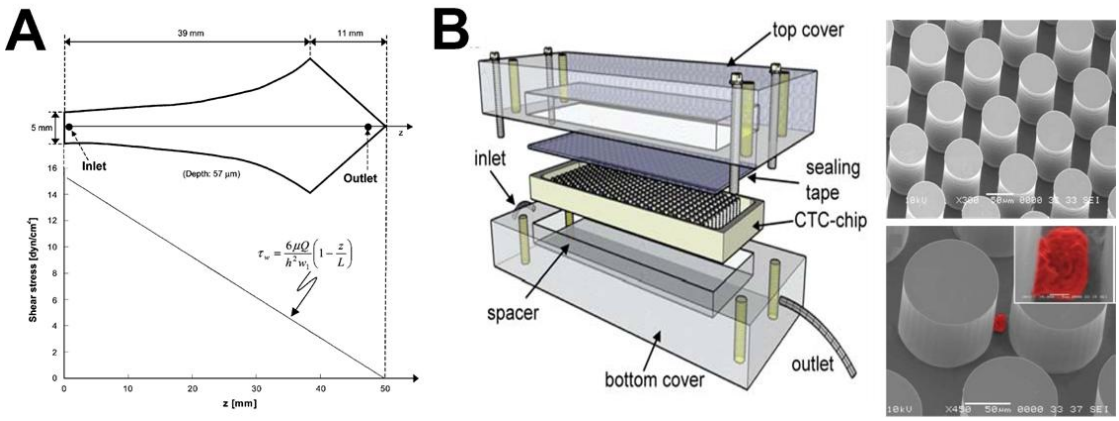

Figure 1.6. Affinity based separation. (**A**) Linear shear stress chamber used by Murthy et al. to determine the effect of shear stress on the binding and separation efficiency of T and B lymphocytes [82]. (**B**) Layout of the CTC chip designed by Nagrath *et al.* consisting of micropost array. Inset showing a SEM image of a lung cancer cell (pseudo coloured red) between two chemically functionalized microposts [83].

1.6.5 Other passive mechanisms

Other passive cell sorting methods include size-based separation based on hydrophoretic sizing [86, 87]. The technique relies on the generation of a pressure field gradient induced using slanted obstacles placed in the flow path. Enrichment of leukocytes from RBCs with a 210-fold enrichment ratio at a throughput of 4×10^3 s^{-1} was demonstrated. Another mechanism is using the inherent motility of cells (either by diffusion or active motility) as a biomarker for cell separation. For example, Cho *et al.* [88] used a microfluidic laminar flow junction of two streams to separate motile, healthy sperm from unhealthy ones.

Two other important passive cell sorting techniques; 1) inertial focusing [89] and 2) biomimetic flow phenomena [90] have also been demonstrated by us and others for efficient cell separation. As the microfluidic approaches presented in this thesis involve similar working principles, these techniques will be discussed in greater details in the subsequent chapters. Table 3 presents a summary of the different passive techniques in terms of their separation principle and characteristics.

Table 3. Comparisons between various passive separation methods.

	Method	Mechanism/Principle	Separation markers	Flow rate/ throughput
PASSIVE	Pillar and weir Structures	Laminar flow	size deformability	1,000 μm s^{-1} [68] 5 μL min^{-1} [71]
	Pinched flow fractionation (PFF)	Laminar flow (Hydrodynamic force)	size	~4000 min^{-1} [75] 20 μL hr^{-1} [75]
	Hydrodynamic Filtration	Hydrodynamic force	size	20 μL min^{-1} [79] >100,000 min^{-1} [80]
	Inertial	Shear-induced and wall-induced lift	size shape	~10^6 min^{-1} [89]
	Surface affinity	Specific binding to surface markers	surface biomarkers and size	1-2 mL hr^{-1} [83]
	Biomimetic	Hydrodynamic force / Fahraeus effect	Size deformability	10 μL hr^{-1} [90]
	Hydrophoretic filtration	Pressure field gradient	Size	4×10^3 s^{-1} [87]

1.7 Motivation

Of the ~5 billion cells per milliliter of blood, RBCs accounts for >99% of all cellular components. Besides blood constituents, pathogenic microorganisms or diseased cells such as *i*RBCs and CTCs are also present in peripheral blood in different diseases, which are of clinical significance and important for fundamental research. However, due to the vast majority of RBCs, separation and isolation of diseased cells from blood has been a challenging problem both from a medical and engineering perspective. Common macroscale separation techniques such as physical filtration, FACS and MACS have limited success, mainly due to laborious sample preparations which introduce artifacts or lead to loss of desired cells. Hence, it is necessary to develop new methodologies for efficient blood processing and isolation of these rare diseased cells.

As mentioned earlier, microfluidics is ideal for cell separation leveraging its numerous inherent advantages. Despite the recent emergence of microfluidic technologies, the development of microfluidic separation techniques to date is mostly suitable for dilute particle or cell samples. Moreover, current microfluidic approaches developed for blood fractionation

suffer from problems such as laborious sample preparation, low throughput and clogging issues after long period of processing time. Therefore, developing efficient and cost-effective microfluidic blood separation platforms will be imperative in realizing point-of-care (POC) devices and invaluable for many downstream clinical and biological applications.

1.8 Scope of work

In this work, several microfluidic approaches for diseased cells separation from blood using physical biomarkers (size and deformability) will be investigated. The mode of operation in the proposed devices will be passive as the separation principles rely entirely on the channel geometry and inherent hydrodynamic forces. This dissertation is focused on the microfluidic cell separation of several blood-related diseases including sepsis, malaria and cancer (presence of CTCs in blood) using different passive separation principles.

For sepsis, a novel biomimetic separation technique based on microcirculatory phenomenon such as leukocyte margination and Fåhræus effect was employed for high-throughput bacteria removal from blood as a potential blood cleansing method for sepsis treatment. A two-stage cascaded system was implemented to achieve higher bacterial removal efficiency and the design simplicity enabled easy multiplexing (6 channels in parallel) to achieve higher throughput with similar filtration performance. By using different channel geometry, the margination technique was also applied for deformability-based separation of *i*RBCs from whole blood for rapid *i*RBCs enrichment. No sample preparations are required and the device simplicity potentially enables testing in resource-poor settings, where malaria infection is most prevalent.

For cancer application, inertial microfluidics using straight and spiral channel geometry were used for continuous size-based separation of CTCs from peripheral blood. The first design consists of a high aspect ratio microchannel patterned with an array of expansion and

contraction regions and a “pinching” region at the channel end. By employing high aspect ratio channels, the shear rate across the microchannel cross-section can be modulated, resulting in preferential cell equilibrium at the sides along the channel height. Larger CTCs were selectively “pinched” to the channel centre upon exit, resulting in a continuous CTCs separation to the centre outlet while smaller RBCs and leukocytes were removed from the side outlets. For the spiral device, a new separation technique termed as *Dean Flow Fractionation (DFF)* was introduced. In this method, the additional Dean vortices due to spiral geometry resulted in the Dean migration of smaller blood components to the channel outer wall as larger CTCs focused at the inner wall due to inertial focusing. The large channel dimensions enable processing of high hematocrit blood samples (~20%) and the developed *DFF* technique is one of the fastest microfluidic CTCs separation method to date, at an ultra-high throughput of 20 mins/ mL of whole blood.

1.9 Chapter summaries

The work in this dissertation has been presented in a number of international and domestic conferences in the fields of microfluidic technologies. The majority of the chapters have also been published in appropriate peer-reviewed journals. Following this introduction, **Chapter 2** reports on the separation of microbes (bacteria and yeast) from blood using the margination technique. We first present the design principle of the cascaded channel design using electrical circuit analysis. Next, effect of different parameters (flow rates, channel dimensions) on bacteria margination and experimental results of whole blood spiked with different microorganisms will be shown. At the end of the chapter, device multiplexing by channel parallelisation and stacking method is demonstrated to improve the blood filtration throughput.

Chapter 3 reports on the deformability-based margination of *i*RBCs from whole blood. Following the introduction on physical characteristics of *i*RBCs and current malaria detection methodologies, experimental results using 3 μm beads and testing of different stages of

*i*RBCs are presented. Channel variations in the new design to improve *i*RBCs enrichment ratio will also be shown. Lastly, the hemodynamic significance of *i*RBCs margination in microcirculation *in vivo* will be demonstrated with another microfluidic device consisting of a capillary-like channel network. The work in this chapter has been the basis for the article published in *Lab on a Chip* [91].

Chapter 4 begins by introducing the importance of CTCs as a useful biomarker in clinical management, challenges associated with convectional CTCs separation methods, and principles of inertial focusing in straight microchannels. This is followed by discussion on the developed channel design and schematic working principle. For device characterization, we first studied the effect of channel aspect ratio, flow rate and hematocrit on RBCs focusing to determine the maximum throughput with our device. Next, testing of different cancer cell lines and the implementation of two cascaded devices with enhanced separation performance will also be presented. This work has been published in *Lab on a Chip* [92].

Chapter 5 will discuss on the principles of Dean Flow and its applications for particle separation, followed by the introduction of *Dean Flow Fractionation (DFF).* To validate the separation principle, computational simulation using COMSOL and experimental results using beads and cell samples to understand the effect of Dean migration and inertial focusing of cancer cells will be presented. Finally, the successful implementation of two spiral devices in tandem and the easy coupling of the developed cascaded system with 96-well plate for different downstream analysis will be demonstrated as a potential platform for high-throughput CTCs isolation.

Lastly, **Chapter 6** will provide a summary of this work.

2 Microbial removal using margination for sepsis treatment

In this chapter, we report a simple microfluidic approach for intrinsic, non-specific removal of both microbes and inflammatory cellular components (platelets and leukocytes) from whole blood, inspired by the *in vivo* phenomenon of leukocyte margination. The developed technique can potentially be used for sepsis treatment and offers significant advantages including high throughput (~1mL/hr per channel) and label-free separation which allows non-specific removal (> 80%) of any blood-borne pathogens (bacteria and fungi). The simplicity of the device architecture also allows easy multiplexing to achieve higher throughput and we successfully designed and tested a larger filtration device consisting of 6 channels in parallel (~6mL/hr) with similar filtration performance.

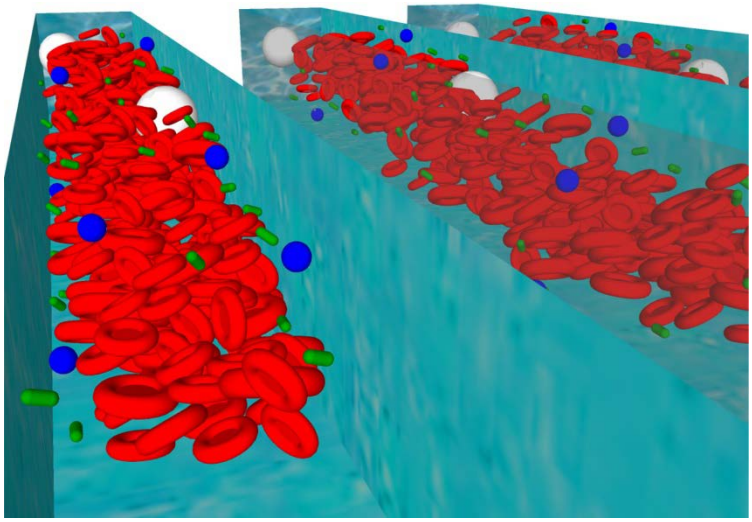

2.1 Background

2.1.1 Sepsis

Sepsis is a critical medical condition characterized by a systemic inflammatory response syndrome (SIRS) due to microbial infection and represents a substantial health care and economic burden with increasing incidences over the years [93]. Upon infection, the innate immune system responds by initiating inflammatory pathways and leukocyte recruitment to the site of infection to combat the infectious agents. However, excess production of cytokines and inflammatory mediators can trigger a systemic inflammation, resulting in widespread activation of vascular endothelium, amplification of coagulation cascades through platelet activation and increase of circulating peripheral leukocytes (mainly neutrophils and macrophages) (Figure 2.1) [16]. These multi-factorial effects damage microvasculature and induce tissue hypoxia, leading to septic shocks or deaths in severe cases as a result of multiple organ dysfunctions [16, 94].

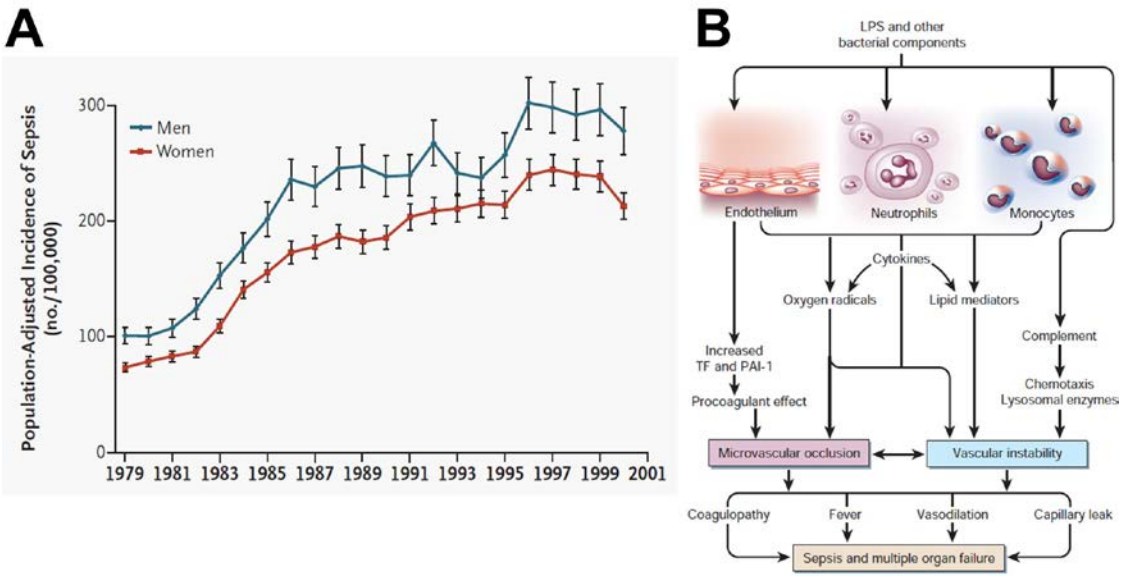

Figure 2.1. (**A**) Incidence of sepsis cases in United States from 1979 to 2011, according to gender [93]. (**B**) Pathophysiological effect in sepsis shock. Simultaneous activation of different components of the immune system leads to impaired microvasculature and organ failure due to hypoperfusion [16].

Current sepsis treatments include antibiotics therapy and patients in critical conditions also receive intravenous fluids to maintain blood pressure and prevent vital organs from failing. However, drug treatment is limited by dose toxicity and rapid emergence of drug-resistant pathogens [95-97]. Infants with sepsis (neonatal sepsis) are especially at risk because their immune system are functionally immature and delay or inappropriate antibiotic treatment may cause fatality [98]. Extracorporeal blood purification therapies have also been used for sepsis treatment and have shown to stabilize hemodynamics and improve clinical outcomes of patients [99-101]. Similar to conventional dialysis system, semi-permeable membrane (diffusion/convection) or sorbent (adsorption) are used to non-selectively remove water-soluble inflammatory mediators and endotoxin from the plasma. However, drawbacks of these techniques include loss of beneficial molecules (nutrients and drugs) during dialysis and treatment is expensive due to large volume of replacement fluid post-filtration and high nursing workload [102-104]. Currently, there is no general consensus on which components of the blood should be removed for better clinical outcome. In this regard, what is necessary is a hemofiltration technique that removes a broad array of targets (pathogens, immune cells, platelets, etc.) from blood, in order to help modulate (but not eliminate entirely) the overall inflammatory response.

2.1.2 Microfluidics approaches for microbial separation from blood

As discussed in the introduction chapter, microfluidic technologies are useful for blood separation due to numerous advantages such as reduced contamination issues, portability and process automation [41, 43, 105]. Typically, pathogenic microorganisms are very small, ranging from 1-3 μm in diameter and can be easily separated from the larger RBCs and leukocytes. Several microfluidic approaches for microorganism separation from blood have been previously demonstrated based on either size differences [106, 107] or affinity separation [108, 109]. However, laborious sample preparations involving blood dilution and magnetic labeling of microorganisms significantly limit their throughput. Large volume of

buffer fluid is required for blood dilution or sheath flow in these methods, making them inconvenient to process large quantities of blood over prolonged period of time. Moreover, the removal of microorganisms itself may not be sufficient to attenuate the overwhelming host immune response as an application for sepsis treatment. In this work, we attempt to overcome some of these challenges by introducing a novel microfluidic approach for intrinsic, non-specific removal of microorganisms and inflammatory cellular components from whole blood directly, inspired by the *in vivo* phenomenon of leukocyte margination [10, 13].

2.1.3 Microcirculatory hemodynamics

In blood vessels with luminal diameter less than 300 μm, RBCs which are smaller in size and more deformable than the leukocytes, tend to migrate to the axial centre of the vessel, resulting in a formation of a reduced hematocrit plasma layer adjacent to the vessel wall and an increased RBC concentration at the centre of the vessel (Fahraeus effect) [10]. This inward RBC migration is attributed to Poiseuille flow profile within the vessel which results in a pressure gradient induced force directed towards the centre. As RBCs migrate towards the axial centre, mechanical collisions between the leukocytes and migrating RBCs results in the larger (and stiffer) leukocytes being displaced to the vessel wall; a phenomenon aptly termed as margination [110, 111]. These two hemodynamic effects, the Fahraeus effect and margination, have been successfully employed in microfluidic devices for plasma separation [112, 113] and leukocyte enrichment from whole blood [114, 115] (Figure 2.2). Besides leukocytes, platelet margination has also been observed in concentrated blood flow as excess platelets are found at the RBCs-depleted region next to the channel walls [116, 117]. Although axial migration of RBCs to channel centre can partly lead to physical exclusion of platelets towards the wall, actual mechanisms responsible for platelet margination are known to be more complex and strongly dependent on hematocrit and shear rate [118, 119]. For example, Zhao *et al.* highlighted the importance of RBCs influence by showing that platelet margination increases with hematocrit, most notably at hematocrit greater than 30% [119].

Turitto and Weiss also proposed that collisions between RBCs and platelets can contribute to margination process due to enhanced platelet diffusion towards the vessel wall [120]. Using computational fluid dynamics (CFD) modeling of platelet-RBCs interactions, Almonani *et al.* found that RBCs motions (tumbling and translation) and cell-cell interactions cause localized flow fluctuation, leading to an increase in fluid shear forces acting on the platelets which promote their margination towards the channel walls [121]. They further showed that platelet margination is predominantly caused by the large size difference (not shape) between RBCs and platelets.

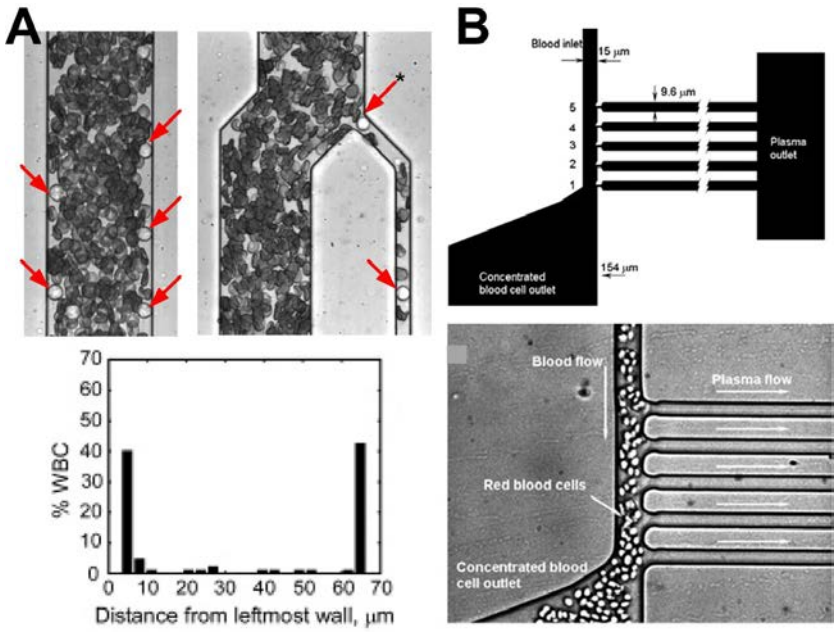

Figure 2.2. Fahraeus effect based cell separation. (**A**) A 34-fold leukocytes enrichment was achieved by employing a 5.5 mm long rectangular microchannel based on leukocyte margination (leukocytes indicated by arrows). The larger leukocytes are displaced to the channel sidewalls and extracted using an asymmetrically bifurcated outlet [114]. (**B**) Microfluidic device with a series of parallel side channels used for plasma skimming from whole blood. The figure also shows a high-speed snapshot confirming the concentration of RBCs at the microchannel center with pure plasma collected at the plasma outlet [90].

2.1.4 Motivation

There are different kinds of pathogenic microorganisms (bacteria, fungus, viruses and protozoa) of which bacteria is the predominant causative organism in septic patients [93] and *Candida albicans* is the most life-threatening fungal pathogen in human sepsis cases. Bacteria

morphology varies widely and can be classified as either spherical (cocci) or rod-shaped (bacilli). For example, *Escherichia coli* (*E. coli*) are Gram-negative, rod-shaped bacterium typically about 2.0 μm long and 0.5 μm in diameter. As bacteria (~1-3 μm) are similar in size as platelets, we hypothesize that microbes in blood flow can also undergo margination towards the wall region by similar mechanisms which can be used for bacteria separation applications. In addition, the bacterial cell wall consists of a rigid layer of peptidoglycan network (Young's Modulus ~10^7 Pa) to help maintain the cell shape by resisting the turgor pressure [122, 123] and is much stiffer as compared to RBCs (membrane Young's Modulus ~10^4 Pa) [124]. Similarly, fungus (typically ovoid shape, ~5-7 μm in diameter) cell wall consists of β1,3-glucan and chitin which provide both mechanical strength and elasticity to the cell wall [125] and the cell wall elastic modulus (~10^8 Pa) is also higher than RBCs membrane [126]. Hence in this work, we investigate using microfluidics if these distinct differences in size and deformability between microorganisms and RBCs could play a role in margination and be applied as a high-throughput blood filtration technique for removal of pathogens from blood.

2.2 Design principle

2.2.1 Separation principle

The microchannel design consists of two cascaded straight microchannels, 20×20 μm (w×h), with two bifurcations in series (1:8:1). As blood flows through the straight channel (margination region), deformable RBCs migrate to the axial centre of the channel to form a RBC-rich core and a cell-free layer adjacent to the channel walls (Figure 2.3). Mechanical collisions between the migrating RBCs and other cell types (bacteria, platelets and leukocytes) result in their margination towards the channel walls into the cell-free layer. The outlet of each margination channel expands into a 200 μm wide section to enhance the cell-free layer allowing majority of the RBCs to enter the centre outlet while the other cell types flowing at the sides are removed through the smaller side channels into the waste [127]. By cascading

two margination channels in series, the bacteria-depleted blood at the first bifurcation undergo another round of margination, thus achieving a two-stage separation and higher bacterial removal efficiency in a single pass through the device.

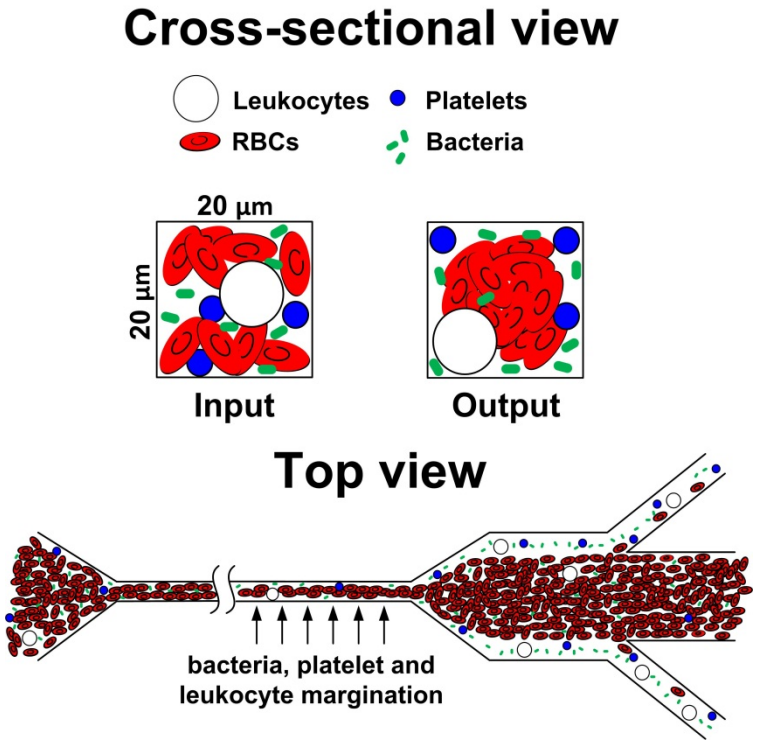

Figure 2.3. Cross-sectional and top view of the microchannel illustrating the separation principle. As blood flows through the channel (margination region), deformable RBCs migrate axially to the channel centre, resulting in margination of other cell types (bacteria, platelets and leukocytes) towards the channel walls and subsequently removed from the side outlets while the centre outlet collects the bacteria-depleted blood.

2.2.2 Microfluidic design using circuit analysis

To design the cascaded fluidic circuit, it is essential to determine channel geometries that can meet the specific flow ratio in different channels. In a manner analogous to an electrical current, fluidic flow rate (Q) in a channel is proportional to the applied pressure drop (ΔP) and can be described as

$$\Delta P = R_h Q \qquad (1)$$

where R_h is the hydrodynamic resistance. This expression is similar to Ohm's law relating voltage difference (ΔV) and current (I) to the resistance of conductor (R), ΔV = RI. Furthermore, the generalization of Kirchhoff's laws for electric circuits can also be applied for

designing microfluidic circuit network. Using Stokes equation, it has been shown that in a rectangular channel with width (w) and height (h), the hydrodynamic resistance can be approximated as [128, 129]

$$R_h \approx \frac{12\mu L}{(1-\frac{0.630h}{w})wh^3} \quad (2)$$

where μ is fluid viscosity, L is channel length and $h < w$. Since channel height and fluid properties are constant, the equation can be simplified to the following relationship,

$$R_h \propto L \propto \frac{1}{w} \quad (3)$$

Based on the relationship in equation (3), the channel hydrodynamic resistance can be easily controlled by varying the channel dimensions. Using this relationship and verification with B2 Spice simulation (Beige Bag Software, MI, USA), we designed a cascaded straight channel design which allows a two-stage removal of microbes in a single processing step, and the volume flow ratio of the filtered blood into the centre outlet was fixed at 0.8 (80%) at each bifurcation (Figure 2.4).

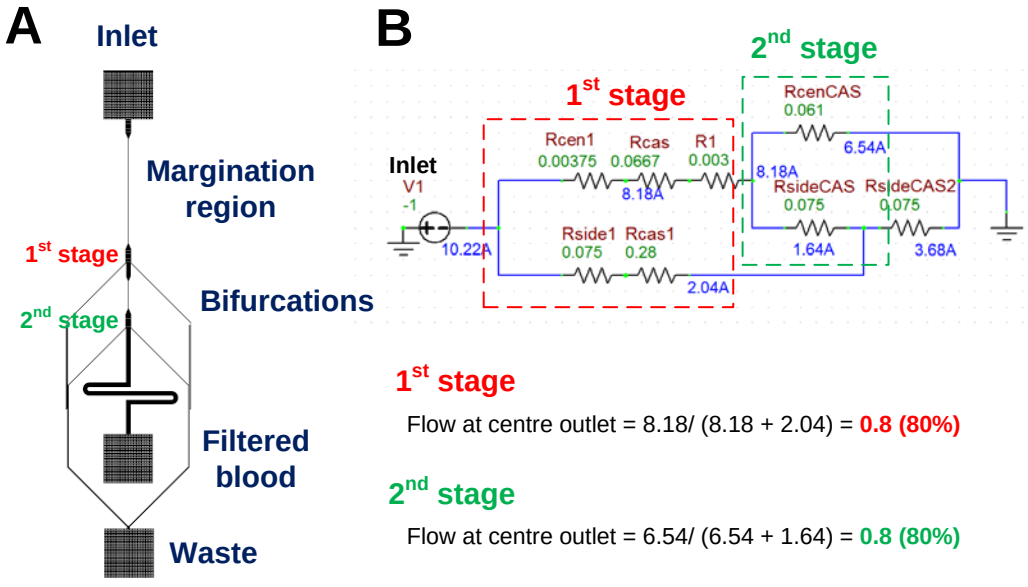

Figure 2.4. Schematic illustration of the channel design and electrical circuit analysis. (**A**) The design consists of two cascaded straight microchannels (5 mm long, 20×20 µm (W×H) for the first channel and 1mm long, 20×20 µm (w×h) for the cascaded channel) with two bifurcations (1:8:1) in series. (**B**) Diagram of a resistive circuit corresponding to the microchannel design in (**A**). Different bifurcation stages are highlighted in the circuit and the

channel hydrodynamic resistances are designed such that the flow distribution into the centre outlet is 0.8 (80%) at each stage.

2.3 Experimental procedures

Fabrication

Channel layouts were designed using L-Edit (Tanner EDA, USA) and devices were fabricated in polydimethylsiloxane polymer (PDMS, Sylgard 184, Dow Corning, USA) using standard microfabrication soft-lithographic techniques (Figure 2.5) [130]. The channel designs were first patterned on polished silicon wafers and etched into silicon using deep reactive ion etching (DRIE). Following etching, the patterned silicon wafers were silanized with trichloro(1H,1H,2H,2H-perfluorooctyl)silane (Sigma Aldrich, USA) for 1 hr to facilitate PDMS mold release. PDMS prepolymer mixed in 10:1 (w/w) ratio with curing agent was poured onto the silicon wafer and cured at 70 °C for 2 hr. The cured PDMS mold then acted as a template for subsequent PDMS casting (negative replica). The PDMS master template was silanized for 1 hr before use to aid release of subsequent PDMS microchannels. Finally, holes (1.5mm) for inlets and outlets were punched and the PDMS microchannels were irreversibly bonded to microscopic glass slides using an air plasma machine (Harrick Plasma Cleaner, USA) and left for 2 hr at 70 °C to complete the bonding.

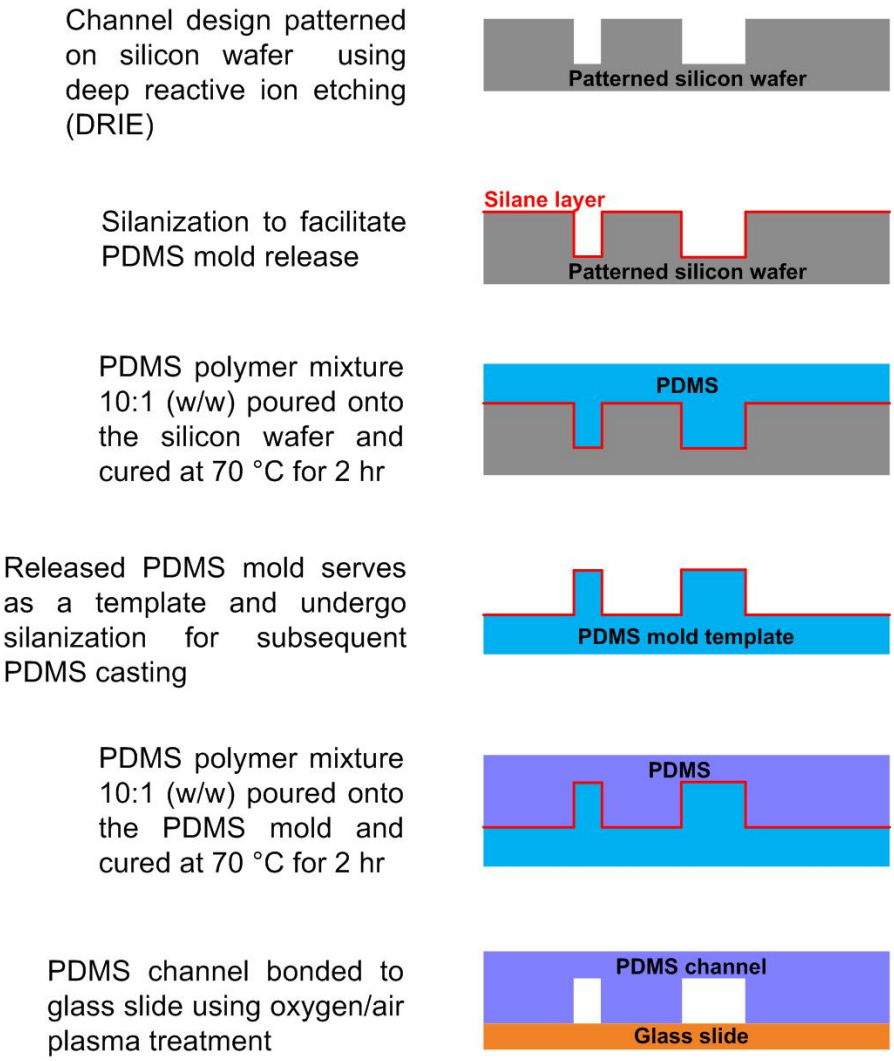

Figure 2.5. Schematic of the rapid PDMS double-casting process to fabricate PDMS microchannels using silicon wafer patterend by Deep Ion Reactive Etching (DRIE).

Cell culture

E. coli (HB101 K-12) bacteria expressing green fluorescent protein (GFP) were cultured overnight at 37°C in LB Agar (Sigma Aldrich, USA) containing ampicillin (100 μg/mL) and arabinose (0.1%, inductor of GFP expression), then harvested and resuspended in 1× phosphate buffer solution (PBS) for experimental use. Haploid S. cerevisiae (W303-1B strain) expressing yellow fluorescent protein (YFP) was a kind gift from Dr. Jacquin Niles from the Department of Biological engineering at MIT.

Sample preparation

For device characterization, human whole blood (Research Blood Components, Brighton, MA) was washed three times with washing buffer containing 1× PBS, 0.5% v/v bovine serum albumin (BSA) (Miltenyi Biotec, USA) prior to running the experiment. Final RBC concentration was adjusted to physiological hematocrit (~45%) in the sample buffer containing 1× PBS, 0.5% v/v BSA and 3% w/v Dextran 40 (Sigma Aldrich, USA) to prevent cell sedimentation. Alexa Fluor® 488 *E. coli* (K-12 strain) BioParticles® conjugates (Invitrogen, USA), cultured bacteria and yeast were added to blood samples ($10^{6\text{-}7}$/mL) and vortexed for 30 seconds before use. For whole blood analysis, fresh human blood was incubated at 4 °C for 40 minutes with fluorescein isothiocyanate (FITC) conjugated CD41a antibodies (1:50, BD Biosciences, USA) and allophycocyanin (APC) conjugated CD45 marker (1:100, BD Biosciences, USA) to identify platelets and leukocytes, respectively.

Device characterization and analysis

Whole blood samples were pumped through the microfluidic devices using a syringe pump (NE-1000, New Era Pump Systems Inc., USA). The microchannels were mounted on an inverted phase contrast microscope (Olympus IX71) equipped with a Hamamatsu Model C4742-80-12AG CCD camera (Hamamatsu Photonics, Japan). IPLab (Scanalytics, Rockville, MD) software was used for video acquisition and captured videos were analyzed using ImageJ® software. For *E. coli* BioParticles® and whole blood analysis, separation efficiency was determined by performing flow cytometry analysis on the sample and collected centre outlet using BD™ LSR II flow cytometer (BD Biosciences, USA). Different cell types were gated based on the forward and side scatters as well as the specific fluorescence intensity. For microbial experiments, bacteria concentrations at the inlet and filtered centre outlet were determined by plating 10 µL of solution on LB Agar and colony-forming units (CFUs) were counted after 24 hrs of incubation at 37 °C. Bacteria and yeast concentrations were also diluted and evaluated using a hemocytometer separately.

Confocal imaging

A LSM 510 meta laser scanning confocal (Carl Zeiss, Jena, Germany) was mounted on an Axiovert 100M Inverted Microscope (Carl Zeiss, MicroImaging) and images were acquired at 488 nm excitation. A 10X objective of the microscope was used with an additional digital zooming of 2.5X (from software) to prevent unnecessary photobleaching of adjacent areas. Image slices were acquired at an interval of 1μm in z-axis (vertical axis) with a resolution of at least 512 x 512 pixels at a minimum scanning speed of 0.96 μs per pixel. Captured images were then analyzed using ImageJ® software.

2.4 Results and discussion

2.4.1 Aspect ratio study

The microchannel design and testing conditions were first optimized by studying the effect of various parameters including microchannel aspect ratio, channel length and flow rate on bacteria margination. To study the effect of channel height/aspect ratio on bacteria margination, a single margination channel of 15 mm length, 20 μm width with varying heights of 10 μm, 20 μm, 45 μm, 75μm were fabricated, yielding aspect ratios (height/width) of 0.5, 1, 2.25 and 3.75 respectively. The channel width was fixed at 20 μm due to enhanced Fahreaus effect in smaller channels as axial migration of RBCs becomes less efficient with increasing channel size [10, 115]. Whole blood spiked with FITC-conjugated *E. coli* bioparticles was pumped into each device and the filtered blood at centre outlet was collected for FACS analysis. Bacteria concentration at the centre outlet was then normalized with the sample to determine the separation efficiency. Figure 2.6A presents the normalized bacteria concentration in the filtered centre outlet at different channel heights. At low channel heights of 10 and 20 μm (aspect ratio $\leqslant$ 1), ~40% of bacteria remained in the centre outlet after filtration, indicating efficient bacteria margination in our device. As channel height increased to 45 and 75 μm (aspect ratio $\geqslant$ 1), bacteria margination became less efficient with >60% of

bacteria still remaining at the centre outlet. This is consistent with previous studies which reported that margination of leukocytes and malaria-infected RBCs were more prominent in low aspect ratio channels [91, 114, 131]. To further understand bacteria margination in different aspect ratio channels, confocal microscopy was used to image the bacteria distribution at the outlet of 20 µm (aspect ratio 1) and 75 µm (aspect ratio 3.75) height channel which clearly illustrates a distinct difference in bacteria margination efficiency between these channels. As compared to the channel inlet, there was a ~3× decrease in fluorescence signal at the mid plane of the channel outlet for 20 µm height channel, indicating lesser bacteria remaining at the centre region due to their efficient margination to the sides (data not shown). Confocal images were also acquired along the channel height which showed that the vertical intensity profile of the outlet centre region for 20 µm height channel was almost uniform, indicative of efficient bacteria margination across the depth (Figure 2.6B). Although bacteria undergo margination to the four channel walls, fluorescence intensity peaks were absent at the top and bottom channel wall proximities because of the sudden width expansion from 20 µm to 200 µm at the bifurcation which caused the bacteria to disperse across the channel width. However, for 75 µm height channel, there was uneven bacteria margination along the height, with a strong fluorescent intensity peak observed at the mid plane region. Confocal images of the channel outlet at the mid plane also showed negligible bacteria margination for 75 µm height channel as bacteria remained evenly distributed throughout the channel and fluorescence intensity was similar as compared to the channel inlet (data not shown).

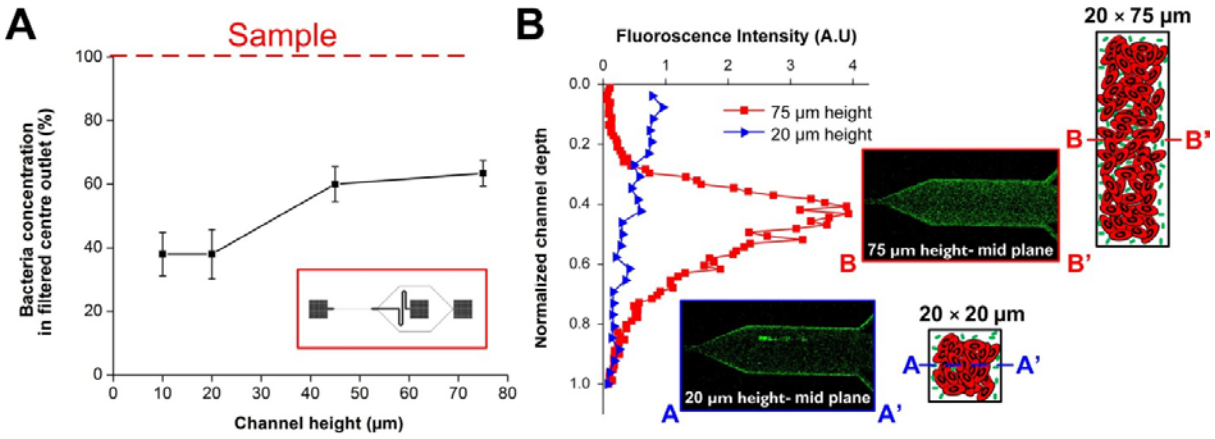

Figure 2.6. Effect of microchannel height (aspect ratio) on bacteria margination. (**A**) Bacteria concentration in the filtered centre outlet with varying channel heights using a single margination channel of 15 mm length and 20 μm width (schematic single channel design in red box). Bacteria concentration was normalized with sample to determine the percentage of bacteria remaining after filtration. (**B**) Fluorescent intensity Z-profiles at the outlet centre region of 20 μm and 75 μm height channels and corresponding schematic illustration of their bacteria margination. Confocal images at the mid plane of 20 μm and 75 μm height channels indicate less efficient bacteria margination at the mid plane region of high aspect ratio channel.

Several reasons can be accounted for the observed differences in margination efficiency. Firstly, low aspect ratio channels (aspect ratio $\leqslant$ 1) closely resemble circular blood vessels in which the fluidic shear distribution is isotropic and uniform across the channel cross-section. As RBCs axial migration distances are the same in all directions, a well-defined RBC core can be easily formed at the centre region in circular and low aspect ratio channels, thereby allowing effective bacteria margination to the sidewalls. For high aspect ratio (ratio $\geqslant$ 1) channels, although there is a higher shear rate along the shorter channel width, shear rate is much lower along the height (z-direction) and more RBCs are packed at the centre region due to Fahreaus effect. This gives rise to a blunt velocity profile in the z-direction which can significantly influence the axial migration behaviour of RBCs at the mid plane region [115, 132]. Moreover, bacteria margination at the mid plane region may be less effective as bacteria can be displaced vertically along the height in addition to axial margination towards to lateral walls, resulting in bacteria being trapped at the channel centre. Similar observations were also made by Jain and Munn who showed that margination of leukocytes to the sidewalls

decreased with channel height due to their lateral displacements towards top and bottom surfaces [131]. Hence, high aspect ratio microchannels are unfavourable for separation applications and we limit the channel height to be 20 µm as channel aspect ratio of 1 gave the most effective bacteria margination with the highest throughput.

2.4.2 Channel length study

After optimizing the channel height, the effect of channel length on bacteria margination was studied to determine the shortest channel length required for efficient bacteria margination. Experimental results indicate that bacteria margination remained approximately constant for channel lengths between 5 mm to 20 mm but less efficient at 2 mm. This is most likely due to insufficient RBC transit time and axial migration in the margination channel which prevented the formation of the RBC core. Therefore the channel length was fixed at 5 mm as this would minimize the pressure drop across the device and allow testing at higher working flow rate.

2.4.3 Flow rate study

Lastly, experiments were done to characterize the effect of flow rate on bacteria margination. Figure 2.7A presents the normalized bacteria concentration at the filtered centre outlet for increasing flow rates. At low flow rate of 1 $\mu Lmin^{-1}$, bacteria concentration at the centre outlet was comparable to the initial sample, indicating negligible bacteria margination. As flow rate increases, bacteria separation efficiency improved evident by the lower bacteria concentrations at the collected outlet, but remained approximately constant beyond 10 $\mu Lmin^{-1}$. These results were expected because at such high flow rates (Reynold's number ~4-5), RBCs experience higher shear and inertia in the margination channel which expedite their axial migration to the channel centre to form a well-defined RBC core, resulting in margination of small bacteria towards the channel walls. A flow rate of 15 $\mu Lmin^{-1}$ was chosen for subsequent experiments as the PDMS device and connection setup used was not

rigid enough to withstand the pressure drop at higher flow rates for long period of device operation. In addition, it was also observed that the cell free layer was enhanced at the expanded bifurcation with most of the marginated bacteria residing in the cell free region (Figure 2.7B). This is useful for filtration purposes as the large centre outlet of the bifurcation (1:8:1) was able to collect most of the RBCs while the marginated bacteria were efficiently removed via the side channels.

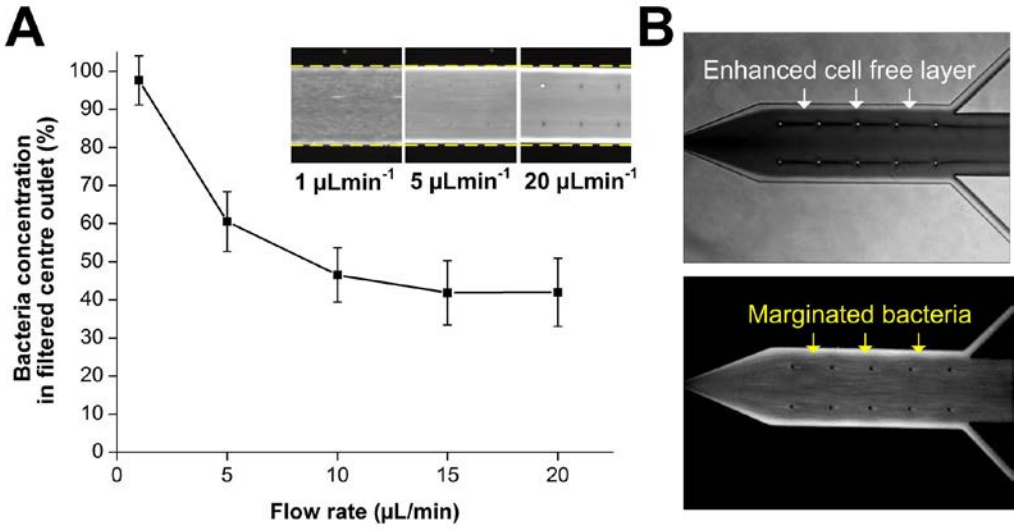

Figure 2.7. Effect of flow rate on bacteria margination. (**A**) Normalized bacteria concentration in the filtered centre outlet for increasing flow rate. Bacteria separation efficiency improved as flow rate increases but remained approximately constant beyond 10 $\mu Lmin^{-1}$. Averaged composite images of the bifurcation indicate increase in concentration of FITC-conjugated bacteria at the channel sides with increasing flow rates. (**B**) Optical images illustrating the enhanced cell free layer at the expanded bifurcation. Most of the marginated bacteria reside within the cell free layer next to the channel wall which allows their efficient removal from the side channels while the densely-packed RBCs are filtered into the larger centre outlet with minimal loss.

2.4.4 Device characterization of the cascaded design

Figure 2.8A presents the averaged fluorescence composite images at the margination channel and their corresponding intensity linescans across the channel width. At the inlet of the channel, FITC-conjugated bacteria were evenly distributed and the fluorescence intensity profile was uniform across the channel although stronger intensities were observed at the channel sides due to slower flow at the corners. At the outlet of the margination channel,

fluorescence intensity at the channel centre decreased with stronger fluorescence intensity peaks at the sides, evident of the higher number of bacteria present near the channel walls after margination. Margination efficiency was determined based on the assumptions that 1) complete bacteria margination to the four channel walls occurred and 2) they would occupy the entire cross section perimeter uniformly. The theoretical separation efficiency was calculated by taking the ratio of the wetted perimeter of the centre region (blue region in schematic) to the total cross section perimeter. As shown in Figure 2.8B, the separation efficiencies obtained from the experimental results at each stage were in good agreement with the theoretical values. By removing a fraction of the plasma and marginated bacteria at the first stage bifurcation, the filtered blood (with higher hematocrit and less bacteria) undergo additional RBCs axial migration (Fahreaus effect) and redistribution in the straight channel region before the 2nd bifurcation, leading to subsequent margination of bacteria towards the channel periphery again. This allows the cascaded design to remove the marginated bacteria via the smaller side channels at each bifurcation successively, thereby achieving a high bacteria separation efficiency of >80%.

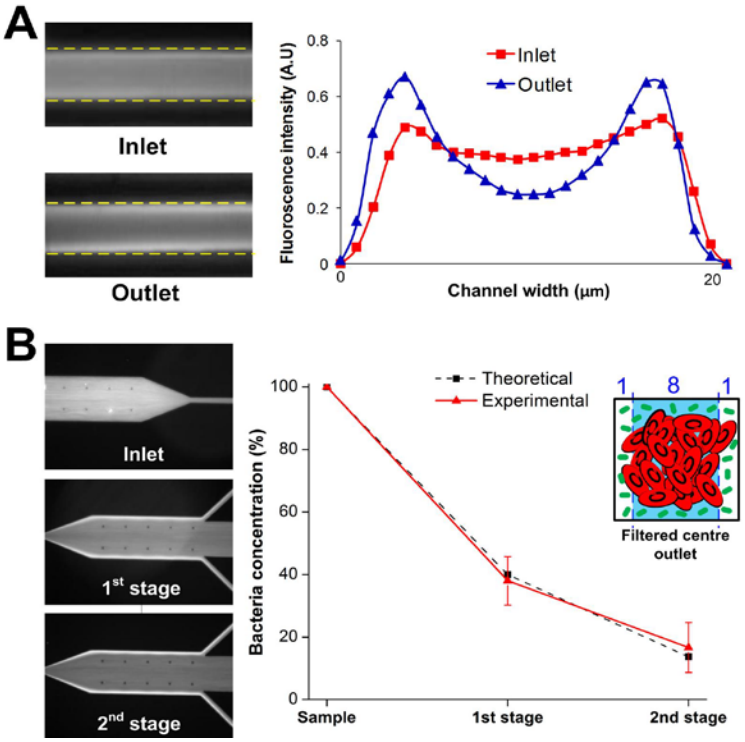

Figure 2.8. Device characterization of the cascaded design. (**A**) Averaged fluorescence composite images at the margination channel (20 μm × 20 μm) and corresponding intensity linescans illustrating the larger number of FITC-conjugated bacteria found at the channel sides after margination. Dotted lines indicate the approximate position of channel walls. (**B**) Plot of bacteria filtration efficiency at different stages. Experimental results were similar to the theoretical separation efficiencies calculated based on the bifurcation ratio (blue region in schematic) and the complete bacteria margination to the four channel walls. A high bacteria separation efficiency of >80% was achieved at the collected centre outlet after two stages of filtration.

2.4.5 Whole blood analysis

Following the characterization of device dimensions and operating conditions, experiments using human whole blood were carried out to quantify the separation efficiency of other cellular components such as platelets and leukocytes. The cells were stained with specific fluorophore-conjugated monoclonal antibodies and identified using FACS analysis. As shown in Figure 2.9A, >80% of leukocytes and platelets were removed in the collected centre outlet, consistent with previous work which reported on the phenomenon of platelets [119, 133] and leukocytes margination [111, 114] in microchannels. RBCs concentration at the centre outlet increased by ~30% as the expanded channel bifurcation at the end of the margination channel allowed efficient filtration of the densely-packed RBCs into the larger centre outlet. Negligible hemolysis was also observed in the filtered blood based on optical absorption at 414 nm due to the short RBCs transit time (<0.01 sec) in the margination channel where the shear rate is the highest. As an application for sepsis treatment, we tested blood sample spiked with two different kinds of microbes, GFP-transfected *E. coli* bacteria and YFP-transfected *S. cerevisiae* yeast, at high microbial concentrations (~$10^{6\text{-}7}$/mL) typically found in sepsis patients. Yeast was used in our experiments to mimic fungal pathogens due to their similarities in morphologies. As expected, results indicate successful removal of ~80% of bacteria and ~90% of yeast at the filtered centre outlet, indicating effective margination for both kinds of microbes in our device. Due to the larger yeast size dimension (~5 μm), most of them occupied the four corners of the margination channel instead of the entire channel peripheral, resulting in complete margination to the sidewalls and thus better separation

efficiency (Figure 2.9B). This clearly indicates the versatility of the device as it can be used for non-specific removal of pathogens present in blood without any labeling or prior information on the infecting species.

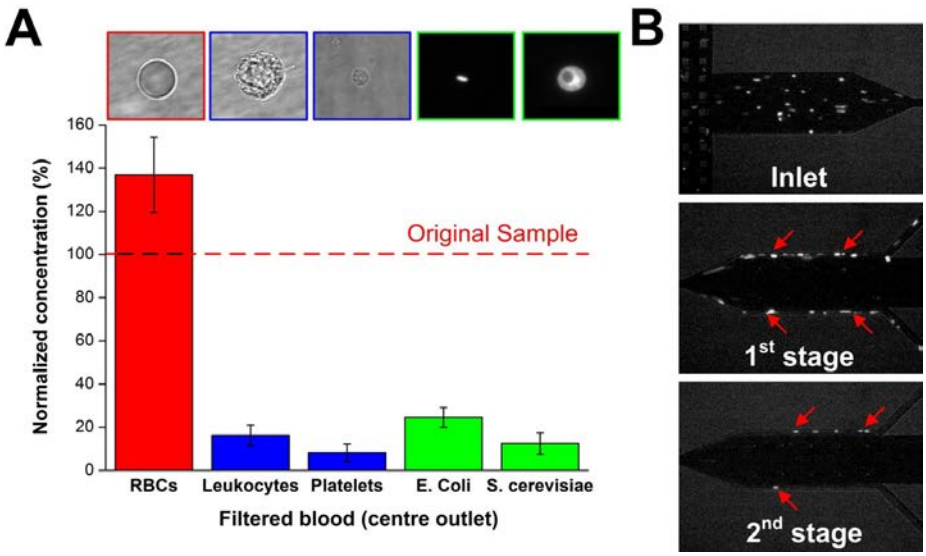

Figure 2.9. Spiked whole blood analysis. (**A**) Normalized concentration of different cellular components at the filtered centre outlet using human whole blood spiked with Escherichia coli and Saccharomyces cerevisiae separately. Optical images (100× magnification) of each component are indicated at the top of their corresponding histogram bar. (**B**) Optical images illustrating yeast filtration at different stages. The larger yeast (~5 µm) undergo margination to the four corners in the straight channel (red arrows), resulting in complete margination to the sides and thus higher separation efficiency.

2.4.6 Multiplexing

In terms of throughput, our single channel design (whole blood processing at ~1 mL/hr) is higher than other reported microfluidic approaches used for blood separation applications, yet significantly slower than conventional macroscale blood purification methods (~1-2 L/hr). To demonstrate the scalability of our device for higher throughput, we designed a parallel system consisting of 6 channels to filter blood simultaneously at ~6 mL/hr (Figure 2.10A). Similar filtration performances were obtained as compared to the single channel device (Figure 2.10B) and the simple experimental setup enables easy and continuous collection of the filtered blood from the two centre outlets. This parallelization scheme can further be extended to larger

devices by stacking layers of devices to achieve even higher throughputs comparable to conventional dialysis systems (Figure 2.10C).

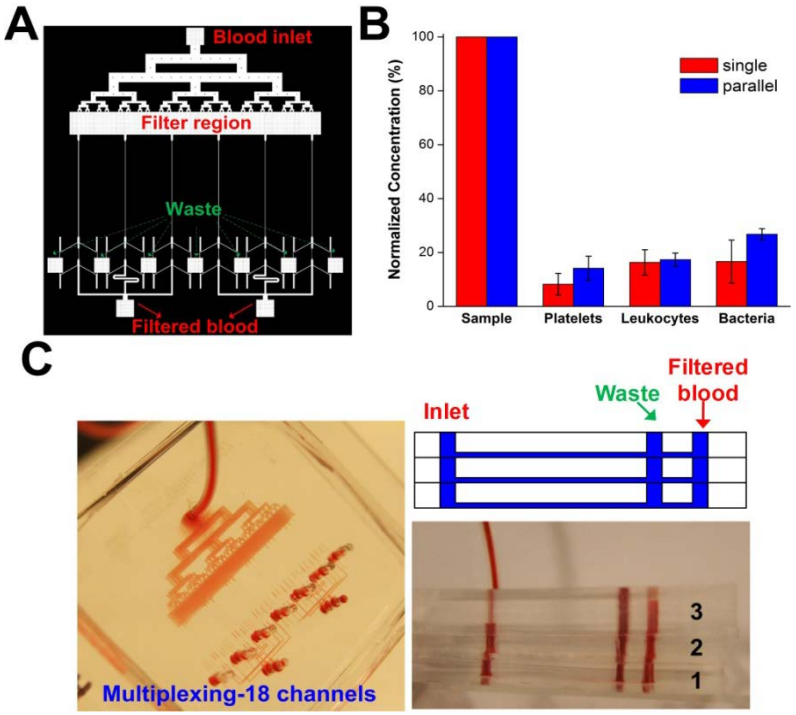

Figure 2.10. High throughput blood filtration using a parallel system. (**A**) Schematic layout of the device consisting of an additional filter region to remove clogs and debris and 6 channels with cascaded design in parallel to achieve higher flow rates. (**B**) Experimental results indicating similar device performances as compared to single channel in removal of different blood components and bacteria using the parallel system at 100 µL/min. (**C**) Illustration of multiplexing through device stacking. Three layers of parallel system (6 channels each) were stacked together, consisting of 18 channels in total to achieve higher throughput (~18mL/hr) for blood filtration applications.

2.4.7 Mouse-model microdialysis

In the next stage of work, we will be collaborating with clinicians from Brigham and Women's Hospital (MA, USA) to study the effect of blood filtration on small-animal model induced with sepsis using murine cecal ligation and puncture (CLP). The rodent CLP model is the most suitable clinical correlate of septic shock/polymicrobial sepsis and multiorgan dysfunction [134], and this pilot study will help determine the feasibility of using the developed microfluidic device as a microdialysis platform in rodent models of sepsis and assess its ability to improve outcomes from sepsis. Using a simple close-loop filtration system

(Figure 2.11), we plan to monitor the clinical outcome of filtered mouse based on survival rate, measurements of blood pressure, concentration of bacteria and circulatory inflammation mediators such as IL-6 in blood over time.

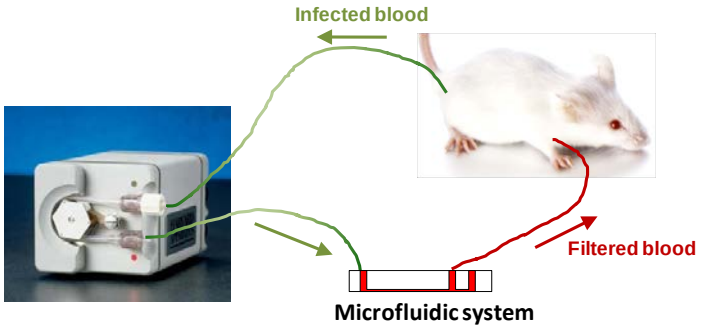

Figure 2.11. Schematic diagram illustrating the proposed microdialysis system using our developed microfluidic device. A peristaltic pump is used to continuously withdraw contaminated blood from the septic mouse into the microfluidic device and return the filtered blood back to the mouse.

2.5 Summary

In this work, a high-throughput microfluidic blood filtration technique for microbial removal from whole blood, inspired by the *in vivo* microcirculatory phenomenon of leukocyte margination was introduced. It has been previously demonstrated both *in vitro* and *in vivo* that RBCs tend to adhere to each other to form rouleaux (or aggregates) at low shear rates (50-600 sec^{-1}) which not only increase the blood viscosity, but also help to exclude the larger and stiffer leukocytes from the axial core of RBCs, resulting in efficient leukocyte margination to the vessel walls [111, 131, 135, 136]. In this work however, the small channel geometry and high flow conditions employed result in significantly higher wall shear rate (~6×10^4 sec^{-1}) whereby RBCs aggregation will be minimal [137] and we postulate that margination of microbes could occur due to Fahreaus effect by the formation of a well-defined RBCs core at the channel centre and hydrodynamic forces arising from intercellular microbe-RBCs interactions. This hypothesis has been demonstrated by us and others who showed that margination of platelets and malaria-infected RBCs can still take place in the absence of RBCs aggregation (by using washed blood and high working flow rates) [91, 119].

Furthermore, Freund also reported that RBCs aggregation is not necessary for leukocyte margination using fluid mechanics simulations and attributed the distinct physical characteristics and hydrodynamics interactions between leukocytes and RBCs as the more important criteria for margination process [138]. Hence, unlike leukocyte margination at low shear rates, RBCs aggregation might not be critical in microbe margination at high flow conditions in our device but further studies are warranted to better understand the actual mechanism responsible so as to improve the channel design for better separation performance.

As an application for sepsis treatment, we demonstrated filtration of *E. coli* and *S. cerevisiae* spiked in whole blood, achieving a high removal efficiency of ~80% and ~90% respectively. Our device not only removes infecting microbial agents from blood, but also allows simultaneous margination and removal of platelets and leukocytes (>80% removal). The rapid removal of both infecting species and immune cells may reduce the concentration of bacterial endotoxin (the main component responsible for inducing inflammatory responses) and production of inflammatory molecules from the activated platelets and leukocytes. This may prevent excessive vascular endothelial damage and potentially help to modulate the host immune response for sepsis treatment. However, the current lack of understanding of the pathophysiology of sepsis makes it difficult to judge how much of the immune cells should be removed. Proper design of the outlet of the channel may allow control over the efficiency of leukocyte, bacteria, and platelets removal to a certain degree to address this challenge. The clinical efficacy of this idea will be verified in animal / clinical testing as future work.

Key advantages in the developed technique include high throughput (~1mL/hr per channel) and label-free separation which allows non-specific removal of any blood-borne pathogens. No sample preparation is necessary and the continuous processing and collection mode enable the return of the filtered blood back to the patient without any post-processing, thereby achieving a simple and complete dialysis circuit setup. Lastly, the device simplicity allows easy multiplexing by channel parallelization or device stacking to further improve the throughput for clinical applications.

3 Enrichment of Malaria-infected RBCs using margination

In this chapter, the physiological phenomenon of leukocyte margination was applied to achieve continuous deformability-based filtration of malaria-infected RBCs (*i*RBCs) in a microfluidic device. As whole blood samples can be used directly in this simple and passive microfluidic device, the technique is ideal for on-site *i*RBCs enrichment for more sensitive diagnosis in resource-limited settings, and can be readily applied to other blood cell diseases such as sickle cell anemia and leukemia which are also characterized by changes in cell stiffness.

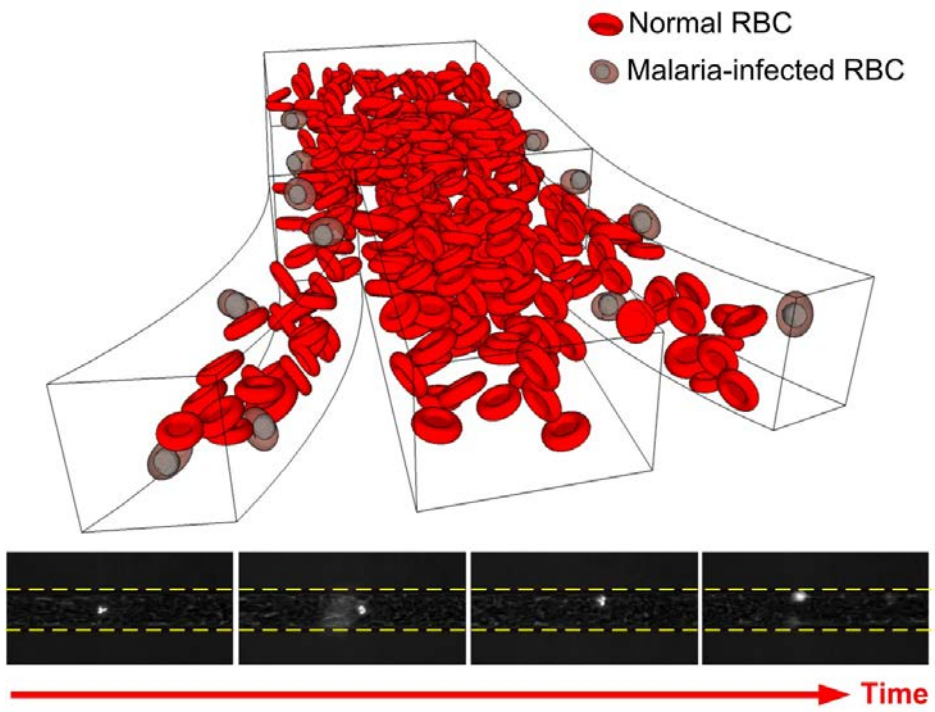

3.1 Background

Malaria is one of the severest parasitic diseases with half of the world's population (3.3 billion) at risk and an estimated 1 to 2 million deaths annually [139]. Of the four types of human malaria species, *Plasmodium (P.) falciparum* is the most deadly. Upon infection, parasites will first enter the human liver and multiply for 8-10 days to form thousands of daughter merozoites. These merozoites are then released into the bloodstream to invade host RBCs and *P. falciparum*-infected red blood cells (*i*RBCs) will undergo various developmental stages (ring, trophozoite and schizont stages) in a 48-hour intraerythrocytic cycle (Figure 3.1). During this period, the parasites continuously remodel the host RBCs machinery and produce parasitic proteins which cause substantial changes in the cell morphology and physiology to promote its own survival [20, 21].

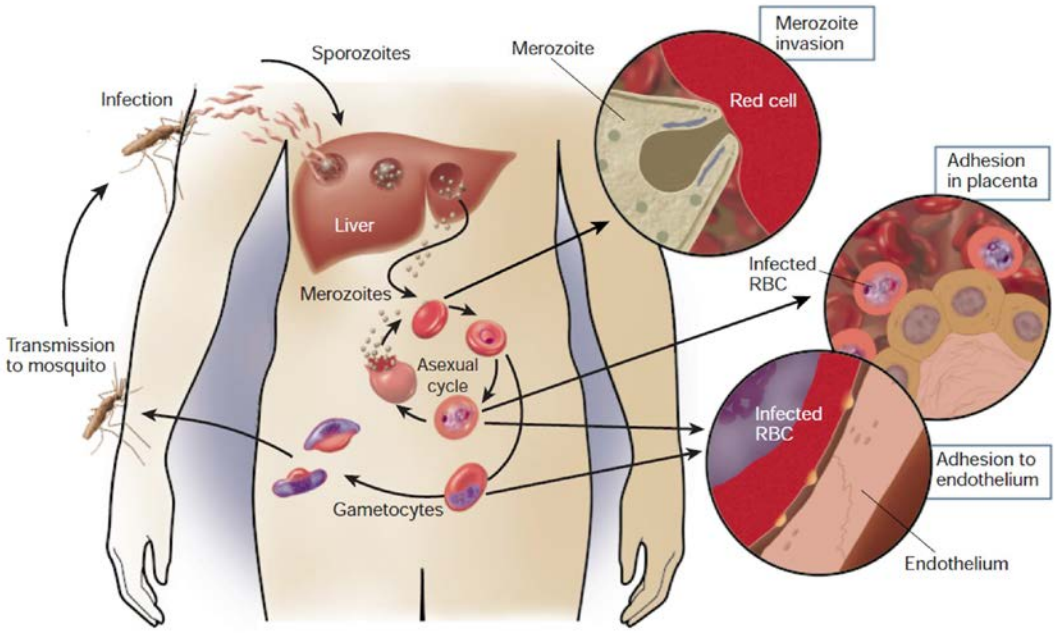

Figure 3.1. Parasite life cycle and pathogenesis of falciparum malaria. Upon infection, the parasites will multiply in the liver for 8-10 days before they are released into the bloodstream to invade the host RBCs. Disease occurs in the asexual blood stage when the parasites undergo various developmental stages (ring, trophozoite and schizont stages) in a 48-hour intraerythrocytic cycle. The *i*RBCs will bind to endothelium or placenta (cytoadherence) for the parasite to avoid clearance by spleen [19].

3.1.1 Physical characteristics of *i*RBCs

Two key morphological changes in *i*RBCs are the reduced cell deformability and increase in cell "stickiness" (adhesiveness). As parasites develop and mature within, *i*RBCs become progressively stiffer and these changes in *i*RBCs rigidity have been extensively studied using different experimental techniques [24-26]. Suresh *et al.* used optical tweezers to stretch and measure the elastic modulus of individual *i*RBCs at different stages of infection (**Table 4**) [24]. This significant change in cell stiffness between various stages is partly attributed to the presence of the large and non-deformable parasites residing within the cells, resulting in a large increase in internal viscosity [140, 141]. As the parasite matures, the discoid *i*RBCs become more spherical with a reduction in surface area to volume ratio leading to reduced cell deformability [141, 142]. Also, release of parasitic proteins stiffens the *i*RBCs membrane by cross-linking and stabilising the spectrin network in the membrane, thus making it less flexible [4, 41]. Recent studies also report that the membrane stiffness of late trophozoite and schizont stages *i*RBCs further increases at febrile temperature, speculating its role in vascular obstruction in microcirculation [143]. Decrease in *i*RBC deformability could lead to several important patho-physiological outcomes. For example, Shevkoplyas *et al.* studied the flow of glutaraldehyde-treated RBCs (with reduced deformability) in a microfluidic device mimicking a microvascular network [144], and showed a decrease in blood flow velocity through the network with increasing RBCs stiffness, resulting in channel clogging and heterogeneous distribution of hematocrit. Other studies have also shown that stiffened RBCs affect the thickness of the cell free layer in a stenosed microchannel [145], and *i*RBCs, especially the late-stage trophozoites and schizonts, *in vivo* mimic the multistep leukocytes recruitment (rolling and subsequent adhesion) on the endothelium [146]. Indeed, cytoadherence in the microvasculature helps the *i*RBCs to evade clearance by spleen which recognizes their loss in deformability. The unique slit-like architecture of the spleen requires RBCs to deform considerably in the narrow interendothelial slits in the venous sinuses [147]. Stiffer *i*RBCs will be retained upstream in the spleen and undergo "pitting" (mechanically

extracting the parasites from the *i*RBCs via mechanical extrusion) which effectively removes the *i*RBCs from the circulation, decreasing the parasitic load.

From the above discussion, one can conclude that cell deformability / stiffness could serve as a relevant biomarker for malaria and other cells. While flow cytometry has been firmly established as a technique to sort cells based on cell surface markers, cell deformability could provide an independent yet physiologically meaningful metric to purify/enrich cells.

Table 4 Classification of *P. Falciparum* infected RBCs at different stages.

Infection stage	Giemsa stained micrograph	Elastic modulus * (μN/m)
Normal RBCs		8
Ring stage		16
Trophozoite stage	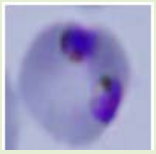	21.3
Schizont stage	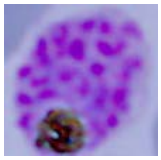	53.3

* Obtained from S. Suresh *et al*. [24].

3.1.2 Malaria detection and diagnosis

The “gold standard” for malaria detection is the microscopic Giemsa-stained blood smear. Peripheral blood from patient is smeared directly onto a glass slide to prepare a thick and thin blood film. The blood films are then stained with Giemsa dye and examined by an experienced microscopist who can yield useful information such as the infecting species and the density of parasitemia. However, lack of skilled technicians, slide preparation techniques,

quality of microscopy, low parasitemia (0.001%), and presence of artifacts may affect the accuracy of the smear and result in false negatives [148].

Immunochromatographic lateral-flow strip test (ICS) is another promising alternative which detects parasitic antigens released from malaria parasites in blood, although with lesser sensitivity than the blood smear method due to fluctuations of parasitic proteins in the body [149]. Other techniques such as mass spectrometry [150], PCR [151], DNA hybridization [152], and UV cytometry [153] have also been used for *i*RBCs detection. However, most of them require the use of specialized equipment or reagents, constant power and refrigeration that are mostly unavailable in resource-poor settings, where malaria infection is most prevalent. More recently, a microfluidic colorimetric immunoassay (designed specifically for resource-limited setting) was reported by Stevens *et al.* to detect parasitic antigens released from malaria parasites in blood, with results generated within 9 min [154], but the sensitivity is not yet up to that of standard Giemsa testing [155]. The detection sensitivity is often limited by the low abundance of the *i*RBCs in the sample blood, which can be addressed better by proper sample preparation (enrichment) strategies.

3.1.3 Current microfluidic approaches for malaria detection

Gascoyne *et al.* used the principle of dielectrophoresis in a microfluidic device for the isolation of *i*RBCs based on the dielectric differences between *i*RBCs and uninfected cells [156, 157] (Figure 3.2A). The group demonstrated high sensitivity (~one infected cell in 10^5 RBCs) and was also able to isolate ring stage *i*RBCs from blood, the primarily circulating *i*RBCs in malaria patients. Recently, Zimmerman *et al.* developed a technique for magnetic separation of *i*RBCs from uninfected ones, known as magnetic deposition microscopy (MDM) [158]. The operating principle relies on the formation of paramagnetic hemozoin nanocrystals within the *i*RBCs fostered by the parasitic digestion of hemoglobin in the host cell. Under the influence of a strong magnetic field, the *i*RBCs were concentrated out of blood and deposited onto a small region of a polyester slide, which was immediately fixed and stained for analysis

(Figure 3.2B**)**. This preconcentration of *i*RBCs increases the sensitivity of diagnosis and can be applied to all Plasmodium species, useful for the detection of a mixed infection. This technique, however, requires sample preparatory steps, as well as strong external magnetic field to be integrated into the microfluidic system. In addition, the absence of hemozoin in ring stage *i*RBCs significantly limits the utility of this technique [159].

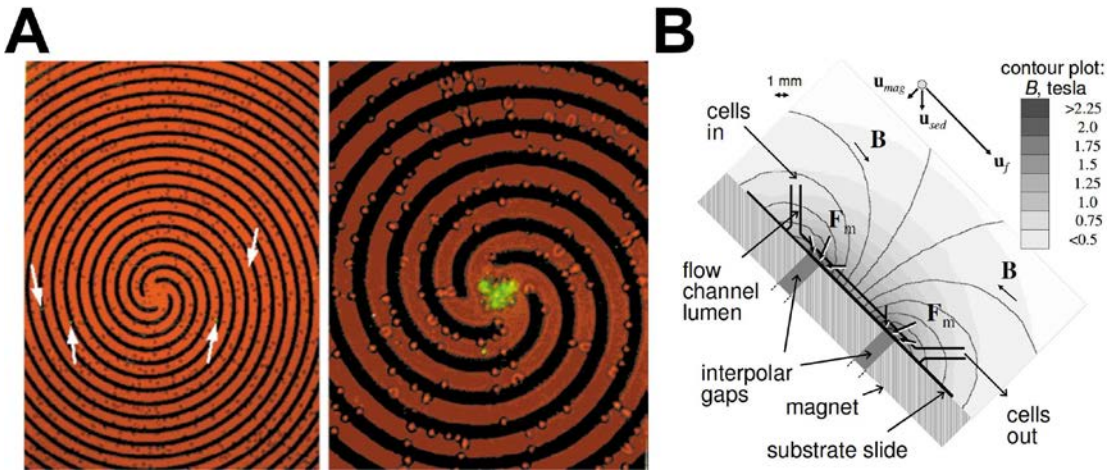

Figure 3.2. Microfluidics systems for malaria separation. (**A**) (left) *i*RBCs (white arrows) were randomly distributed before dielectrophoresis. (right) When the electric field was switched on, uninfected RBCs were trapped at the electrode edges while *i*RBCs (green fluorescence) were levitated and carried towards the centre of the spiral by the travelling field [156]. (**B**) Schematic of the MDM setup illustrating the force vectors acting on the paramagnetic cells (F_m), and magnetic field lines (B) [159]. When sample flow into the channel, paramagnetic *i*RBCs will be concentrated and deposited on substrate at the interpolar gaps while uninfected RBCs will exit the channel.

3.1.4 Motivation

As mentioned in Chapter 2, leukocyte margination in microvessels occurs as leukocytes are significantly different from RBC, both in deformability (stiffness) and size. We have previously demonstrated microbe margination in microfluidic channel, whereby bacteria is smaller but much stiffer than RBCs (>1000×) due to the presence of a rigid cell wall. In this work, however, we investigate if the margination technique can be used in malaria disease for separating normal and *i*RBCs, with the same sizes and only a subtle difference in cell deformability.

3.2 Design principle

The microchannel design consists of a 3cm long, 15×10 µm (*w*×*h*) microchannel with an expanded asymmetrical 3-outlet system (Figure 3.3). Microchannels began with a 100 µm wide segment at the input that constricted to 15 µm; at the output the microchannel opened into a 100 µm wide section to enhance visualization. Before testing with *i*RBCs, the filtration principle was corroborated using hard polystyrene 3 µm beads suspended in whole blood. The 3 µm beads were chosen as they are similar in size to the parasites found in late stage *i*RBCs and are thus representative of the actual *i*RBCs behaviour. The sample consists of whole blood (40-45% hematocrit) spiked with 0.05-0.1% beads or *i*RBCs of different stages. As the blood sample flows through the 15×10 µm microchannel, normal RBCs, which are more deformable than the *i*RBCs, migrate laterally to the axial centre of the channel, displacing the stiffer *i*RBCs towards the channel wall. By designing low aspect ratio microchannels, *i*RBCs are allowed to marginalize only along the channel width and thus align near each sidewall (Figure 3.4). The *i*RBCs are then filtered using the asymmetrical 3-outlet system, thus achieving a continuous high throughput deformability-based filtration.

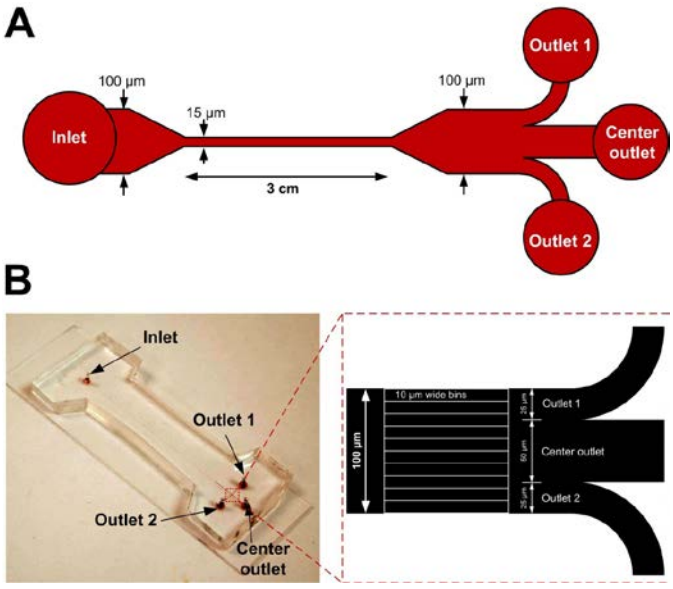

Figure 3.3. (**A**) Schematic of the microfluidic design illustrating the device dimensions. (**B**) Photograph of the 15×10 µm (w×h) microchannel fabricated in PDMS (the microchannel is filled with dye for visualization). The figure also illustrates the output region of the microchannel showing the outlet division and ten equally divided 10 µm wide bins for characterizing the filtration efficiency.

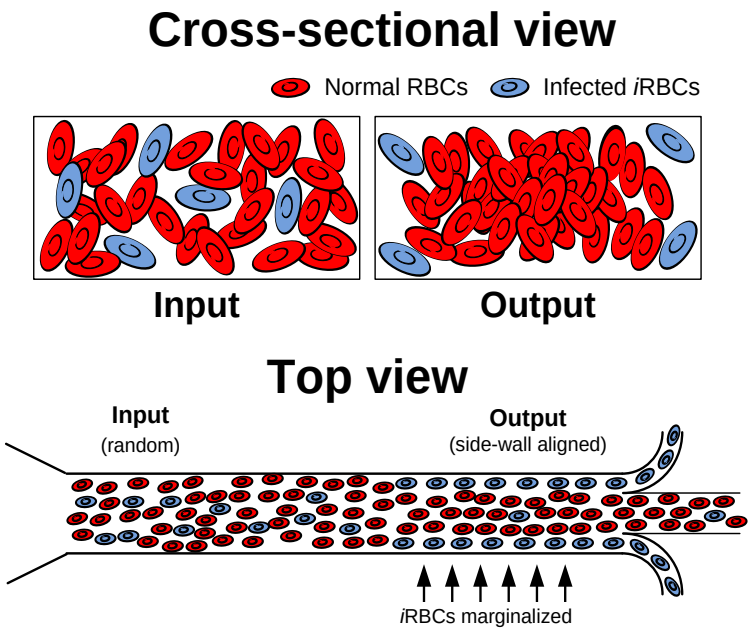

Figure 3.4. Schematic of the cross-sectional and top view of the microchannel illustrating the filtration principle. The randomly distributed *i*RBCs (blue discoid cells) at the microchannel inlet marginate to the channel sidewalls as the flow reaches the outlet and are filtered out using a three outlet system.

3.3 Experimental procedures

The devices were fabricated in polydimethylsiloxane (PDMS) using standard microfabrication soft-lithographic techniques described in Chapter 2.

Malaria culture

P. falciparum 3D7 strain was used in this study. Parasites were cultured in RPMI medium 1640 (Invitrogen, USA) supplemented with 0.3 g of L-glutamine, 5g of AlbuMAX II (Invitrogen, USA), 2 g $NaHCO_3$, and 0.05 g of hypoxanthine (Sigma-Aldrich, USA) dissolved in 1 ml of 1 M NaOH, together with 1ml 10mg/ml of Gentamicin (Invitrogen, USA). Parasites were synchronized at ring stage using 2.5% sorbitol to maintain a synchronous culture. Cultures were stored at 37 ^{o}C after gassing with a 5% CO_2, 3% O_2 and 92% N_2 gas mixture and their hematocrit maintained at 2.5%. Cells were harvested at the ring stage, late trophozoite and schizont stage. Whole blood for parasite culture was obtained from healthy donors and was spun down to separate the RBCs. The RBC pellet was treated with CPDA for 3 days before being washed three times with RPMI 1640 and stored for use.

Sample preparation

The blood sample was washed three times with washing buffer containing 1× phosphate buffer solution (PBS), 2 mM ethylenediaminetetraacetic acid (EDTA) and 1% v/v bovine serum albumin (BSA) prior to running the experiment. Fluorescently labeled microbeads of 3μm diameter (Fluoresbrite® Microspheres, Polysciences Inc, Singapore) were added (0.01% volume fraction) to the blood and resuspended in sample buffer containing 1× PBS, 2mM EDTA, 1% BSA, and 3.5 w/v % dextran 40 (AppliChem Asia, Singapore). The dextran provided the effective viscosity of normal plasma and helped to prevent sedimentation and formation of rouleaux during the experiment [133]. The *i*RBCs (0.01% parasitemia) were stained with 4',6-diamidino-2-phenylindole (DAPI) (Sigma-Aldrich, USA) for visualization and quantification. Final blood suspension was then adjusted to various hematocrits (1%, 10% and 40%) with sample buffer accordingly.

Device characterization

To characterize the microfluidic devices, cell sample was filled in a 1mL syringe and pumped into the microfluidic devices using a syringe pump (Fusion 400, Chemyx Inc., USA) driven at varying flow rates. Flow was experimentally observed using an inverted epi-fluorescence microscope (Olympus IX81, Olympus Inc., USA) equipped with a 12-bit EMCCD camera (iXon^{EM}+ 885, Andor Technology, USA). During testing, high speed images of the channel were captured at the outlet using Metamorph® software (Molecular Devices, USA).

To quantify the device performance, the dispersion of the fluorescently labeled microbeads and *i*RBCs was measured from the images taken at the microchannel outlet. Microbeads and *i*RBCs dispersion was measured by dividing the 100 μm wide outlet microchannel into 10 equal bins of 10 μm each and counting the number of beads and *i*RBCs passing through each bin [160] (Figure 3.3B). The count was then plotted to show the distribution of the beads/*i*RBCs across the channel width. Filtration efficiency was determined by normalizing the beads/*i*RBCs count measured at the side outlet to the total outlet count. For complete filtration, all the beads/*i*RBCs are expected to migrate to the two channel sidewalls and

effectively filtered from the two side outlets. The device performance was further verified by performing Fluorescence Activated Cell Sorting (FACS) analysis using BD™ LSR II flow cytometer (BD Biosciences, USA) on the collected outlet samples.

3.4 Results and discussion

3.4.1 3µm beads characterization

To validate the phenomenon of deformability-based lateral displacement in concentrated blood flow, rigid 3 µm fluorescently labeled polystyrene beads were tested because of the similarity in size with the parasites (3 to 5 µm) found in late stages *i*RBCs. As the stiff parasites are mainly responsible for the loss of deformability in infected cells [141], 3 µm beads gives a good representation of *i*RBCs flow behavior. The beads were added into blood suspensions of 1%, 10% and 40% hematocrit and pumped through the device at varying flow rates. The filtration efficiency was quantified by counting the beads passing through each bin location. For consistency, we counted a total of 200 beads for each experiment. Figure 3.5 plots the beads distribution across the microchannel width for varying flow rates. At low hematocrit (1% Hct), the beads and RBCs remained uniformly dispersed across the channel width, indicating negligible axial migration and margination. Increasing the hematocrit to 10% and 40% results in the formation of a well-developed RBC dominated core at the microchannel center. Due to strong interactions between the beads and RBCs, almost all the beads (>90%) were displaced towards the channel sidewalls (bins 1 and 10 in Figure 3.5B-C). These results are in accordance to those reported by others, suggesting the role of high hematocrit for cell margination [115, 131].

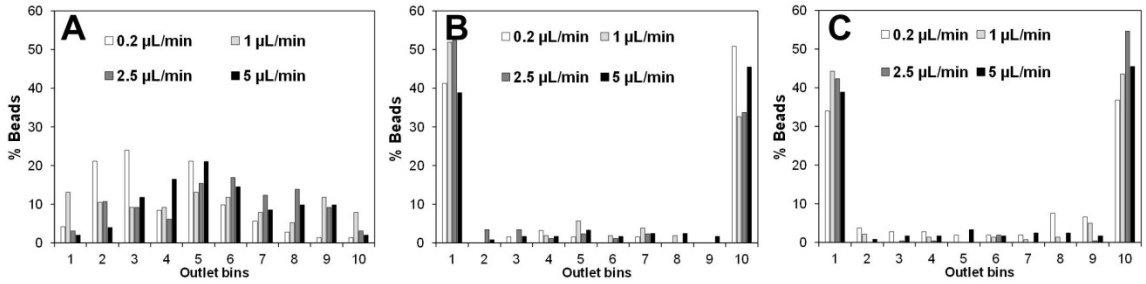

Figure 3.5. Histogram showing the normalized 3 µm beads distribution at the microchannel outlet for varying flow rates in (**A**) 1% hematocrit, (**B**) 10% hematocrit and (**C**) 40% hematocrit samples.

Figure 3.6 presents the 3 µm beads distribution measured at the side outlets and the center outlet arm for varying hematocrit samples. All experiments were conducted at a fixed flow rate of 5 µL/min. At 1% hematocrit, the centre outlet had approximately twice as many beads than the side outlets. This is attributed to the higher velocity at the microchannel center (Poiseuille flow), resulting in more number of beads passing though the center in a given time period. However, at higher hematocrit (10% and 40%), almost all the beads (~ 90%) were displaced to the channel sidewalls and collected by the side outlets. The filtration efficiency also increased from 89% to 97% as the hematocrit was increased from 10% to 40%, indication increased margination [119].

A high hematocrit sample is required for improved lateral displacement of beads in our microchannel. Next, experiments were conducted to determine the effect of flow rate on margination efficiency. Based on the results presented in Figure 3.6A, a 40% hematocrit sample spiked with fluorescently labeled beads was tested at flow rates ranging from 0.2µL/min to 5µL/min. Figure 3.6B presents the 3 µm beads distribution measured at the side outlets and the center outlet arm for increasing flow rates. The bead margination efficiency remained approximately constant at ~90% at all tested flow conditions, consistent with other recently reported results [119]. This behavior can be accounted for by the following reasons. At lower flow rates the rigid beads take longer to traverse the channel length, thus allowing sufficient time for multiple cell interactions for lateral margination. However when the flow rate is increased, due to higher inertia, RBCs migrate faster to the axial center of the

microchannel forming a well-defined core. This results in the rigid beads being "pushed" away from the center towards the sidewalls, thus achieving efficient filtration even at higher flow rates.

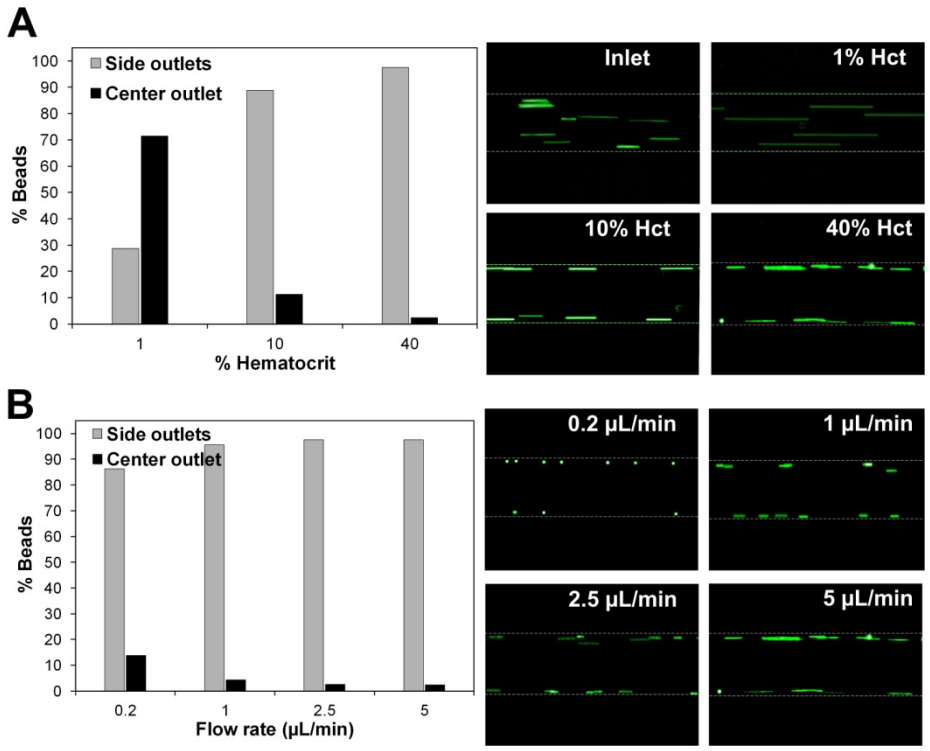

Figure 3.6. (**A**) Filtration efficiency of 3 µm beads at the side outlets for varying sample hematocrit at 5 µL/min flow. (**B**) Filtration efficiency of 3 µm beads at the side outlets at varying flow rates in 40% hematocrit sample. Also, shown in the figure are fluorescent images indicating the beads distribution (fluorescently labeled green) across the channel cross-section at the outlet. (white dotted lines indicate the approximate channel wall boundaries).

3.4.2 *i*RBCs characterization

Following the validation of the design principle with the experiments using polystyrene beads, we tested *i*RBCs reconstituted in 10% and 40% hematocrit blood samples. Initially, all tests were done using late trophozoite/schizont stages *i*RBCs, as the margination effect would be more prominent due to their increased stiffness when compared with the early stage *i*RBCs. Figure 3.7 presents the *i*RBCs distribution results measured at the microchannel outlet for 10% and 40% hematocrit at varying flow conditions. At 10% hematocrit, contrary to the results obtained with the hard polystyrene beads, we see negligible *i*RBCs marginating towards the

side walls. The *i*RBCs count indicates a parabolic distribution around the channel axial center, consistent with the Poiseuille velocity profile. This suggests that the difference in deformability between the *i*RBCs and normal RBCs is not sufficient to displace the *i*RBCs towards the sidewalls with moderate cell-cell interactions.

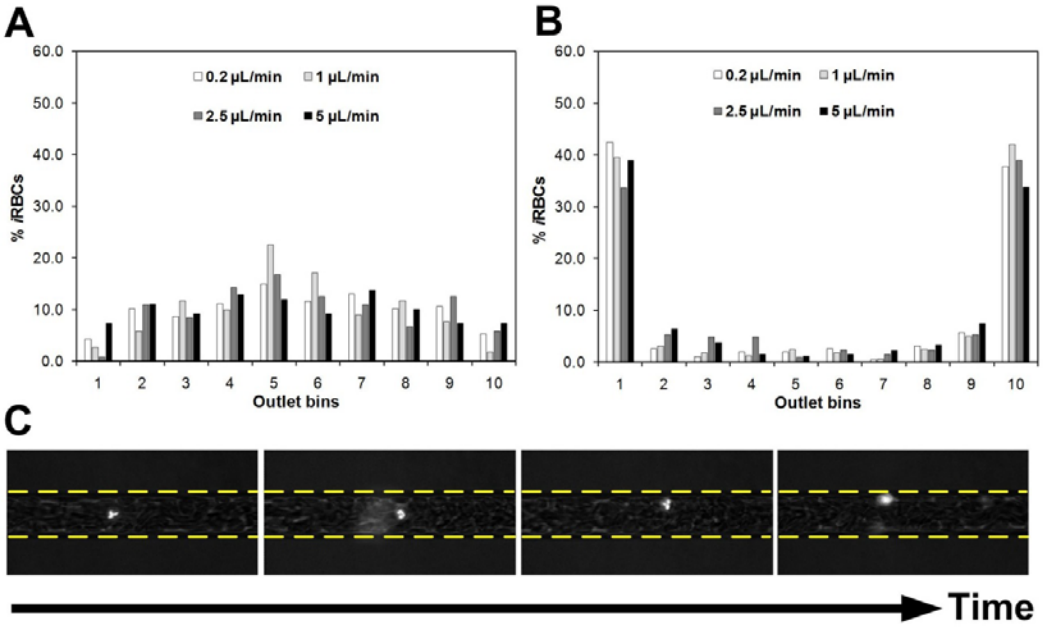

Figure 3.7. Histogram showing the normalized *i*RBCs distribution at the microchannel outlet for varying flow rates in (**A**) 10% hematocrit and (**B**) 40% hematocrit samples. Contrary to the 3 µm bead results, no *i*RBCs margination is observed at 10% hematocrit. At 40% hematocrit, ~80% *i*RBCs marginate to the sidewalls for all flow conditions. (**C**) Sequential images showing the actual margination of a stiffer *i*RBC (DAPI-stained) in the straight channel region in 40% hematocrit sample. (yellow dotted lines indicate the approximate channel wall boundaries).

However, increasing the hematocrit to 40% results in significant *i*RBCs margination (Figure 3.7B). From the figure, ~80% *i*RBCs were displaced to bins 1 and 10 for all flow conditions, similar to the results obtained with the polystyrene beads. The margination effect was observed at all flow rates tested, suggesting that the hematocrit is the main factor for *i*RBCs margination. Tracking video analysis also shows the actual displacement of an *i*RBC in the straight channel region in 40% hematocrit sample, indicating that higher hematocrit facilitates increased cell-cell interactions and displacement of the stiffer *i*RBCs to the channel sidewalls (Figure 3.7C). Figure 3.8 presents the margination efficiency of *i*RBCs for varying flow rates.

It is important to note that the technique worked equally well at all tested flow conditions including high flow rates (5 µL/min), an important consideration for high-throughput separation. As expected, the *i*RBCs margination efficiency was not as high as that measured with hard beads since *i*RBCs are still deformable and thus marginalize less efficiently to the sides.

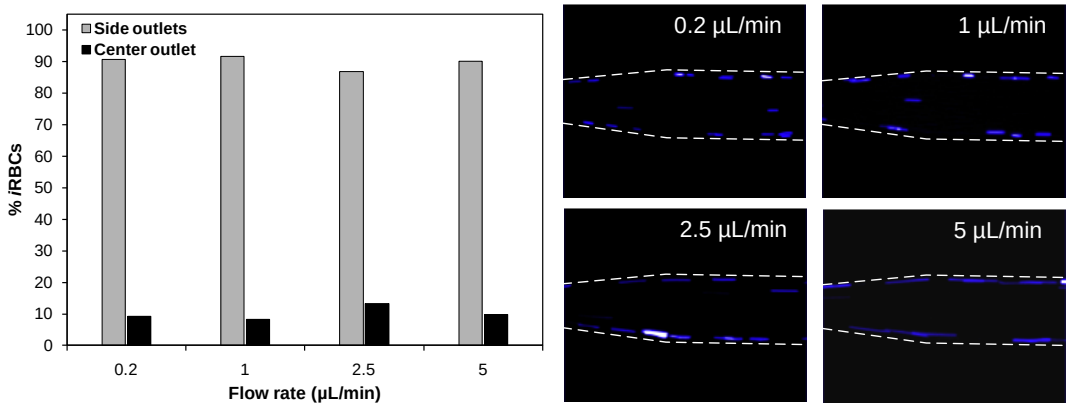

Figure 3.8. Filtration efficiency of late trophozoite/schizont stage *i*RBCs at the side outlets at varying flow rates in 40% hematocrit sample. Also, shown in the figure are fluorescent images indicating the DAPI-stained *i*RBCs distribution (fluorescently labeled blue) across the channel cross-section at the outlet. (white dotted lines indicate the approximate channel wall boundaries).

To verify the accuracy of the filtration efficiency, the outlets samples were also analyzed using FACS. Both ring stage and late trophozoite/schizont stages *i*RBCs at 40% hematocrit blood suspension were pumped through the device at 5 µL/min and the outlets were collected and analyzed using FACS. For experiments with late trophozoite/schizont stages *i*RBCs, 92% filtration efficiency was measured between the side and center outlets, consistent with the bin-counting data (Figure 3.9A). The *i*RBCs concentration at the side outlets show 2× enrichment compared to the inlet sample, as the side outlets account for 50% volume flow (1:2:1) of the three outlets. However, this enrichment can be further improved by using a cascading scheme on samples collected from the side outlets and by designing optimally bifurcated outlets.

To apply this *i*RBCs margination for malaria diagnostics, it is important to enrich the ring stage *i*RBCs. Typically, in malaria-infected patients, late stages (trophozoite/schizont) *i*RBCs would sequester in the post-capillary venules and only the ring stage *i*RBCs are observed

circulating in the peripheral bloodstream for detection of malaria infection [150, 156]. Margination efficiency of the technique for ring stage *i*RBCs were tested under optimized separation conditions (40% hematocrit, 5 μL/min), and the collected outlets were analyzed using FACS (Figure 3.9B). Ring stage *i*RBCs are only marginally stiffer than uninfected cells due to a reduction in cell surface area to volume ratio and stiffening of the cell membrane [24, 141, 142]. However, even this subtle difference in deformability can be exploited using this phenomenon of margination for *i*RBCs filtration. Understandably, the efficiency of ring stage *i*RBCs is lower than late stages *i*RBCs and our results indicate that ~80% ring stage *i*RBCs marginated towards the channel sides. We believe this can be further improved using longer microchannels, thus allowing the ring stage *i*RBCs sufficient time to marginate entirely to the sidewalls. Also, by appropriately dividing the outlets (for example using a 1:10:1 width ratio rather than 1:2:1 ratio between the three arms) the developed microfluidic device can also be used as an enrichment tool for malaria diagnosis with improved detection sensitivity at low parasitemia.

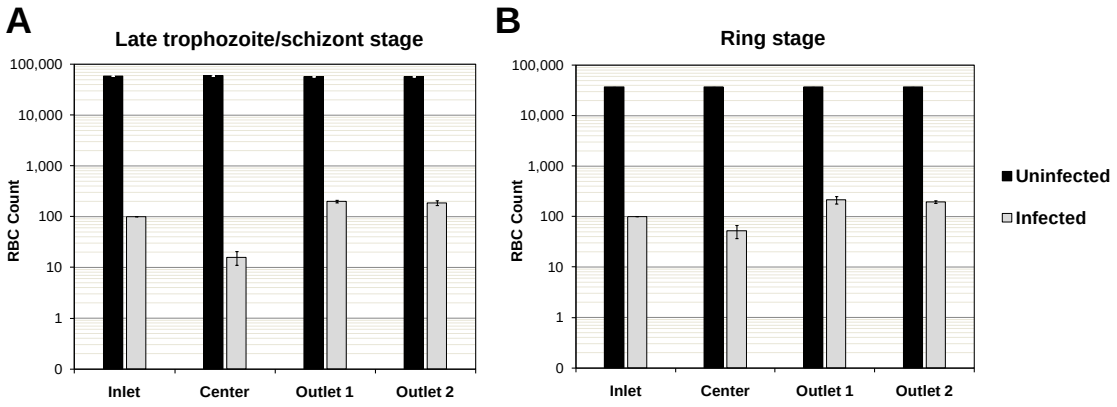

Figure 3.9. Flow cytometry (FACS) data indicating concentration of *i*RBCs and normal RBCs collected at the three outlets. The plots (log scale) illustrate the counting results indicating the distribution of *i*RBCs across the three outlets for (**A**) late trophozoite/ schizont stage and (**B**) ring stage *i*RBCs samples. The results indicate a filtration efficiency of >90% for late trophozoite/schizont stage *i*RBCs and ~80% for early ring stage *i*RBCs.

3.4.3 Whole blood analysis

Lastly, we conducted experiments with whole blood to determine the effect of leukocyte interference with the *i*RBCs margination. As expected, >80% of both *i*RBCs and leukocytes were collected at the side outlets, indicating that leukocyte margination has little effect on *i*RBCs migration, thus ensuring a high recovery of infected cells from whole blood analysis (Figure 3.10). As leukocytes are typically larger than RBCs, future designs can include a highly dense pillar structures at the channel inlet to filter out the larger leukocytes.

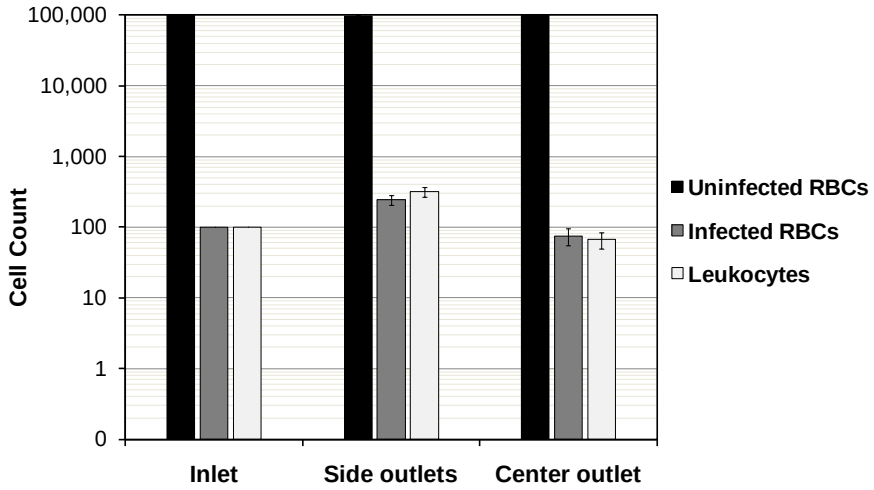

Figure 3.10. Flow cytometry (FACS) data of *i*RBCs spiked into whole blood. The plot indicates the distribution of RBCs, *i*RBCs and leukocytes collected at the outlets, with a filtration efficiency of >80% for both *i*RBCs and leukocytes from the side outlets.

3.4.4 Improvement in *i*RBCs enrichment ratio

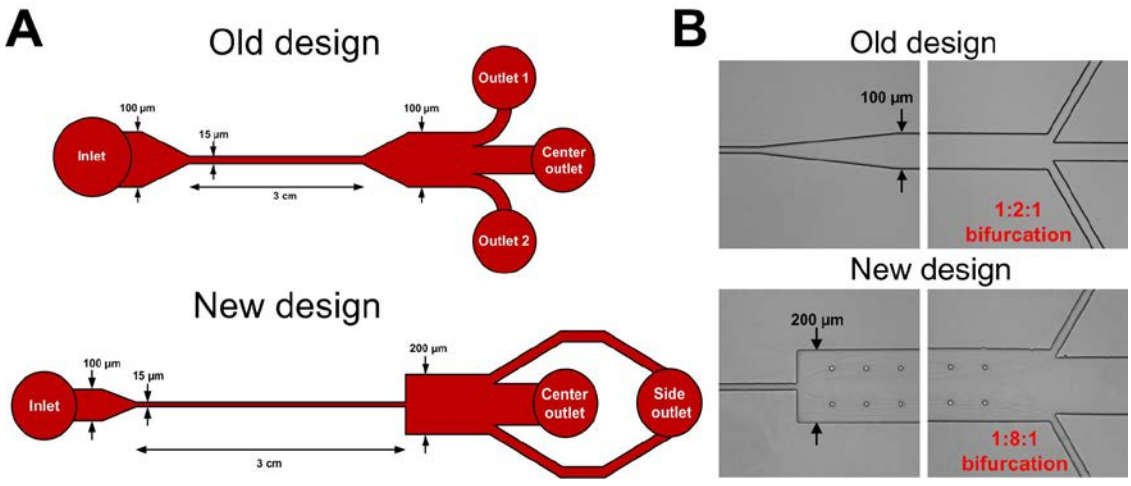

Figure 3.11. (**A**) Schematic diagram showing comparisons between the old and new channel designs. (**B**) Optical images of the fabricated old and new PDMS devices illustrating the changes in the new design. Instead of a tapered opening of 100 µm width at the channel end, the new design consists of an abrupt expansion which is 200 µm wide. Pillars are added at the centre region to prevent the channel from collapsing during fabrication. Bifurcation ratio also changes from 1:2:1 to 1:8:1 so that the side outlets are smaller which minimize the number of uninfected RBCs from entering.

Several geometrical changes were made in the new channel design to improve the *i*RBCs enrichment ratio. Firstly, instead of using a tapered opening at the channel end, an abrupt expansion was used to enhance the cell-free layer (Figure 3.11). This is useful because most of the marginated *i*RBCs are located outside the RBC core upon exiting the straight channel. Hence these *i*RBCs would have higher chances residing in the larger cell-free layer next to the channel sides. Other changes made include increasing the expansion channel width from 100 µm to 200 µm and changing the outlet bifurcation ratio from 1:2:1 to 1:8:1.

As shown in Figure 3.12, the marginated *i*RBCs were mostly flowing within the enhanced cell-free layer in the abrupt expansion design. With a smaller side outlet bifurcation (1:8:1), less uninfected RBCs are entering the side outlets during separation, giving rise to an improvement in *i*RBCs enrichment factor to ~7×. Experimental results also indicate that the enrichment factor decreased at higher parasitemia. From our captured videos, it was observed that *i*RBCs overcrowding occurred at the channel sides at high parasitemia, resulting in secondary *i*RBCs-*i*RBCs interactions which led to some of them being displaced to the centre again. Nevertheless, parasitemia in malaria patients is usually less than 0.1% and *i*RBCs overcrowding problem will not be significant when testing actual samples from malaria patients. The results presented here also clearly demonstrate that *i*RBCs enrichment factor can be improved by simply changing the channel geometry and dimensions. Future work will include optimizing the channel designs (e.g. cascade scheme) to improve both throughput and enrichment factor.

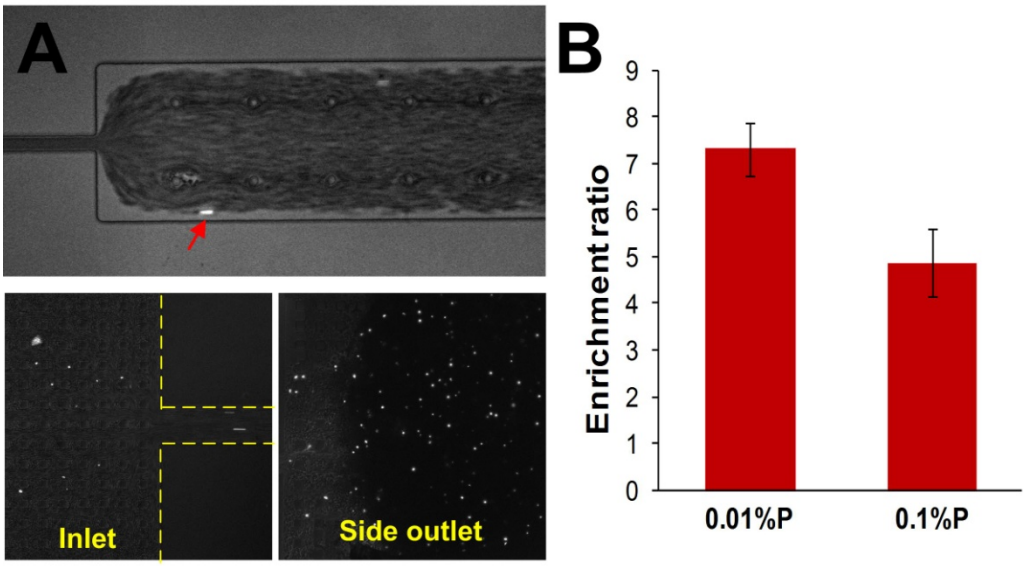

Figure 3.12. (**A**) *top* Optical image showing a marginated *i*RBC (DAPI-stained, red arrow) residing in the enhanced cell-free layer in the abrupt expansion design. *bottom* Snapshots at the channel inlet and side outlet indicate an increase in *i*RBCs concentration (fluorescence labelled) after margination in our new device. (**B**) Plot showing an improved enrichment of ~7× in the new device. Enrichment factor decreases at higher parasitemia (P) due to *i*RBCs overcrowding and *i*RBCs-*i*RBCs interactions at the sides after margination.

3.4.5 Pathological Significance

In this work, we demonstrate, for the first time, that stiffer *i*RBCs behave like leukocytes and undergo margination towards the side walls. This demonstration provides insights into the hemodynamic effects of *i*RBCs microcirculation and its pathophysiological significance to cytoadherence. As mentioned earlier, two key morphological changes in *i*RBCs are the increase in adhesiveness of the *i*RBC membrane and reduced deformability. These changes are pivotal in severe malaria pathogenesis leading to cytoadherence of *i*RBCs to various types of host cells. Margination of these *i*RBCs to the capillary walls also leads to sequestration at the venular blood capillaries, responsible for capillary blockages and comprising the microcirculation [27, 161]. Ho *et al.* have shown *in vivo* that *i*RBCs cytoadherence to endothelium mimic the multistep leukocytes recruitment, such as rolling and adhesion, and this process occurs in both human post capillary venules and the arteriolar vasculature [146]. The results presented here clearly illustrate the rigid late trophozoite/schizont stage *i*RBCs

being laterally displaced and flowing at the periphery of the microchannels. This, *in vivo*, would favor their entrance into the small branching side capillaries, resulting in subsequent *i*RBCs sequestration in the capillary bed. We also tested *i*RBCs margination over a wide range of flow conditions (*Re*= 0.01-2.22), similar to physiological arteriole flow [9], further confirming the role of reduced deformability to *in vivo* sequestration and cytoadherence.

Lastly, to study the effect of *i*RBCs margination on microcirculatory flow behaviour, we designed another microfluidic device consisting of a 2cm long margination channel (15µm (*w*) ×10µm(*h*)) connected to an array of bifurcating channel network with capillary-like dimensions (smallest channel is 5 µm width). As shown in Figure 3.13A, the capillary network is symmetrical and can be divided into 9 equal bins for characterization. Preliminary experiments were conducted as whole blood samples spiked with late stages *i*RBCs (~0.01% parasitemia) were pumped into the device at physiological pressure (~4kPa) and *i*RBCs flow distribution into the capillary network was monitored. As expected, there was an uneven distribution of *i*RBCs flowing into the capillary network after margination, with more *i*RBCs entering the side branches (bin 1-3, bin 7-9) (Figure 3.13B). This has important implications in the sequestration or cytoadherence pattern in the capillary region. For example, because there were lesser *i*RBCs entering the central capillary channels (bin 4-6) after margination, most of the channels remained functional as compared to the side capillary channels (bin 1-3, bin 7-9) which have a significant number of blocked channels after 30 minutes (Figure 3.13C). The channel blockage occurred most probably due to 1) the reduced deformability of *i*RBCs which resulted in slower flow through the channels and 2) increase in *i*RBCs surface adhesiveness which facilitated the non-specific binding of *i*RBCs to the channel wall. Future work include coating the capillary channels with different proteins (ICAM-1, CD36), which are the main ligands involved in *i*RBCs cytoadherence to create a more *in vivo* microenvironment for cytoadherence studies.

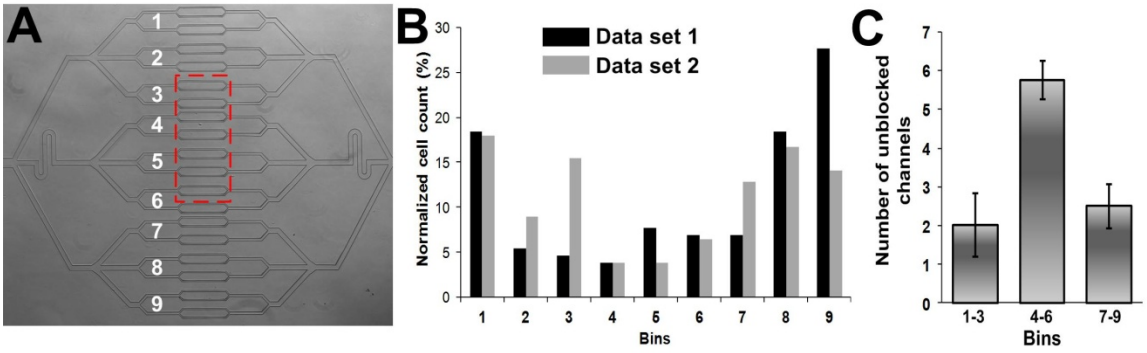

Figure 3.13. (**A**) Optical image showing the layout of the capillary channel network, which can be divided into 9 equal bins for characterization. The smallest channel dimension is 5 µm located at the middle section (indicated in red dashed box). (**B**) Histogram plot showing an uneven distribution of *i*RBCs into the capillary network after margination. (**C**) Plot indicating the number of functional (unblocked) channels remaining after 30 minutes.

3.5 Summary

Here, a continuous deformability-based *i*RBCs filtration method in a microfluidic device based on biomimetic cell margination was introduced. We demonstrated, for the first time, that stiffer *i*RBCs behave like leukocytes and marginate towards the side walls under physiological conditions. Our results indicate that high sample hematocrit (40%) was critical for optimal *i*RBCs margination, observed over a wide range of flow rates. The reported results indicate a high filtration efficiency of ~80% for early ring stage *i*RBCs and >90% for late trophozoite/schizont stage *i*RBCs. We also showed that by changing the channel geometry and dimensions, the *i*RBCs enrichment factor can be improved to ~7×. However, further optimization is necessary to increase both throughput and enrichment factor so that the developed technique can be clinically useful for malaria diagnostic applications. Lastly, the effect of *i*RBCs margination on microcirculatory flow behaviour was investigated using another microfluidic design consisting of a margination channel connected to an array of bifurcating channel network with capillary-like dimensions. Our preliminary results showed that there was an uneven *i*RBCs distribution flowing into the capillary network after margination, which could have important implications in the cytoadherence/sequestration pattern. Although the current design does not completely represent the *in vivo*

microvasculature (such as square cross-section channels instead of circular ones), we envision such microfluidic devices with capillary channel network could serve as a more relevant microfluidic platform for cytoadherence studies due to the physiological shear conditions and geometrical constraints generated in these small channels.

For malaria diagnostic application, the developed margination technique offers many distinct advantages over other microfluidic separation methods. First, continuous operating mode enables a high sample throughput (5μL/min, ~20 million cells/min), enhancing detection sensitivity at low parasitemia [156, 158]. Passive operating principle eliminates the need to integrate an external force field for functionality and the low-cost and disposable nature of the device makes it ideal for outfield settings. As whole blood from patients can be tested directly, sample preparatory steps are not necessary unlike other microscale separation techniques [158, 159], further reducing processing time. Also, as no special chemicals or antibodies are needed, it helps to solve reagent storage problems which are a major concern for malaria-affected countries that suffer from hot and humid weather and lack refrigeration [154]. Finally, as the separation principle is based on deformability differences as an intrinsic biomarker, the device can be readily applied to other blood cells diseases such as sickle cell anemia and leukemia which are also characterized by change in cell stiffness.

4 Circulating tumour cells (CTCs) separation using pinched flow coupled shear-modulated inertial microfluidics

In this chapter, we apply shear-modulated inertial microfluidics to isolate CTCs from blood using a high aspect ratio microchannel patterned with a contraction-expansion array. The design simplicity allows easy parallelization with the ability to process millilitres of blood samples within minutes. By varying the 'pinching' width, the device design can also be easily customized for isolating other rare-cells from blood including leukocytes and fetal nucleated red blood cells.

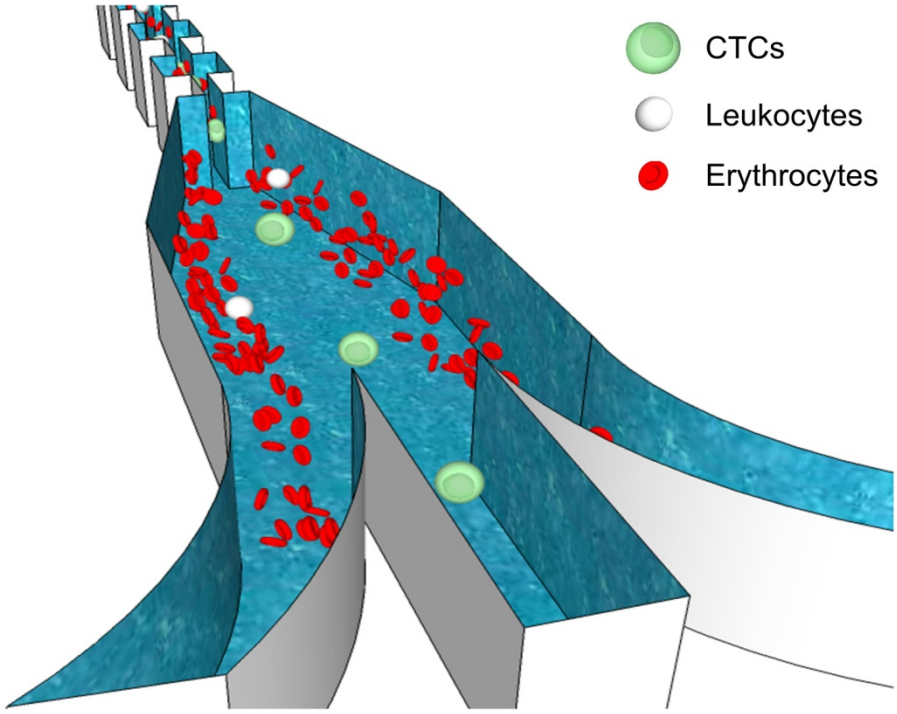

4.1 Background

4.1.1 CTCs as biomarker in clinical management

Cancer metastasis is a highly complex, multi-stage process which involves the dissemination of tumor cells from a primary site to other parts of the body to form new tumors. Although it is generally considered an inefficient process with only a small subset of tumour cells (< 0.01%) that enter the bloodstream eventually forming metastases, cancer metastasis accounts for ~90% of all cancer related deaths [162, 163]. During metastasis, viable tumour-derived epithelial cells (circulating tumour cells or CTCs) have been identified in peripheral blood from patients with metastatic carcinomas (solid tumours derived from epithelial tissues) and are probably responsible for extravasation at distant organs to form new metastatic sites (Figure 4.1) [39]. Interestingly, the first report on blood-borne cells shed by a solid tumor was by an Australian pathologist Thomas Ashworth more than a century ago in 1869 [164]. However, with technological advances which lead to better understanding of the disease, it was only until the late 1990s when scientists and clinicians began to realize the significance of CTCs and their potential applications in cancer diagnosis and therapeutic applications.

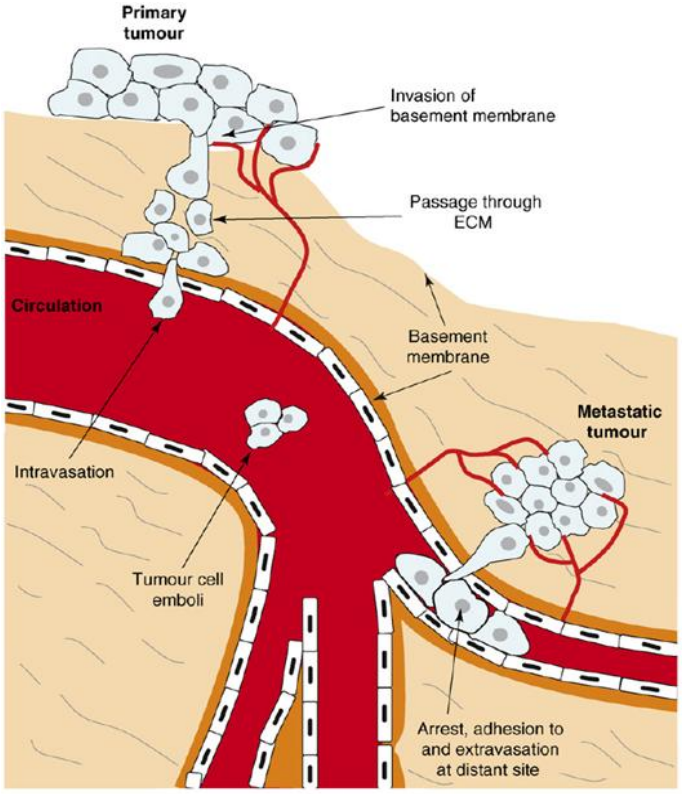

Figure 4.1. Schematic diagram showing the different stages in cancer metastasis [22]. The circulation of CTCs in the bloodstream is an important intermediate step for the cancer cells to form secondary tumours at distant sites.

In clinical settings, clinicians use medical history, physical examination, radiographic imaging and serological analyses for cancer markers to assess the conditions of cancer patients. However, the reliability and accuracy of these techniques depend significantly on the disease stages and vary among patients [165]. In the last decade, enumeration of CTCs in blood has received wide attention because of its potential as a biomarker for clinical evaluation in cancer patients. Detection of CTCs can provide valuable insights associated with disease stages and cancer progression [36, 37] and clinical reports have shown that breast cancer patients with more than five CTCs per 7.5ml of blood have a much lower survival rate than patients with fewer cells [37]. Besides prognostic significance, CTCs enumeration is also used for monitoring therapeutic treatment response [38] and may even provide a more accurate determination of disease status than classical clinical testing [36].

4.1.2 Current methodologies for CTCs isolation

As CTCs are extremely rare, comprising as few as one cell per 10^9 hematologic cells with highly heterogeneous morphologies and molecular signatures, their isolation from blood has been a technical challenge [39]. In general, CTCs isolation/enrichment can be based on physical or immunomagnetic separation. Physical enrichment of CTCs include density-gradient centrifugation which produces a mononucleocyte fraction that contains CTCs due to their similar buoyant density, RBCs lysis to extract only mononuclear cells, and physical filtration such as ISET (isolation by size of epithelial tumour cells) to trap larger CTCs (> 8μm) individually on filter pores [166]. For immunomagnetic enrichment, antibodies against adhesion molecules (such as EpCAM) that are commonly expressed on malignant epithelial cells are functionalized on magnetic particles which will bind specifically to CTCs in blood and can be separated magnetically. The CellSearch system (Veridex™, Warren, PA), which is the only US FDA-approved CTCs assay currently, is an example that enriches CTCs by ferrofluids coated with EpCAM, followed by immunostaining for detection. Although these techniques have achieved relatively good separation efficiency and isolation purity, major

drawbacks include long processing time and laborious experimental procedures. As multi-steps sample preparation are required, it may result in cell contamination or cell loss, thereby affecting the sensitivity and specificity of the cell assay result. Moreover, viability of CTCs is also lost as cell fixation and labeling are required in most of these techniques.

4.1.3 Microfluidics approaches for CTCs separation

Microfluidic approaches for CTCs separation has emerged as an attractive alternative as it can produce a fully enclosed and integrated system to process clinical samples, which helps to minimize sample loss and provide a more sensitive enumeration of CTCs. Various microdevices utilizing different separation principles such as physical filtration using micro structures [69, 70, 167], dielectrophoresis [168], affinity-based sorting using functionalized channels or micropillars [83, 85, 169, 170], and self-assembled functionalized superparamagnetic particles [171] have been successfully applied for CTCs enrichment and separation (Figure 4.2).

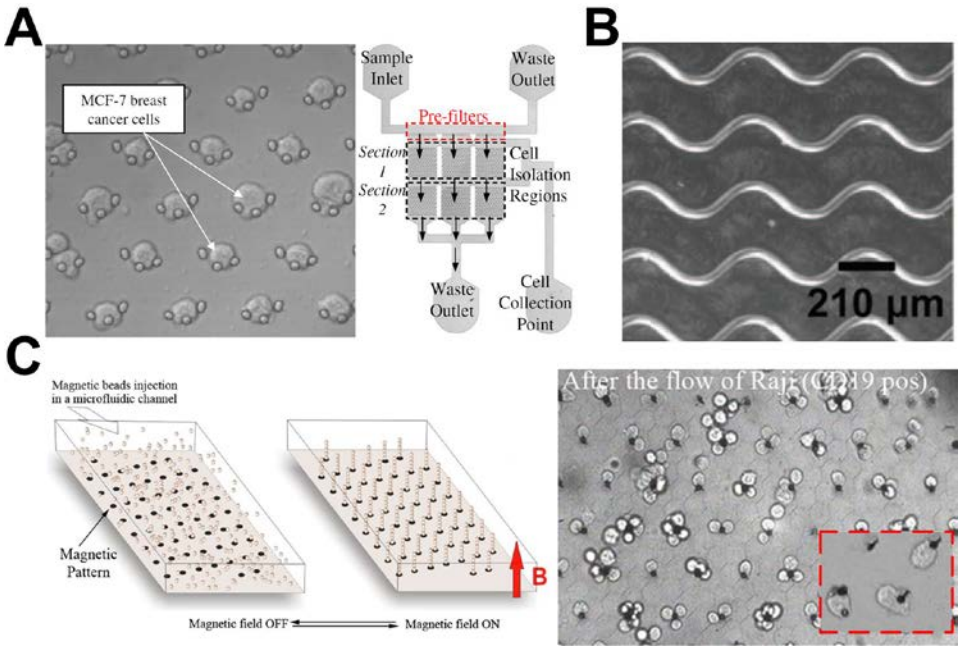

Figure 4.2. (**A**) Overview of the microdevice layout and cancer cell isolation region using crescent-shaped structure [69]. (**B**) SEM image showing the sinusoidal channels coated with EpCAM for CTCs capture [169]. The sinusoidal channels improve the capture efficiency for CTCs at high flow rates. (**C**) Principle of magnetic self-assembly. The application of an

external vertical magnetic field results in the formation of a regular array of functionalized bead columns on a pre-defined pattern. Optical image shows the immuno-capture of Raji cells on the beads during flow. Inset (red box) shows a magnified view of the captured cells [171].

In physical filtration devices, clogging is commonly encountered when processing whole blood, thus affecting the isolation efficiency and purity. Also, these methods are limited to low flow rates as high pressures can typically lower the CTCs trapping efficiency. In immuno-mediated enrichment, the use of surface antigens such as EpCAM and HER-2 is less desirable as their expression levels varies widely for different or even same tumor type and retrieval of isolated CTCs may be difficult due to cell binding in the device [172]. Moreover, there is a risk of losing the most aggressive CTCs subpopulation due to epithelial to mesenchymal transition (EMT), which leads to the down-regulation of epithelial markers that are commonly used for affinity binding [173, 174].

4.1.4 Inertial microfluidics in straight channels

Inertial lift forces inherent to cell motion in microchannel flows can be exploited to precisely manipulate the cell position within these flows. Due to the small Reynolds number (as a result of small channel dimensions and low flow rates), microfluidics is commonly associated with dominant viscous drag forces which are responsible for the laminar flow properties and help entrain particles along the streamlines. However, when particle/cell size is comparable to channel dimensions, inertial lift forces become significant which can lead to the lateral migration of particles across flow streamlines. Although the first experimental study on particle inertial migration was demonstrated in the 1960s by Segre and Silberberg [175], it was until very recently that such phenomenon has been employed for microfluidic based cell separation [176]. A recent review highlights the applications of this technique towards high-throughput cell separations [177].

In principle, lateral migration of particles in straight microchannel (plane Poiseuille flow) occurs when $a_p/D_h \geq 0.07$ (where a_p is particle diameter and D_h is the microchannel hydraulic

diameter) and the particle Reynolds number is > 0.05 [176]. This is due to the superposition of two inertial lift forces; the shear-induced lift force which arises due to the channel parabolic flow profile and pushes the particles towards the wall, and the wall-induced lift force which pushes the particles away from the wall due to the formation of an asymmetrical wake of the particles when near the wall (Figure 4.3) [176, 178-180]. The net inertial force (F_L) focus the particles at equilibrium positions that are the balance between these two opposing lift forces and is given by [178]

$$F_L = \rho G^2 C_L a_p^4 \quad (N) \qquad (4)$$

where ρ is the density of fluid medium, G is the shear rate of the fluid given (s^{-1}) by $G = U_{max}/D_h$, U_{max} is the maximum fluid velocity and C_L is the lift coefficient (assumed value of 0.5) which is a function of the particle position across the channel cross-section and Reynolds number (*Re*).

From equation (4), it can be observed that the inertial force has a strong dependence on particle size (a_p) and channel shear rate (G). As shear rate and shear distribution vary in channel with different geometries, carefully-designed channels can result in particle focusing at distinct equilibrium positions which can be exploited for efficient particle separation applications (Figure 4.4).

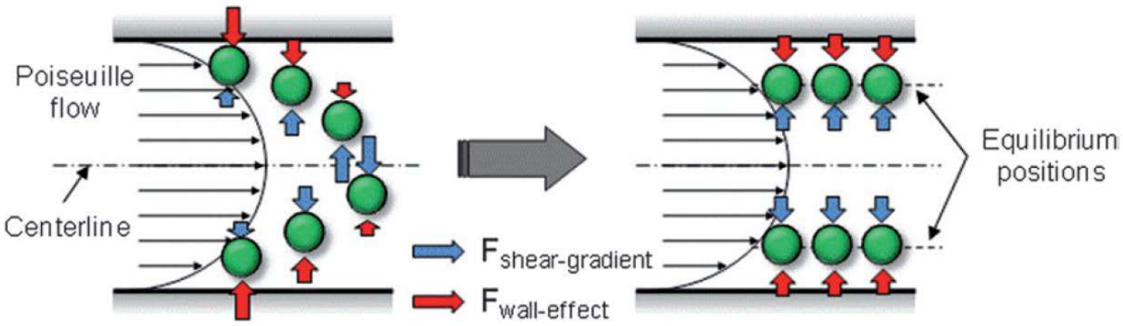

Figure 4.3. Inertial lift forces exerted on cells suspended in a Poiseuille flow. The combined effect of the shear-induced lift force (blue) and the wall-induced lift force (red) align particles/cells at distinct equilibrium positions [180].

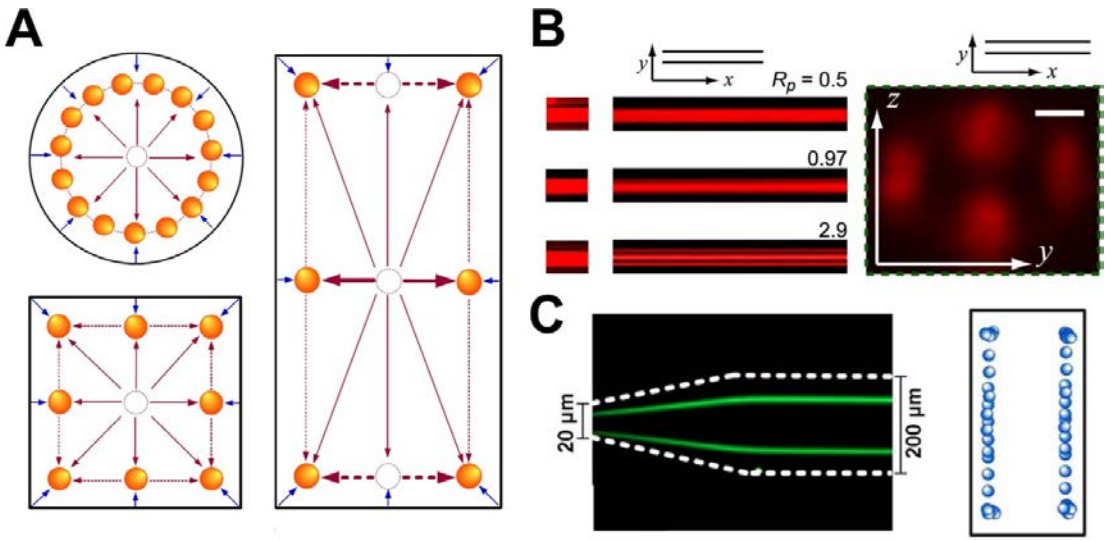

Figure 4.4. Examples of particle inertial focusing in straight channel of different geometries. (**A**) Inertial migration of particles in circular, square, and rectangular microchannels for $a_p/D_h \geq 0.07$ [181]. Particles align to their equilibrium positions where the lift forces balance each other (dotted lines). Arrows indicate the direction of migration for $Re \leq 100$ flows. (**B**) Top-down fluorescent images showing the outlet of 9µm diameter particles in a square channel (50 µm) at different particle Reynolds number (R_p = 0.48, 0.97, or 2.9) [176]. A confocal cross-section shows focusing of particles to the four channel faces. This appears as three lines with double the intensity in the middle streak–line under the microscope. (**C**) Fluorescent and schematic images showing the particle distribution of 2 µm diameter particles in a high aspect ratio microchannel (20 µm by 50 µm) [179]. Bright white lines indicate the approximate position of channel walls.

Throughput for cell separation using inertial microfluidics (~10^6cells/min) is significantly higher than other microfluidic cell separation techniques. As it relies entirely on the intrinsic hydrodynamic forces, channel design is very simple and can be easily integrated with existing microfluidic modules. Also, the channel dimensions are comparably larger than the sample cell sizes, leading to both high volume throughputs and eliminating channel clogging issues. Limitations however include the use of dilute samples as cell-cell interactions can deteriorate the efficiency of this separation technique.

4.1.5 Motivation

Because CTCs are extremely rare in blood, continuous isolation and retrieval of CTCs from blood is a huge technical challenge because it is difficult to eliminate the majority of blood components without losing any CTCs. Current inertial microfluidics based devices are useful for size-based particle separation, but not suitable for blood-related applications due to the high amount of RBCs background (~45% v/v). In this work, we investigated the use of inertial microfluidics for blood cell separation using high aspect ratio rectangular channels, and demonstrated isolation of cancer cells (circulating tumor cells (CTCs)) from blood by exploiting the difference in size between CTCs and hematologic cells (CTCs ~15-20 μm; RBC ~8 μm discoid; WBC ~7-10 μm) [166, 181]. Besides high throughput and high separation efficiency, another key consideration is the collection of viable CTCs as studies of intact CTCs will enable us to gain valuable insights into the complex process of cancer metastasis.

4.2 Design principle

In square microchannels, eight stable equilibrium positions exist due to uniform shear gradient on all four sides at low *Re* (*Re* < 100) [179, 182, 183]. Increasing *Re* to 500 reduces the equilibrium positions to the four corners of the square microchannel [182]. Recent reports have demonstrated that in high aspect ratio rectangular microchannels, the shear rate modulation results in preferential focusing along the longer microchannel dimension (height in this case) [179, 183]. As inertial lift force scales as $F_L \propto G^2$, high aspect ratio (AR, ratio of channel height to width) rectangular microchannel cross-sections yields a higher shear rate (hence stronger F_L) along the shorter channel width ($\sim AR^2$), resulting in particle focusing into two streams near the channel sidewalls along the microchannel height and creating a particle-free central region. In this work, we take advantage of this phenomenon to focus all the peripheral blood cells along the channel walls for downstream removal.

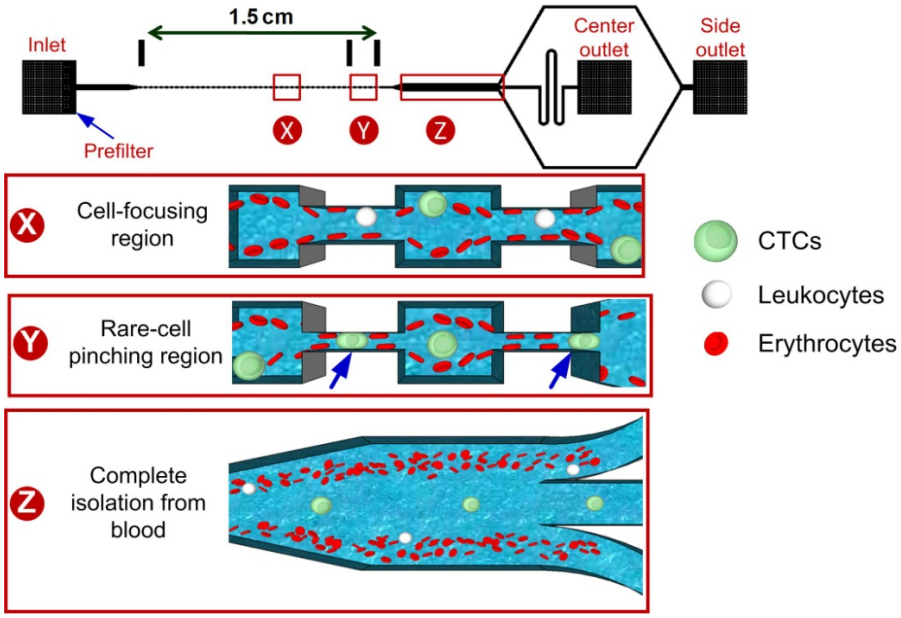

Figure 4.5. Schematic illustration of the developed microfluidic device for rare-cell isolation from blood. The microchannel design consists of high aspect ratio rectangular microchannel patterned with a contraction-expansion array. In the cell-focusing region (X), under the influence of shear modulated inertial lift forces, all the cells equilibrate efficiently along the channel side walls. Flowing through the rare-cell pinching region (Y), the center of mass of the larger CTCs aligns along the channel center while smaller hematologic cells remain focused along the channel sidewall. Designing bifurcating outlets (Z) allows for the collection of the larger CTCs at the center outlet while the remaining hematologic cells are removed from the side outlet as waste.

The developed design consists of a single inlet, high aspect ratio rectangular microchannel patterned with a contraction-expansion array (Figure 4.5). The widths of the contraction and expansion regions were fixed at 20 µm and 60 µm respectively and their lengths were fixed at 100 µm. The outlet opens into a 300 µm wide section and is equally divided into three 100 µm wide bifurcating arms; two side outlets and a central outlet arm. The microchannel consists of 75 subunits of contraction-expansion regions with a total length of 1.5 cm (a pair of contraction and expansion region makes up one subunit) and can be divided into two regions: (i) cell focusing region and (ii) rare-cell pinching region. In the cell focusing region (first 70 subunits), under the influence of shear-modulated inertial lift forces, all the cells migrate and equilibrate along the longer channel sidewalls. At the rare-cell pinching region (last 5 contraction-expansion subunits) prior to the channel outlet, the contraction width in this pinching region (pinching width) is designed to be comparable to the CTCs diameter, such that the center of inertia of these larger cells aligns along the axial centre of the

microchannel. Thus upon exit, all the RBCs and leukocytes still remain focused along the channel sidewalls, while the larger CTCs are "pinched" to the channel axial center, allowing the centre outlet to collect all the CTCS while hematologic cells are removed from the side outlets (Figure 4.5).

In high aspect ratio devices, the width of the microchannel is the critical dimension regulating cell focusing. In this work, this dimension corresponds to the width of the contraction region and was fixed at 20 µm. Ideally, just a straight microchannel (without a contraction-expansion array) is sufficient for efficient cell equilibration [179, 183]. However, recent studies have shown that patterning contraction-expansion regions along the microchannel length enhances particle focusing along the microchannel sidewalls [180, 184]. As the particles/cells travel from the contraction region into the expansion channels, due to increased distance from the channel sidewalls, the shear-induced lift forces dominate and quickly push the particles towards the channel sides. Therefore, the combined effects of shear modulation using high aspect ratio microchannels with the contraction-expansion array enhances cell focusing along the channel sidewalls in a shorter channel length, thereby allowing high throughput cell separations. Secondly, as channel aspect ratio as high as 7.5 are fabricated in PDMS polymer, the expansion regions provides greater structural stability for the microchannels and help to minimize deformation and distortion during fabrication [185, 186].

4.3 Experimental procedures

Cell culture and sample preparation

Two commercially available human breast adenocarcinoma cell lines, MCF-7 and MDA-MB-231, were used to mimic CTC separation in this work. The MCF-7 cells (HTB-22^{TM}, ATCC, USA) and MDA-MB-231 cells (HTB-26 ^{TM}, ATCC, USA) were cultured in low-glucose Dulbecco's modified Eagle's medium (DMEM) (Invitrogen, USA) supplemented with 10%

fetal bovine serum (FBS) (Invitrogen, USA) together with 1% penicillin-streptomycin (Invitrogen, USA). The culture was maintained at 37^{o}C in a humidified atmosphere containing 5% (v/v) CO_2. The cells were cultured in sterile 25 cm^2 flasks (Corning) and sub-cultivated three times a week with media replaced every 48 hours. Sub-confluent monolayers were dissociated using 0.01% trypsin and 5.3 mM EDTA solution (Lonza, Switzerland).

For the control and recovery experiments, the cancer cells were diluted in buffer containing 1× phosphate buffered saline (PBS), 2 mM ethylenediaminetetraacetic acid (EDTA) supplemented with 0.5% bovine serum albumin (BSA) (Miltenyi Biotec, Germany) to prevent non-specific adsorption to the tubing and microchannel walls. The buffer density was increased by supplementing with 3% w/v Dextran 40 (AppliChem Asia, Singapore) to prevent cell sedimentation [91]. For RBC equilibration experiments, whole blood obtained from healthy donors was spun down to separate the RBCs. Final sample concentration was adjusted to varying hematocrit (0.5% - 5%) with sample buffer accordingly. For leukocyte control experiments, whole blood was treated with RBC lysis buffer (eBioscience, USA) according to the manufacturer's instructions to obtain a pure population of leukocytes.

Microchannel fabrication

The devices were fabricated in polydimethylsiloxane (PDMS) using standard microfabrication soft-lithographic techniques described in Chapter 2. In this work however, PDMS prepolymer was mixed in 5:1 (*w*/*w*) ratio with curing agent instead as higher ratio of curing agent promote increased cross-linking, thus making the PDMS channels more rigid for high aspect ratio structures which are easily prone to deformation during fabrication.

Device characterization

During testing, the sample was pumped through the microfluidics devices at varying Reynolds number (*Re*) using a syringe pump (NE-1000, New Era Pump Systems Inc., USA). The microchannels were mounted on an inverted phase contrast microscope (Olympus IX71)

equipped with a high speed CCD camera (FASTCAM 1024 PCI, Photron, USA). High speed videos captured at the channel outlet were then analyzed using ImageJ® software.

Immunofluorescence staining and FACS analysis

Results from experiments conducted to determine the collection efficiency, recovery and enrichment ratio were analyzed by performing flow cytometry analysis using BD™ LSR II flow cytometer (BD Biosciences, USA) on the centre and side outlet samples. Immunofluorescence staining allowed differentiating the various cell types for visualization and quantification. The outlet samples were incubated with FcR blocking reagent (1:100, Miltenyi Biotec Asia Pacific, Singapore) for 15 min to block out non-specific bindings, followed by incubation with allophycocyanin (APC) conjugated Epithelial Cell Adhesion Molecule (EpCAM) (1:100, Miltenyi Biotec Asia Pacific, Singapore) for 40 min to identify the cancer cells. The peripheral blood leukocytes were identified by staining with fluorescein isothiocyanate (FITC) conjugated CD45 marker (1:100, Miltenyi Biotec Asia Pacific, Singapore) for 40 min. During FACS analysis, the cells were gated based on the forward and side scatters as well as the fluorescence intensity. Additionally, due to the extremely high RBC count, the RBC concentration was further confirmed using hemocytometer.

4.4 Results and discussion

As RBCs make up >99% of all hematologic cells, complete removal of RBCs is pivotal for achieving meaningful enrichment. The microchannel design and testing conditions were first optimized by studying the effect of various parameters including microchannel aspect ratio, flow rate and sample hematocrit on RBC focusing and removal from the side outlets.

4.4.1 Aspect ratio study

Figure 4.6 presents the effect of microchannel aspect ratio on RBC focusing. To study the effect of aspect ratio, microchannels of height 20 µm, 50 µm, 75 µm, 100 µm and 150 µm

were fabricated yielding aspect ratios of 1, 2.5, 3.75, 5 and 7.5 respectively. Composite images and linescans indicating the RBC distribution across the channel as a function of aspect ratio are presented in Figure 4.6.

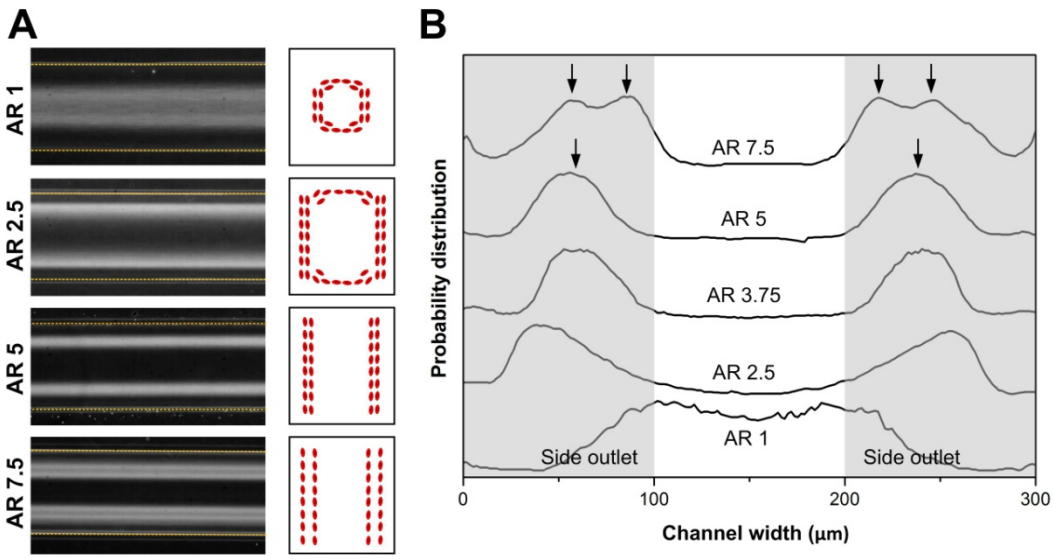

Figure 4.6. Effect of microchannel aspect ratio (AR) on RBCs focusing. (**A**) Averaged composite images at the expanded channel end illustrating RBC equilibration for increasing aspect ratios. The input blood sample was fixed at 1% hematocrit pumped at *Re* = 100. Adjacent schematics indicate the approximate position of the RBCs within the microchannel cross-section at the outlet. (dotted lines indicate approximate position of channel walls) (**B**) Linescans representing the probability distribution of RBCs across the microchannel width measured at the outlet. The position of the side outlets is also indicated on the plot.

In square microchannels (AR 1) at *Re* =100 and 1% hematocrit, the uniform fluidic shear across the cross-section results in RBCs equilibrating in an annular fashion and forming a weakly focused cellular ring across the channel cross-section (as depicted in the schematic). Increasing the aspect ratio to 2.5 initiates the preferential migration of cells across the channel width and equilibration along the microchannel height. However, the linescans clearly indicate that not all RBCs have focused in the equilibrium positions in the given channel length. In microchannels with aspect ratio 3.75, all RBCs equilibrate at the microchannel height, clearly evident by the formation of a prominent cell-free region along the microchannel center. Further increasing the aspect ratio to 5 causes the migration of the two strongly focused cellular band closer towards the channel sidewalls. An interesting effect is seen when we increase the microchannel aspect ratio to 7.5. In this very high aspect ratio

channel, the breaking-up of the focused RBC bands into two, an inner and outer band is observed. This observation is in accordance with very recent experimental and modeling work studying the effect of aspect ratio on inertial migration [187]. The exact mechanisms responsible for this behavior are still unclear and warrant further investigation. However, this effect is unfavorable for separation applications and thus we limit this work to channels with maximum aspect ratio of 5.

4.4.2 Flow rate/ Reynolds number (*Re*) study

Figure 4.7 presents the effect of *Re* on RBC focusing. Tests were conducted using 1% hematocrit sample in AR 5 (h= 100 μm) microchannel and RBC equilibration was studied for *Re* ranging from 10 to 150. Higher flow rates could not be tested due to the high pressure drops across the microchannels resulting in device failure due to channel debonding. At low flow rates ($Re \leq 25$), the inertial lift forces acting on the RBCs are weaker than the viscous drag force, thus no equilibration is observed. Increasing the flow rate to $Re = 50$ and above enables the RBCs to overcome the drag forces and migrate preferentially towards the channels side walls, forming two well-defined cellular-bands (observed as two distinct peaks when imaged from the top or the bottom). We also observed the migration of the RBCs equilibrium positions closer to the microchannel walls with increasing *Re* [182].

To quantify the degree of focusing as a function of *Re*, we define two parameters: cell-free region width and the cell-band width (Figure 4.7B). The cell-free region width is the normalized microchannel width at the microchannel center which is completely devoid of any RBCs. It is calculated from the RBCs probability distribution profile by measuring the full width at half maximum (FWHM) of the distance between the two cell-occupied regions. Similarly, the cell-band width is calculated by measuring the FWHM of the region occupied by the RBCs. As *Re* increases, the large inertial lift forces induce stronger RBC focusing; evident with a decrease in the cell-band width (Figure 4.7C). Consequently, the width of the cell-free region increases with increasing flow rate. At low *Re* (<100), the reduction in the

cell-band width, as a result of tighter RBC focusing, accounts for the increase in the cell-free region at the microchannel center. Beyond *Re* = 100, although the width of the cell-band remains constant, the increase in the cell-free region is accounted by the migration of the two RBC-bands closer to the channel sidewalls. For optimal RBC focusing and collection at the side outlets, it is essential to operate in the strongly focused region ($Re \geq 100$).

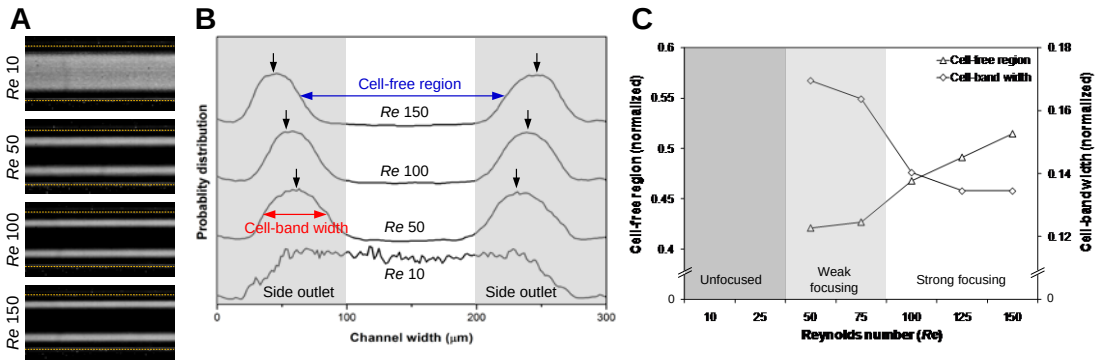

Figure 4.7. Effect of flow rate (*Re*) on RBCs focusing. (**A**) Averaged composite images illustrating RBC equilibration for increasing flow rate. The input blood sample was fixed at 1% hematocrit and pumped through AR 5 microchannel. (dotted lines indicate approximate position of channel walls) (**B**) Linescans representing the probability distribution of RBCs across the microchannel width at the outlet. (**C**) Experimental result indicating the width of the cell-free region at the channel center and the thickness of the cell-band for increasing *Re*.

4.4.3 Hematocrit study

Tests were also performed to determine the highest sample hematocrit that can be processed in these microchannels without affecting the RBC focusing. For applications involving whole blood processing (~40% hematocrit), it is imperative to work with high hematocrit to reduce processing and analysis time. The cell-free region and the cell-band width parameters were used to determine the optimal test conditions. Experiments were conducted with hematocrit ranging from 0.5% to 5% at *Re* = 100 in AR=5 microchannel. Composite images and linescans presenting the effect of increasing hematocrit on RBC equilibration are shown in Figure 4.8. As the input hematocrit is increased, the width of the RBC band increases in a linear fashion, consequently decreasing the width of the central cell-free region. This trend is expected for increasing volume fraction (hematocrit) as more RBCs try to occupy the equilibration positions, resulting in significant cell-cell interaction induced dispersion.

An interesting effect was observed when the hematocrit was increased to 3% and above. As seen earlier in microchannels with aspect ratio 7.5, we again observe the breaking up of the cell-band into two prominent inner and outer bands. Again, the formation of these inner and outer bands is unfavorable for separation applications as it reduces the width of the central cell-free region. For this reason, this work is limited to samples with maximum hematocrit of 2%, implying a 20× whole blood dilution prior to testing.

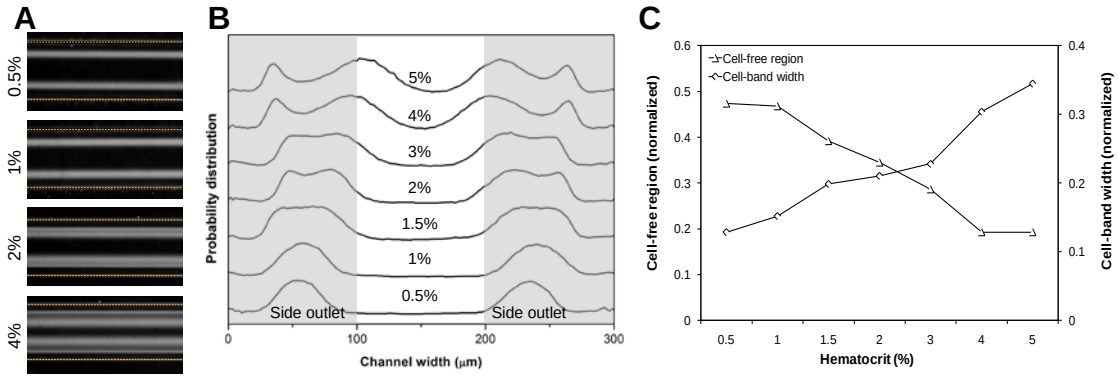

Figure 4.8. Effect of hematocrit on red blood cell focusing. (**A**) Averaged composite images illustrating RBC equilibration for increasing hematocrit. The input blood sample was pumped at *Re* = 100 through AR 5 microchannel. (dotted lines indicate approximate position of channel walls) (**B**) Linescans representing the probability distribution of RBCs across the microchannel width measured at the outlet. (**C**) Experimental result indicating the width of the cell-free region at the channel center and the thickness of the cell-band for increasing hematocrit.

4.4.4 CTCs pinching width characterization

As mentioned in the design principle section, the 'pinching' width is a key feature of the microfluidic device for the successful isolation of CTCs from other hematologic cells. The contraction width along this pinching region is designed to be comparable (smaller) to the CTCs diameter, ensuring that the cells are effectively 'squeezed' to the centre as they traverse through the contraction channels (Figure 4.9). Two human breast adenocarcinoma cell lines, MCF-7 and MDA-MB-231, with average measured diameters of 18.1 ± 1.8 μm and 18.2 ± 2.8 μm respectively were tested. As the average size of the CTCs is larger than 15 μm [69, 166], we designed microchannels with 10 μm, 12 μm and 15 μm pinching widths to ensure minimum loss of CTCs at the side outlets. Figure 4.10 presents the effect of pinching width

on MCF-7 cells separation for increasing channel *Re*. At low *Re* = 50, ~95% of tumor cells are collected at the centre outlet for all three contraction widths. Increasing the *Re* results in a decrease in the collection efficiency, possibly due to the large deformability of cancer cells under high laminar shear stresses and deformation of the PDMS channel [188, 189]. Considering alternate materials such as hard plastics (PMMA, COC) may overcome this issue thereby increasing the collection efficiency. As CTCs are extremely rare cells, a collection efficiency cut-off of 90% was targeted in this work. Results from experiments conducted with only RBCs suggest *Re* = 100 flows optimal for their removal from the side outlets. Based on these results, the 10 µm channel width was selected for efficient CTC collection. Similar results were observed for the MDA-MB-231 cells.

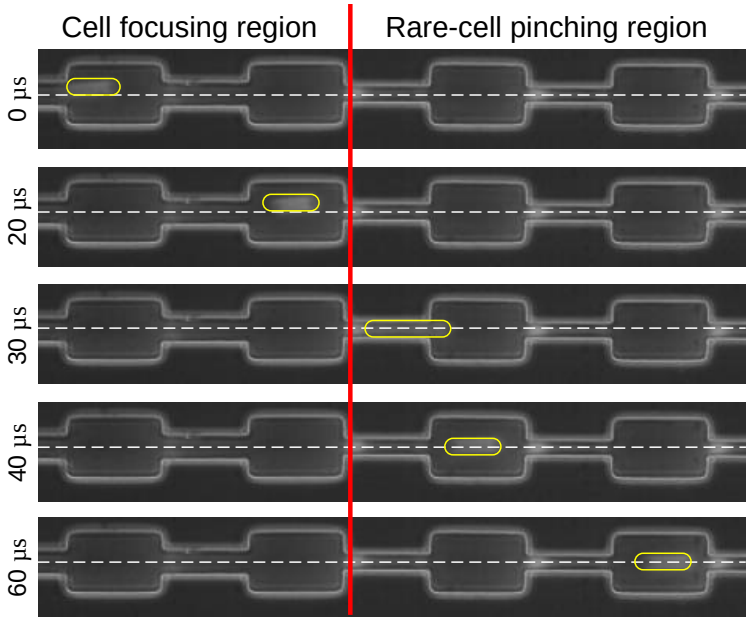

Figure 4.9. Time-sequential images indicating the rare-cell isolation principle of the developed microfluidic device. In the cell-focusing region the CTCs (MCF-7 cells marked by yellow circles) under the influence of shear-modulated inertial forces equilibrate along the microchannel sidewalls. (white dotted line indicates the approximate channel center) Passing through the pinched section (10 µm width), the center of inertia of CTCs align with the center of the microchannel width. In the expansion region the CTCs continue to follow the flow streamlines and stay aligned along the center of the microchannel width.

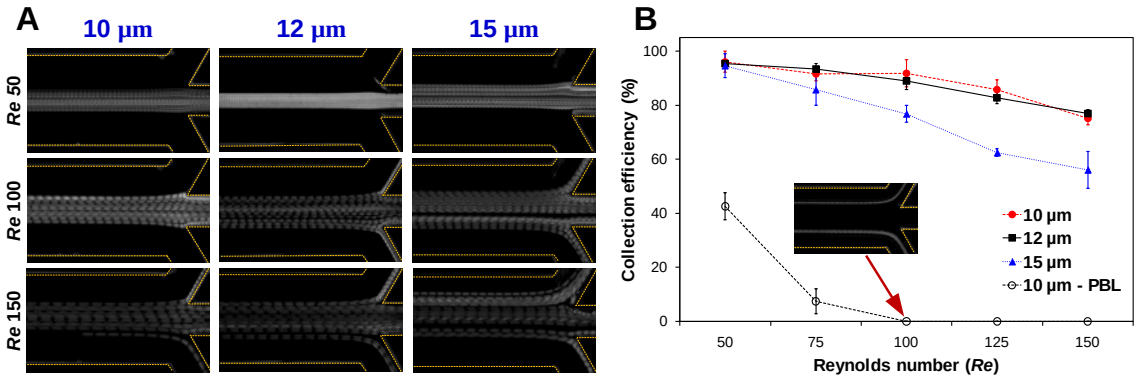

Figure 4.10. Effect of channel width in the cell-pinching region on CTC separation efficiency. (**A**) Averaged composite images illustrating MCF-7 cells isolation in the center outlet for increasing flow rate in microchannels with varying "pinching" widths. (dotted lines indicate approximate position of channel walls) (**B**) Plot indicating the fraction of MCF-7 cells and peripheral blood leukocytes collected at the center outlet for increasing *Re*.

Following separation, the cell viability was tested by reseeding the MCF-7 cells back into culture using the procedure described in the methods section to observe their proliferation and growth. After 4 days of culture, the proliferation rate of the isolated MCF-7 cells was similar to the control cells with no noticeable change in the morphology (Figure 4.11). The cell viability was further quantified using trypan blue dye exclusion assay with >90% cells excluding the dye post sorting. These results confirm that the developed technique has minimal effect on the cells during isolation maintaining high post-sorting cell viability.

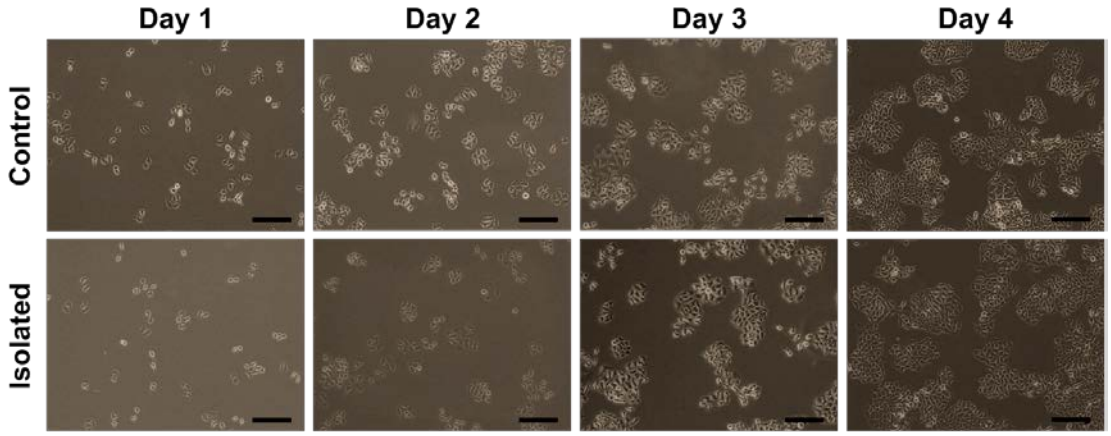

Figure 4.11. Phase contrast images of cultures of control (unsorted) MCF-7 cells and cells isolated from the center outlet of the microfluidic device. The images indicate no significant differences between the morphology and proliferation rate of the MCF-7 cells suggesting high viability. Scale bar is 200 µm.

For subsequent downstream CTC analysis, it is important to minimize contamination due to the presence of peripheral blood leukocytes in the isolated samples. To assess the device efficiency for PBL removal, a pure population of human leukocytes isolated by RBC lysis was ran through the microchannel (pinching width = 10 μm) at varying *Re*. As the mean diameter of human leukocytes is smaller than 10 μm in diameter [4, 71, 190], the flow path of the leukocytes in cell pinching region remain unchanged and are thus filtered out from the side outlets (Figure 4.10B). As evident from the figure, at *Re* 50 and 75 a fraction of leukocytes are still collected at the center outlet due to weak inertial cell focusing. However at $Re \geq 100$, all the leukocytes equilibrate along the channel sidewalls with no cells collected at the center outlet.

4.4.5 Whole blood analysis

Following the characterization of device dimensions and operating conditions, MCF-7 cells spiked into whole blood were analyzed in the device using the optimal parameters (~1.5-2% hematocrit, AR = 5, *Re* =100). The width of the cell pinching region was fixed at 10 μm. Outlet samples labeled with fluorescent markers were analyzed using FACS and hemocytometer to calculate the separation enrichment. The results indicate ~300× enrichment over RBC and ~850× enrichment over leukocytes with ~85% CTC recovery in a single pass through the device (1^{st} stage) (**Table 5**). To achieve higher and meaningful enrichments for CTC detection, samples collected from the center outlet of the device are processed again through the device to completely eliminate the contaminating hematologic cells (2^{nd} stage) (Figure 4.12). This was implemented by connecting the outlet tubing from the 1^{st} stage to another device in a cascaded configuration. By adding a 2^{nd} stage, the MCF-7 enrichment increases significantly to 3.25×10^5 (5.5 $\log_{10}$) fold over RBCs and ~1.2×10^4 (4.1 $\log_{10}$) over leukocytes, with minimal loss in overall CTC recovery (~81%). This converts to approximately 15,000 RBCs and less than 850 leukocytes per mL of blood (assuming 5

billion RBCs and 10 million leukocytes in one mL of whole blood). This enrichment performance of the device is comparable to other popular size-based and immuno-mediated (including immunomagnetic, immunofluorescent and immunobinding) CTC sorting techniques typically achieving 10^4-10^6 fold enrichment [69, 70, 83, 166, 167, 181, 191].

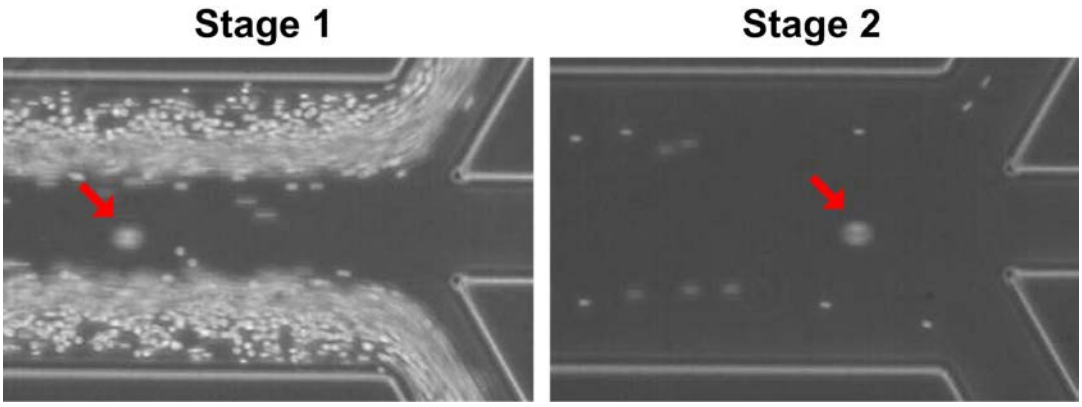

Figure 4.12. High speed images illustrating distinct difference in equilibrium positions between MCF-7 cells (red arrows) and blood cells at the channel end which allows their subsequent separation into the centre and side outlets respectively. By cascading two devices, higher enrichment factor / purity is obtained at the centre outlet of 2nd stage separation.

Table 5 Separation performance of whole blood spiked with MCF-7 cells.

	Concentrations (%)		
	RBCs	**Leukocytes**	**MCF-7**
Sample	100	100	100
1st stage	0.304 ± 0.003	0.115 ± 0.013	84.51 ± 2.85
2nd stage	3.10E-04 ± 3.76E-05	0.008 ± 0.007	81.10 ± 4.13

4.5 Summary

In this chapter, we presented a high throughput inertial-based separation technique to isolate CTCs from blood using high aspect ratio microchannel patterned with a contraction-expansion array. While many published CTC isolation techniques work with undiluted whole blood, our device performance is limited to dilute samples for efficient cell separation.

Despite a 20× sample dilution, the microfluidic device is capable of achieving comparable throughput due to the high flow rates required for inertial focusing. By testing a 2% hematocrit sample at a high flow rate of 400 µl/min (*Re* 100), the device is capable of processing ~10^8 cells/min using a single device, which translates to ~50 min of processing time for 1 mL whole blood. Designing just four parallel channels, the analysis time can be practically reduced to less than 15 min/mL of blood, faster than other popular CTC detection techniques.

Secondly, the residence time of cells in the microchannels is <10 ms, significantly lower than other physical entrapment methods with typical operational time >1 hr. Such long-term exposure of cells to high shear can potentially alter their phenotype affecting downstream molecular analysis [192]. As the device offers continuous sorting and collection capability, isolated CTCs can be retrieved easily for downstream assays such as gene analysis, drug screening and molecular-targeted cancer therapy. The isolated cells can also be enumerated and analyzed in real-time rather than performing an end-point investigation.

As with any size-based CTC separation technique, a major limitation of this device is its inability to isolate tumor cells that overlap the leukocyte size scale. Furthermore, there is possibility of capturing unknown cells circulating in blood that are larger or on the order of CTCs [193]. Although most epithelial tumor cells are larger than leukocytes, tests with clinical samples have shown that captured CTCs exhibit significant size heterogeneity [194]. As other size-based CTC isolation techniques have shown promising results when translated to clinical diagnosis [195], further validation of the developed microdevice using clinical patient samples will be necessary to evaluate its potential as a cancer diagnosis technique.

5 Circulating tumour cells (CTCs) isolation using Dean Flow Fractionation (*DFF*)

In this chapter, we report an ultra-high throughput separation technique for CTCs isolation from blood using the inherent Dean vortex flows present in curvilinear channels, aptly termed *Dean Flow Fractionation (DFF)*. The large channel dimensions enable processing of very high hematocrit blood samples (~20%) which allow us to process 1 mL of whole blood in under 20 minutes with >90% cancer cell recovery. This, to our knowledge, is the fastest processing speed demonstrated in microfluidics systems for continuous CTCs isolation.

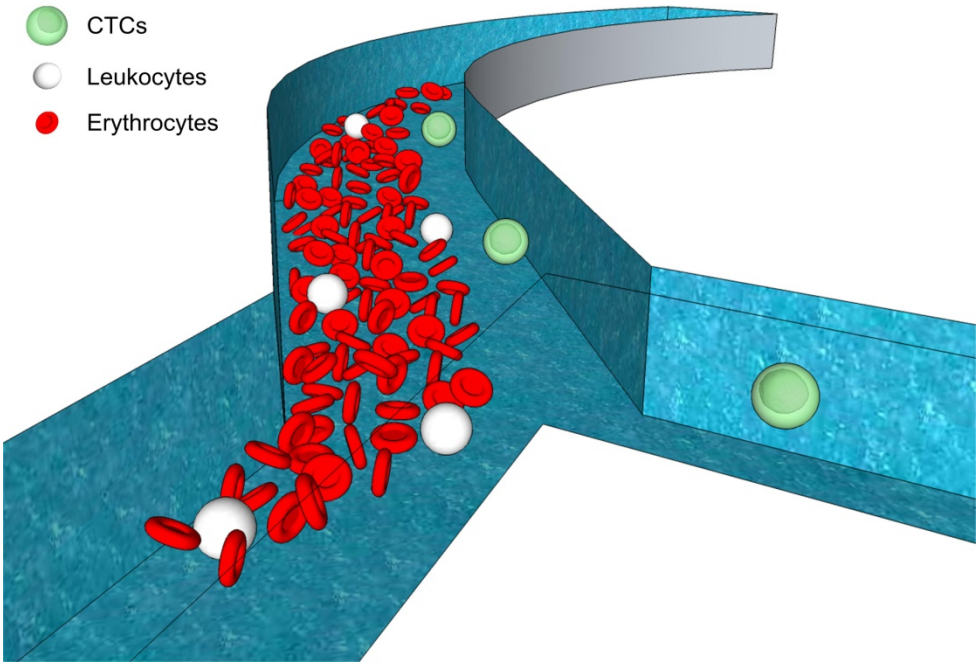

5.1 Background

5.1.1 Dean flow in curvilinear channels

In curvilinear channels, due to non-uniform fluid inertia across the channel in Poiseuille flow, fluid elements at the channel centre have higher velocity and inertia and will flow outwards at the channel midline in the radial direction under the influence of centrifugal acceleration [177]. This creates a centrifugal pressure gradient in the radial direction and by conservation of mass; fluid elements near the outer wall will recirculate inwards, thereby creating two symmetrical counter-rotating vortices (top and bottom) across the channel (Figure 5.1A). The shape and magnitude of the Dean vortices is determined by the Dean number *(De*) and is given by [196, 197]

$$De = \frac{\rho U_f D_h}{\mu} \sqrt{\frac{D_h}{2R}} = Re \sqrt{\frac{D_h}{2R}} \qquad (5)$$

where ρ is fluid density (kg m^{-3}), μ is fluid viscosity (kg $m^{-1}s^{-1}$), U_f is the average primary channel velocity (m s^{-1}), D_h is the microchannel hydraulic diameter (m) defined as $2w \times h/(w + h)$, R is the radius of curvature (m) and *Re* is Reynolds number that compares the inertial forces to viscous forces. From equation (5), it is observed that *De* increases with higher curvature (smaller R), larger channel size (larger D_h), and faster flow (higher *Re*). An increase in *De* magnitude results in higher Dean flow velocity and shifting of the vortices towards the outer wall [198]. Presence of rotational Dean vortices in curved microchannels has been employed for fluid mixing applications using a simple two-inlet spiral channel design (Figure 5.1B) [199, 200]. Main advantages include simple channel geometry and device fabrication, the ability to mix a wide range of fluids of various physical properties and enhancement of mixing performance with increasing flow rate [177]. Besides mixing, Huang *et al.* have also developed a tunable focal length lens using a 90-degree curve microchannel by accurately controlling the interface between two co-flowing fluids with different refractive indices [201].

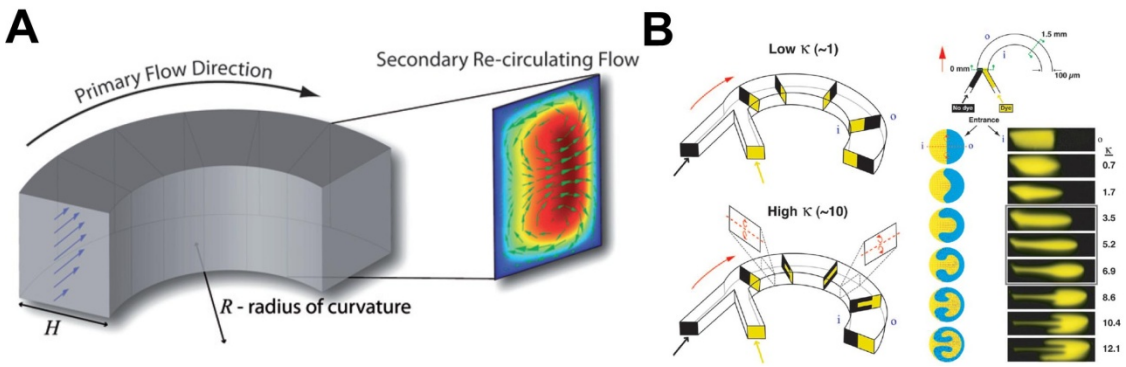

Figure 5.1. (**A**) Secondary Dean flow in curved channels whereby two counter-rotating vortices (green arrows) are created at top and bottom halves of the channel cross section perpendicular to the main flow [177]. (**B**) Fluid mixing in a spiral channel based on Dean flow [199].

5.1.2 Particle focusing in curvilinear channels

Recently, several studies have shown that suspended particles can be entrained into the Dean vortices in curvilinear channels and experience lateral Dean drag force (F_D) which causes them to migrate across streamlines. This has been successfully employed for high-throughput, membrane-free particle/cell separation applications using different curvilinear channel geometries including spiral, single curve and serpentine channels (Figure 5.2) [176, 202, 203]. Ookawara *et al.* formulated the expression for the average Dean velocity (U_{De}) for a given *De* as [197]

$$U_{De} = 1.84 \times 10^{-4}\, De^{1.63} \quad (\mathrm{m\ s^{-1}}) \qquad (6)$$

As shown above, the transverse Dean flow velocity increases with *De* and the expression for the Dean drag force (F_D) is then derived by assuming Stokes drag and is given by [196]

$$F_D = 3\pi\mu\, U_{De}\, a_p = 5.4 \times 10^{-4}\, \pi\, \mu\, De^{1.63}\, a_p \ \ (\mathrm{N}) \qquad (7)$$

where a_p is particle diameter. In low aspect ratio straight rectangular channels (width ≫ height), particles ($a_p/h \geq 0.07$) undergo inertial focusing and equilibrate across the longer channel width (top and bottom of the rectangular channel) due to shear rate modulation along the shorter channel height (discussed in Chapter 4) [179]. The characteristic length here corresponds to the shortest channel dimension (channel height, *h*) instead of D_h. However in

low-aspect-ratio curved microchannels, the interplay between inertial lift forces (F_L) and Dean drag (F_D) reduces the particle focusing positions to two points near the channel inner wall with each equilibrium position situated within one vortex (Figure 5.2) [204]. Additionally, the particles will also alternate in the z-plane (channel height) with uniform longitudinal spacing [204]. It is known that inertial lift forces and Dean drag vary in magnitude across the channel cross section but the exact functional form is still poorly understood. Nevertheless, it has been demonstrated that the particle equilibrium position is strongly dependent on the ratio of the inertial lift and Dean drag forces (F_L/F_D) which varies with the third power of the particle diameter [89, 204, 205].

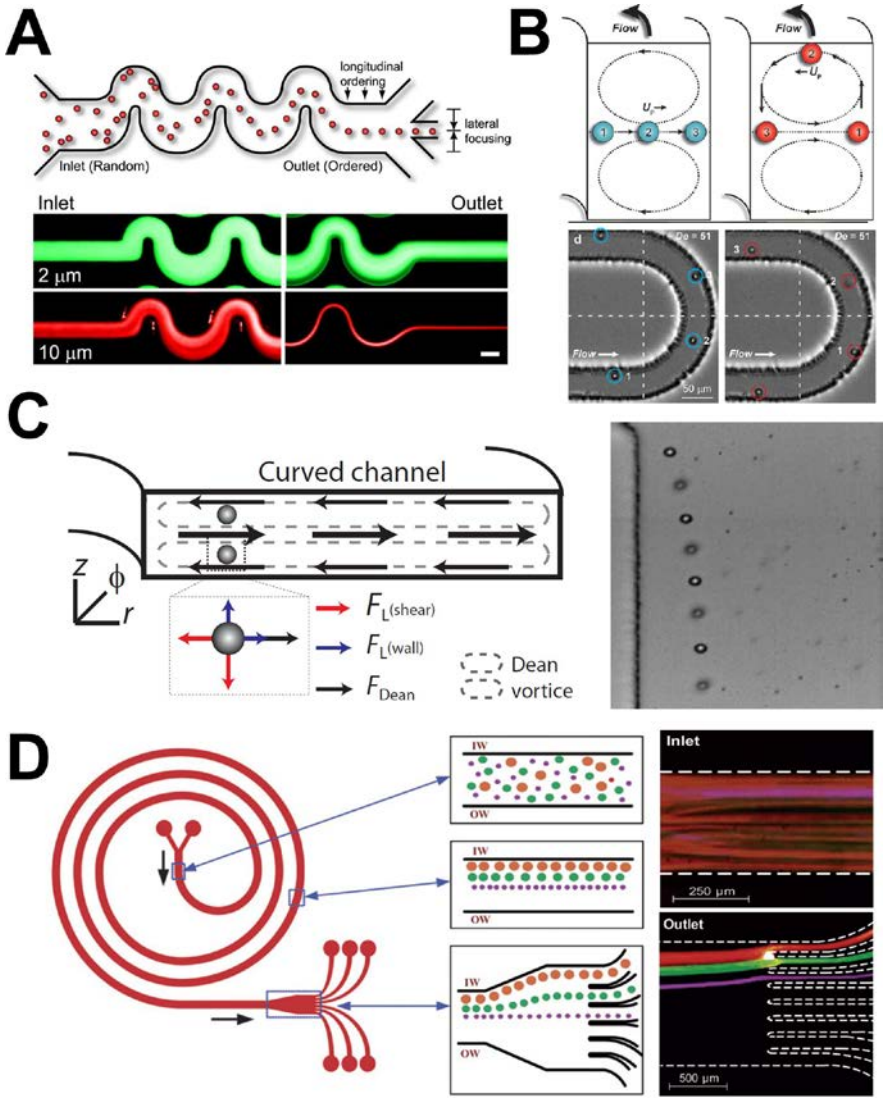

Figure 5.2. Particle focusing in curvilinear channels. (**A**) *top* Schematic illustrating particle inertial focusing in an asymmetric curving serpentine channel [176]. *bottom* Differential

focusing of 10 µm and 2 µm mixed particles. 2 µm particles remain unfocused while 10 µm particles focused sharply into a single stream after transiting 3 cm of asymmetric turns. (Scale bar = 50 µm) (**B**) Schematic and high speed images indicating lateral particle migration at different positions within a Dean vortex in a single U-turn microchannel [203]. (**C**) *(left)* Schematic illustration of particle focusing in a curved channel [204]. Due to superposition of inertial lift forces and Dean drag, particles are focused to two distinct equilibrium positions, with each point within each secondary vortices. *(right)* Snapshot indicating focusing of 10 µm particles in longitudinally alternate positions near the inner wall while 2um particles remained scattered in the channel outlet at *Re* = 88. (**D**) Separation principle and optical images indicating distinct size-based focusing positions of 10 µm (purple), 15 µm (green) and 20 µm (red) particles near the inner wall in a spiral channel which resulted in their efficient separation into different outlets [89].

As compared to straight channels employing only inertial forces for particle focusing, key advantages of using Dean flow for particle focusing in curvilinear channels include the reduction in channel length due to enhanced lateral migration by the secondary Dean vortices which results in particle focusing faster at their equilibrium positions. Throughput is also higher than straight channels as the large channel dimensions and generation of Dean vortices (*De* ~2-20) generally require higher working flow rates for particle focusing. The large channel dimensions also help to minimize clogging issues and allow testing of higher sample concentrations, leading to further improvement in throughput. Moreover, the strong dependence of inertial focusing on particle size ($F_L/F_D \propto a_p^3$) in curvilinear channels can easily enhance particle separation resolution over a wide range of particle sizes [89].

5.1.3 Motivation

Inertial microfluidics in straight and curvilinear channels has been used for efficient particle and cell separation, but a main drawback for blood-related applications is the requirement of relatively diluted blood samples (< 1% hematocrit), thereby lowering overall throughput [107, 206]. This is due to increased RBC-RBC interactions and broadening of the RBC focused band in the channel which leads to poorer separation resolution. In chapter 4, we presented an inertial-based circulating tumor cells (CTCs) separation method using high aspect ratio rectangular channels which allows processing of high hematocrit blood samples (~2%). In this work, we further improve the throughput by introducing another size-based separation

technique for CTCs isolation from blood using the inherent Dean vortex flows present in curvilinear channels, aptly termed *Dean Flow Fractionation (DFF).* The large channel dimensions enable processing of very high hematocrit blood samples (~20%) at an ultra high throughput of 1 mL of whole blood under 20 minutes. This, to our knowledge, is one of the fastest processing speeds in microfluidics systems to date.

5.2 Design Principle

Particles flowing in a curvilinear channel experience a lateral drag force due to the presence of the transverse Dean flows, entraining and driving them along the direction of flow within the vortices. This motion translates to the particles moving back and forth along the channel width between the inner and outer walls with increasing downstream distance when visualized from the top or bottom. The lateral distance traversed by a particle along the Dean vortex can be defined in terms of 'Dean cycle' (DC). For example, a particle which is initially positioned near the microchannel outer wall migrates to the inner wall at a given distance downstream is said to have completed ½ Dean cycle (DC 0.5). Returning back to the original position near the channel outer wall completes a full Dean cycle (DC 1). For a given microchannel length, the particles can thus undergo multiple Dean cycle migration with increasing flow rate (*Re*) conditions. The length for a complete Dean cycle migration (L_{DC}) can be estimated as:

$$L_{DC} \approx 2w + h \tag{8}$$

where w and h is the microchannel width and height respectively. Consequently, the total microchannel length (L_c) required for Dean migration is given by:

$$L_C = \frac{U_f}{U_{De}} \times L_{DC} \tag{9}$$

where U_f is the primary fluid flow velocity (m s^{-1}) and U_{De} is the transverse Dean flow velocity (m s^{-1}). Apart from Dean drag force, larger particles ($a_p/h \geq 0.07$) in curvilinear microchannels also experience appreciable inertial lift forces (both shear and wall-induced) and the superposition of these two forces results in particle focusing at two equilibrium positions near the inner channel wall, each within the top and bottom Dean vortex. These two equilibrium positions overlay each other along the microchannel height and are located at the same distance from the microchannel inner wall for a given particle size, *i.e.* viewed as a single position from top or bottom.

In this work, we take advantage of these two phenomena, *i.e.* Dean migration and inertial focusing, to achieve CTCs separation from blood based on the size difference between CTCs, which are typically ~15-20 µm in diameter, and the other blood cells (RBC ~8 µm; leukocyte ~10-15 µm). The design consists of a 2-inlet, 2-outlet spiral microchannel (500 µm (w) × 160 µm (h)) with a total length of ~10 cm. The sample inlet (75 µm width) and sheath inlet (425 µm width) is fixed at the outer and inner side of the channel respectively. Channel dimensions are selected such that only the larger CTCs undergo inertial focusing, while migration of the smaller hematologic cells (RBCs and leukocytes) is solely affected by the Dean drag (*i.e.* only the CTCs satisfy the $a_p/h \sim 0.1$ ratio). At the outlet bifurcation, the larger CTCs are collected at the CTC outlet (150 µm width) at the inner side while smaller hematologic cells are filtered into the waste outlet (350 µm width) at the outer side.

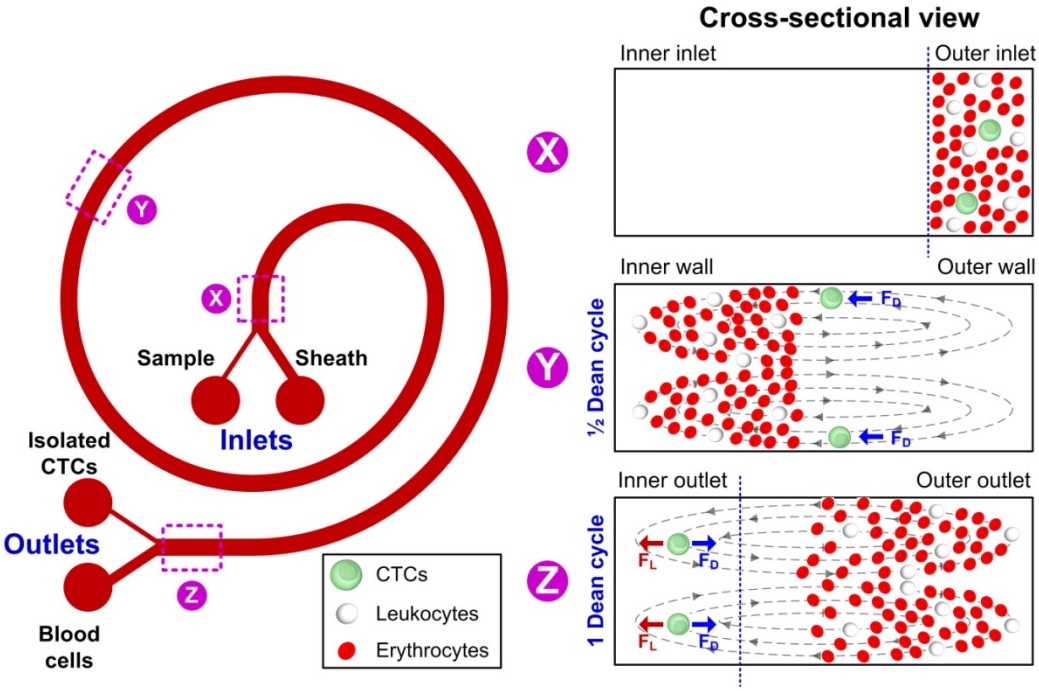

Figure 5.3. Schematic of the developed ultra-high throughput CTC isolation chip illustrating the operating principle at Dean cycle 1 (DC 1). Blood sample is pumped through the outer inlet of the device and sheath fluid is pumped through the inner inlet. Under the influence of Dean drag forces (F_D), the smaller hematologic cells (RBCs and leukocytes) migrate along the Dean vortices towards the inner wall, then back to outer wall again (cross-sectional view), while the larger CTCs experience additional strong inertial lift forces (F_L) and focus along the microchannel inner wall, thus achieving separation.

At the inlet, high hematocrit blood sample is pumped into the outer inlet while sheath fluid (1× PBS) is pumped through the inner inlet at a higher flow rate to form a tight sample stream at the outer wall (Figure 5.3). As the sample transverses through the channel, under the influence of Dean drag forces, all the cells initiate migration along the Dean vortex and move towards the inner channel. Near the inner wall, the strong inertial lift forces experienced by the larger CTCs prevent them from migrating further under the influence of Dean drag and cause them to focus and occupy the two equilibrium positions. On the other hand, since the RBCs and leukocytes are not influenced by inertial forces, these cells continue to circulate along the Dean vortex towards the outer wall. By calculating the appropriate flow rate ensuring that the blood cells undergo a complete Dean cycle migration (DC 1) to outer half of the channel at the channel outlet, the focused CTCs near the channel inner wall can be continuously collected at the inner outlet while blood cells are removed from the outer outlet

as waste (Figure 5.3). The advantage of using this technique is its ability to process very high hematocrit samples (~20%) thus reducing sample preparatory steps and decreasing the processing time significantly.

5.3 Experimental procedures

The devices were fabricated in polydimethylsiloxane (PDMS) using standard microfabrication soft-lithographic techniques described in Chapter 2.

COMSOL modeling

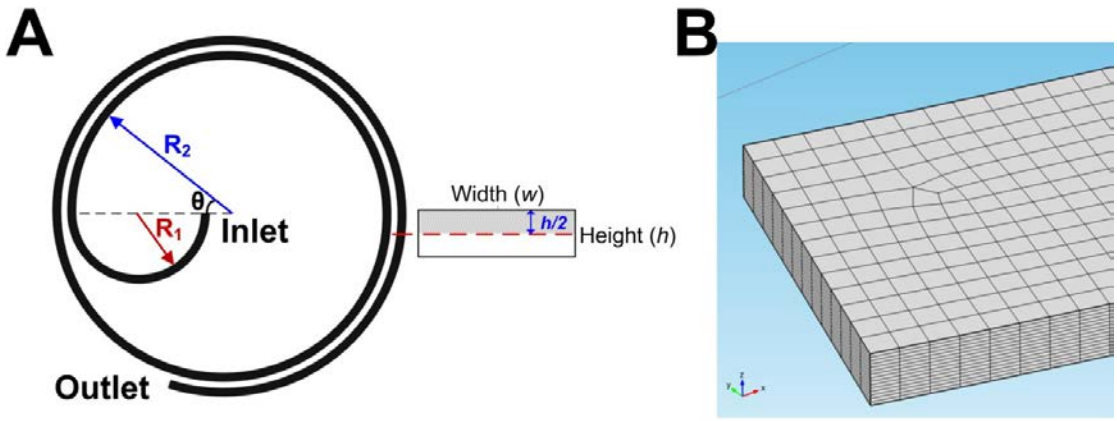

Figure 5.4. 3D computational simulation of fluid flow in the proposed spiral device. (**A**) Schematic diagram of the constructed spiral channel used for modelling. Due to flow symmetry about the middle plane, only the top half of the channel (gray area) was modelled to shorten the computational time. (**B**) Illustration of the meshing network used in the study. A high number of meshing grids were added along the height to more accurately model the Dean flow acting in the transverse direction.

Commercially available COMSOL Multiphysics (COMSOL Inc, Burlington, MA) software was used to study fluid flow behavior inside the proposed spiral design. The model structure consists of an inner semi-circular channel with radius R_1 = 0.42 cm and a spiral channel R_2 = (1.0 + 0.1θ/2π) cm. Width (*w*) and height (*h*) of the channel were fixed at 500 µm and 155 µm respectively. Full Navier-Stokes equations for incompressible fluids were solved using finite element method. For simplicity, it was assumed that the presence of suspended particles does

not affect the intrinsic properties of the fluid (a continuum fluid with density 1g cm^{-3} and dynamic viscosity 0.001 Pa s). Fluid flow with varying flow rates (in mL/min) and no-slip boundary conditions were applied at the channel inlet and channel wall boundaries respectively. At the outlet, the pressure was set to zero with no viscous stress on the boundary. As the flow is symmetric about the middle plane in the z direction (depth), only half of the channel (upper channel) was modeled (Figure 5.4), which introduced an additional symmetric boundary condition for that symmetric plane. From the steady-state solution for single-phase laminar flow, Dean migration of the fluid elements (similar as particles) at the outer wall region were obtained using particle tracking functionality in the software and compared with experimental observations of fluorescence microbeads lateral migration.

For calculation of Dean flow, a separate semi-circular channel with the same dimensions as the spiral channel was modeled under similar fluid flow conditions. The radius of the channel was set as 0.42 cm and 1.0 cm respectively, which corresponds to inner and outer loop of the spiral channel. Maximum Dean and axial flow speed were then calculated at mid point along the circular channel at different flow rates, where the error caused by the boundary effect is expected to be negligible.

Cell culture

Human breast adenocarcinoma cell lines, MCF-7 and MDA-MB-231, and human cervical HeLa cell line were used to mimic CTC separation in this work. The cells were cultured in low-glucose Dulbecco's modified Eagle's medium (DMEM) (Invitrogen, USA) supplemented with 10% fetal bovine serum (FBS) (Invitrogen, USA) together with 1% penicillin-streptomycin (Invitrogen, USA). The culture was maintained at 37^{o}C in a humidified atmosphere containing 5% (v/v) CO_2. The cells were sub-cultivated every 4 days with media replaced every 48 hours. Sub-confluent monolayers were dissociated using 0.01% trypsin and 5.3 mM EDTA solution (Lonza, Switzerland).

Sample preparation

Fluorescently labeled microbeads of 6 and 15 μm diameter (Fluoresbrite® Microspheres, Polysciences Inc, Singapore) were added (0.01% volume fraction) to sample buffer which consists of 1× phosphate buffered saline (PBS), 2 mM ethylenediaminetetraacetic acid (EDTA) supplemented with 0.5% bovine serum albumin (BSA) (Miltenyi Biotec, Germany). BSA was used to prevent non-specific adsorption to the tubing and microchannel walls. For RBC hematocrit experiments, whole blood obtained from healthy donors was spun down to separate the RBCs. Final sample concentration was adjusted to varying hematocrit (1% - 45%) with sample buffer accordingly. For leukocyte control experiments, whole blood was treated with RBC lysis buffer (eBioscience, USA) according to the manufacturer's instructions to obtain a pure population of leukocytes. To study the focusing of cancer cells in spiral channel, a high number of cancer cells (~10^5 cells/ mL) were added into the sample buffer to facilitate high speed imaging and analysis. Whole blood experiments were carried out by diluting fresh blood samples to ~20% hematocrit and spiked with MCF-7 cells (~10^5/ mL). A high number of cancer cells was used as flow cytometry (FACS) analysis generally require recording of >100 000 events for greater accuracy.

Device characterization

During testing, cancer cell and blood sample was filled in a 1 mL syringe and pumped through the spiral microfluidic device using a syringe pump (NE-1000, New Era Pump Systems Inc., USA) while sheath flow (1× PBS, 2 mM EDTA supplemented with 0.5% BSA) was filled in a 60 mL syringe and pumped into the device using a separate syringe pump (PHD 2000, Harvard Apparatus, USA). The flow rate ratio between the sample and sheath flow was fixed at 1: 9 to form a tight sample stream at the outer wall. The devices were mounted on an inverted phase contrast microscope (Olympus IX71) equipped with a high speed CCD camera (Phantom v9, Vision Research Inc., USA). High speed videos were captured at the channel outlet using Phantom Camera Control software and then analyzed using ImageJ® software. For fluorescence imaging, another inverted microscope (Olympus

IX81, Olympus Inc., USA) equipped with a 12-bit EMCCD camera (iXon^{EM}+ 885, Andor Technology, USA) was used. Images were acquired using Metamorph® software (Molecular Devices, USA) and analyzed using ImageJ® software.

Immunofluorescence staining and FACS analysis

To determine the enrichment ratio between the sample and sorted CTCs, flow cytometry (FACS) analysis using BD™ LSR II flow cytometer (BD Biosciences, USA) was performed on the inlet and CTC outlet samples. Immunofluorescence staining allowed differentiating the various cell types for visualization and quantification. After sorting, the cells were stained with allophycocyanin (APC) conjugated Epithelial Cell Adhesion Molecule (EpCAM) (1:100, Miltenyi Biotec Asia Pacific, Singapore) and fluorescein isothiocyanate (FITC) conjugated CD45 marker (1:100, Miltenyi Biotec Asia Pacific, Singapore) for 30 minutes to identify MCF-7 cells and blood leukocytes respectively. Additionally, due to the extremely high RBC count, the RBC concentration was further confirmed using hemocytometer.

5.4 Results and discussion

5.4.1 COMSOL simulation

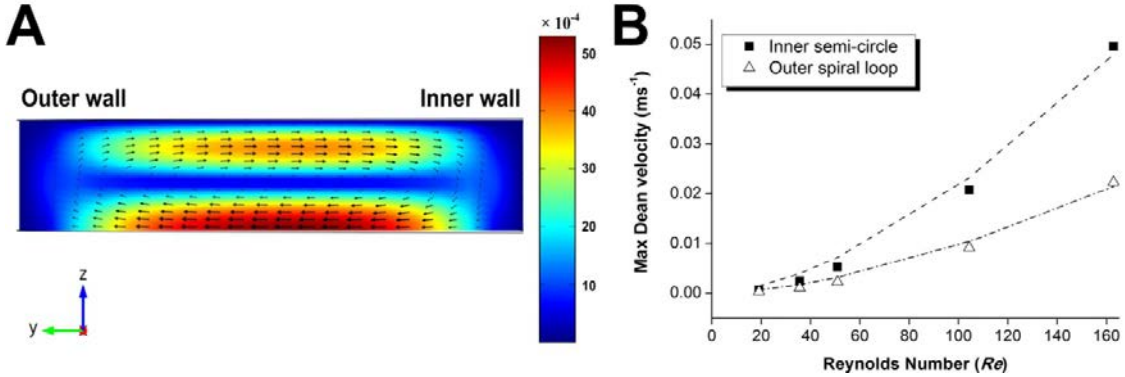

Figure 5.5. Computational modeling of the Dean flow profile in the spiral design. (**A**) Velocity contour plot of the transverse Dean flow at the inner semi-circular channel cross section at Reynolds Number (*Re*) 50. Arrows indicate the well-developed Dean flow pattern across the upper half of the channel cross section. Colour bar represents Dean velocity magnitude (m sec^{-1}). (**B**) Plot indicates the maximum Dean flow velocity at different regions of the spiral device at different *Re*. The data points were fitted with a similar power law equation (with slight modifications) proposed by Ookawara *et al.* [207] which showed good agreement with the fitted curves (dashed lines).

Figure 5.5A presents the simulation results of the Dean flow profile in the spiral channel design. At *Re* 50, there was an apparent formation of a well-developed secondary counter-rotating Dean vortex at the upper half of the channel due to centrifugal acceleration in curvilinear channels. As expected, the maximum Dean velocity was located at the mid plane region due to similar flow direction (inner to outer wall) for the upper and lower Dean vortices (not shown) which resulted in faster lateral fluid flow. To study the change in Dean flow at different *Re*, the maximum Dean velocity at different regions of the spiral device were plotted at various *Re* (Figure 5.5B). These tested flow rates (*Re*) were chosen based on equation (9) to approximate the lateral Dean migration distances which correspond to different Dean cycle (DC). As shown in the figure, the maximum Dean velocity at the inner semi-circle loop was higher than the outer spiral loop at all flow rates due to a smaller radius of curvature (R), which results in higher Dean number (*De*). A non-linear relationship between the transverse Dean velocity and flow rate was also observed in the plot, consistent with previous work reported by Ookawara *et al.* [197, 207]. The data points were then fitted with a power law equation proposed by Ookawara *et al.* [207] with slight modifications in the coefficient to account for the difference in channel geometry used in our work and the computational results showed good agreement with the fitted curves (dashed lines), further confirming the accuracy of the simulation model.

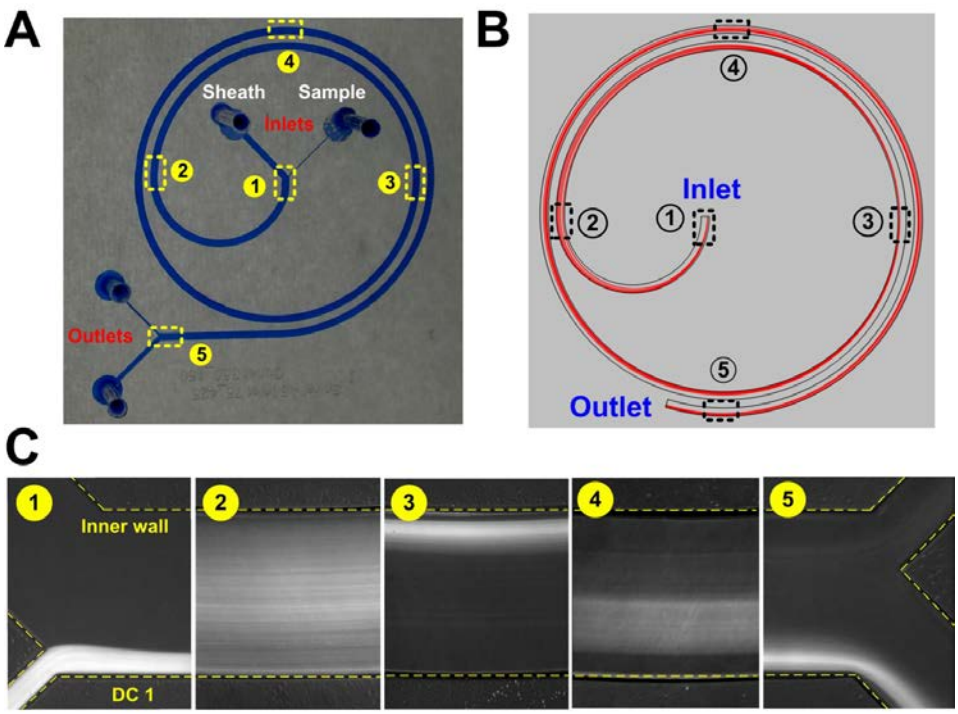

Figure 5.6. (**A**) Photograph of the spiral microchannel fabricated in PDMS (the microchannel is filled with blue dye for visualization). (**B**) Particle tracking (red streamlines) in the modeled spiral device at *Re* 50 (DC 1) showing the lateral migration of the fluid elements at the outer wall region (inlet) towards the inner wall (position 3) and back to the outer wall again (position 5), thus achieving a complete Dean cycle migration at the end of the channel as predicted. (**C**) Average composite fluorescence images illustrating the Dean migration profile along the channel length obtained by flowing 3 µm beads into the spiral device. Corresponding positions of the captured images are indicated in (**A**). Experimental results were in good agreement with the modeled Dean flow pattern at different positions as shown in (**B**). Dashed yellow lines indicate the approximate channel wall boundaries.

After validation of the simulation model, particle tracking function was used to better understand the lateral Dean migration profile in our device. As shown in Figure 5.6B, the flow path of fluid elements located at the outer channel region at the inlet (red streamlines) clearly undergo continuous lateral migration to different positions as they flow along the channel at *Re* 50 (DC 1). Due to the smaller R of the semi-circular channel, a strong Dean vortex was established which resulted in a rapid lateral movement of the red streamlines from the outer wall to inner wall region (position 3). As they continue to flow along the spiral channel, the red streamlines slowly moved back to the outer channel region due to slower Dean migration (larger R) and finally reached the outer wall again by the end of the channel.

This result is indeed consistent to the predicted behaviour of DC 1 in which particles at the outer channel region initially were expected to migrate laterally towards the inner channel and back to outer channel region again at the channel end. This also clearly demonstrates that the calculated flow rate (*Re* 50) employed for DC 1 is a good approximation and sufficient for a complete Dean migration of particles in our channel, which will be crucial for our separation application. To further test if the modeled Dean migration profile was accurate, we added fluorescent 3µm beads into the spiral device at the same flow rate (DC 1) and monitored the positions of the band occupied by the beads along the channel (Figure 5.6C). Since the $a_p/h \leq 0.07$, we expect the beads to solely follow the Dean migration profile with no inertial focusing. Our experimental results showed good agreement with the simulated particle tracking results which confirmed the accuracy of our model and also proved that 3µm beads were only subjected to lateral Dean migration effect within the channel.

5.4.2 Beads characterization at different Dean cycle (DC)

After computational simulation, fluorescent microbeads of different sizes were tested individually to determine the equilibrium focusing positions at different Dean cycle (DC). 15 µm and 6 µm beads were chosen to mimic cancer cells (~15-20 µm in diameter) and RBCs (~6-8 µm) respectively. The flow rates tested were derived from equation (9) which corresponds to different DC based on the lateral Dean migration distance. Images were captured at the 500 µm channel section prior to the outlet bifurcation for analysis. At DC 0.5, the smaller 6 µm beads were entrained in the Dean vortices and solely undergo lateral Dean migration from the outer wall to the inner wall, consistent with our calculated lateral migration distance for DC 0.5. As flow rate increased, the inertial lift forces did not affect migration of the 6 µm beads ($a_p/h \leq 0.07$) and the beads were transposed towards the outer channel again due to stronger Dean flow, resulting in a complete Dean cycle migration back to the outer wall at DC 1 (Figure 5.7A). Further increasing the flow rate caused the beads to recirculate towards the inner half, which is unfavorable for our separation application.

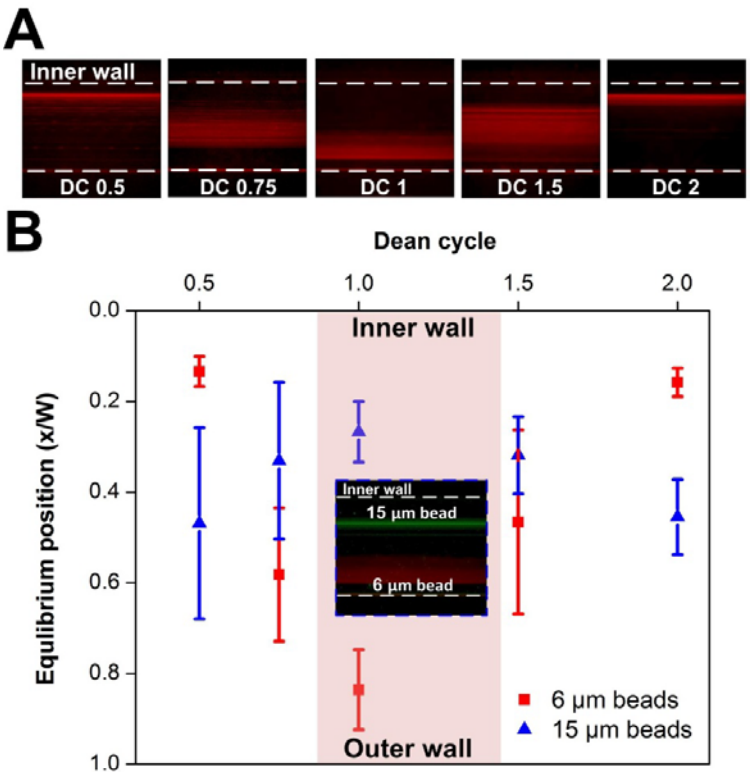

Figure 5.7. Beads characterization of the spiral microfluidic device at different Dean cycle (DC). (**A**) Average composite fluorescence images indicating equilibrium position of 6 µm beads at different DC (white dotted lines indicate the approximate position of the microchannel walls). (**B**) Plot illustrating the position and width of the focusing bands for 6 µm and 15 µm beads at different DC. Focusing band width is determined by measuring the full width at half maximum (FWHM) of the region occupied by the beads. At DC 1, 15 µm beads focused most tightly at the inner wall while 6 µm beads migrated completely to the outer half of the channel, resulting in their complete separation into different outlets. Inset image indicates the distinct equilibrium positions for 15 µm and 6 µm beads in a mixed sample at DC 1.

Next, 15 µm beads were used to study the inertial focusing of the larger particles in our device. To compare the degree of focusing as a function of DC, we measure the equilibrium position and width of the focused band for 15 µm and 6 µm beads separately. The focusing band width is calculated by measuring the full width at half maximum (FWHM) of the region occupied by the beads. As opposed to the smaller beads, 15 µm beads were mostly flowing at the channel centre at DC 0.5 due to stronger lateral drag force acting on the larger particles which resulted in slower Dean migration. At DC 1, the 15 µm beads migrated to the inner channel completely and undergo inertial focusing ($a_p/h \geq 0.07$) to form a narrow band near the inner wall (Figure 5.7B). Above DC 1, the focused band began to stream away from the inner

wall towards the channel centre, consistent with observations reported by others that Dean drag become more dominant than inertial forces at high flow rates due to a decrease in the lift coefficient (C_L) [89]. Optical image (Figure 5.7B) also shows a distinct difference in equilibrium position between 15 µm and 6 µm beads in a mixed sample at DC 1 which resulted in their complete separation using the bifurcated outlet design.

5.4.3 Whole blood characterization

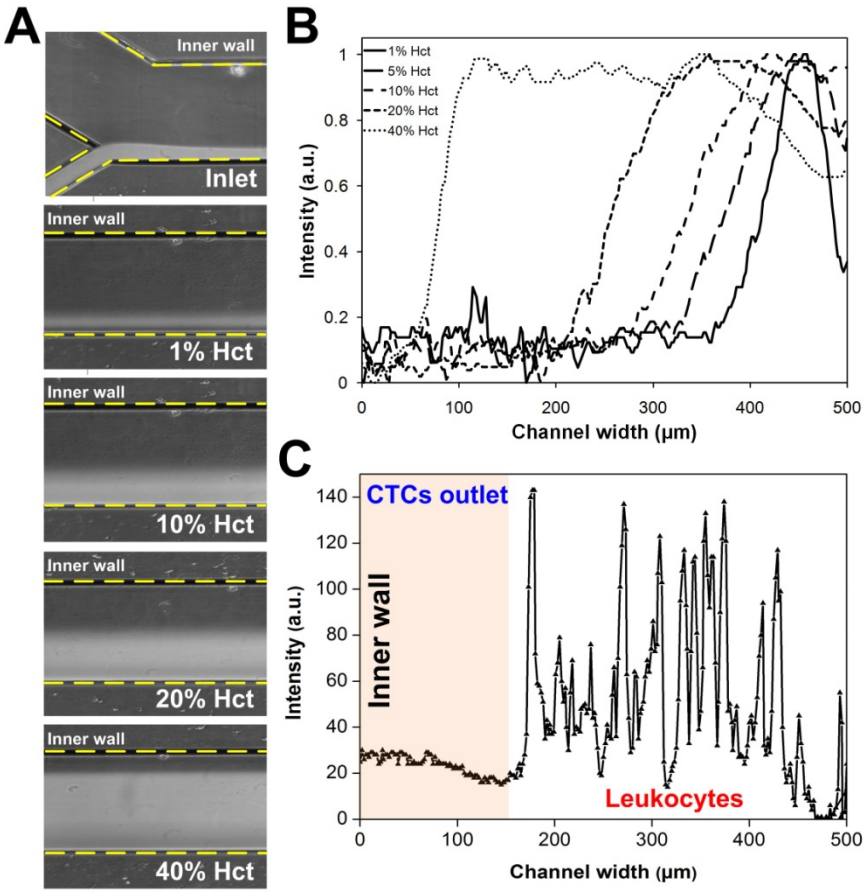

Figure 5.8. Hematocrit and leukocyte characterization of the spiral device at DC 1. (**A**) Averaged composite images illustrating the RBCs occupied region for increasing hematocrit at the outlet. The sample to sheath buffer flow rate was fixed at 1:9. (Dotted lines indicate position of channel walls) (**B**) Plot indicating the width of the RBCs occupied region for increasing hematocrit. (**C**) Linescan indicating the lateral positions of leukocytes at the outlet of the spiral device at DC 1. The larger leukocytes behaved similar to RBCs and were transposed to the outer half of the channel under the influence of Dean drag forces, resulting in minimal leukocytes entering the CTCs outlet (150 µm width).

As RBCs constitute >99% of all the blood cells components, complete RBCs removal will be crucial for efficient isolation of the rare CTCs. After corroboration of the separation principle

using microbeads, RBC samples of varying hematocrit were used to study their equilibrium position at DC 1 to determine the maximum sample hematocrit in which negligible RBCs would enter into the CTCs outlet. Figure 5.8 presents the composite images and linescans for RBCs focusing positions with increasing hematocrit. Similar to 6 μm beads behavior, the smaller RBCs experienced negligible inertial forces and were found at the outer half of the channel after a single Dean cycle migration. As the hematocrit increased, RBC band broadened and the cell-free region width at the inner channel region decreased (Figure 5.8B). This is expected since more RBCs try to occupy the equilibration position at the outer channel which resulted in significant cell-cell interaction induced dispersion. Based on our results, a final hematocrit of 20% was chosen as it gives ~175 μm of cell free region at the channel inner wall and negligible RBCs would enter the CTCs outlet (150 μm). Compared to other inertial-based microfluidic separation methods, 20% hematocrit is considered a major improvement as only ~2× dilution of whole blood (original hematocrit ~40-45%) is required. In terms of throughput, 1mL of whole blood is diluted to 2mL of blood sample which will take ~20 minutes to process (at 100 μL min^{-1}).

Although leukocyte consists of only ~0.1% of all blood cells, it is still overwhelming when compared to CTCs in blood (~10-100 CTCs/mL) and removal of nucleated leukocytes will significantly help reduce the background noise in molecular research such as gene analysis or drug screening. To study the focusing position of leukocytes, a pure sample of leukocytes was pumped through the device at DC 1. Linescan across the channel indicates that leukocytes behaved similar to RBCs and were transposed to the outer half of the channel at DC 1 (Figure 5.8C). As leukocytes are larger in size, they experienced stronger drag forces during the lateral migration and did not migrate completely back to the outer wall at DC 1. Nevertheless, our experimental data clearly shows that the leukocytes were flowing approximately 150-160 μm away from the inner wall and the CTCs outlet bifurcation (150 μm) would ensure minimal leukocytes entering the CTCs outlet, leading to an efficient leukocytes removal.

5.4.4 Cancer cell separation characterization

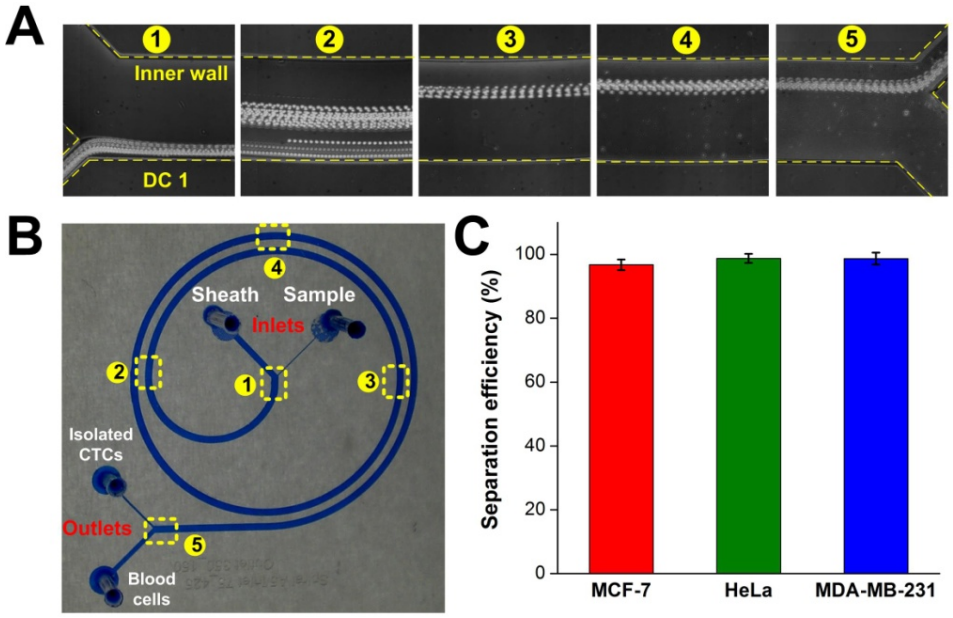

Figure 5.9. Cancer cell separation characterization. (**A**) Average composite images illustrating the focusing position of MCF-7 cells at different locations of the spiral channel at DC 1. (**B**) Photograph of the spiral microchannel fabricated in PDMS (the microchannel is filled with blue dye for visualization). Corresponding positions of the MCF-7 focusing in (**A**) are indicated on the device. (**C**) Plot indicating a high separation efficiency of >95% for different cancer cell lines tested.

Next, we studied the effect of inertial focusing on different cancer cells at DC 1. Figure 5.9 illustrates the focusing position of MCF-7 cells at different locations in the spiral channel. As the cancer cells flowed through the first loop of the spiral channel, the small radius of curvature (R) resulted in strong secondary Dean flows which quickly entrained these cells into the vortices and forced them to migrate laterally towards the inner channel. Similar to 15 µm beads behavior, once the cancer cells reached the inner channel, they experienced significant inertial lift forces as the net lift force acting on the cells is more dominant than the Dean Drag due to the stronger dependence on particle diameter ($F_L \propto a_p^4$ vs. $F_D \propto a_p$) [89, 196]. As a result, the cancer cells focused tightly into a single stream near the inner wall and could be separated into the CTCs outlet at high separation efficiencies of >95% for all cell lines tested (Figure 5.9C).

5.4.5 Cascaded system

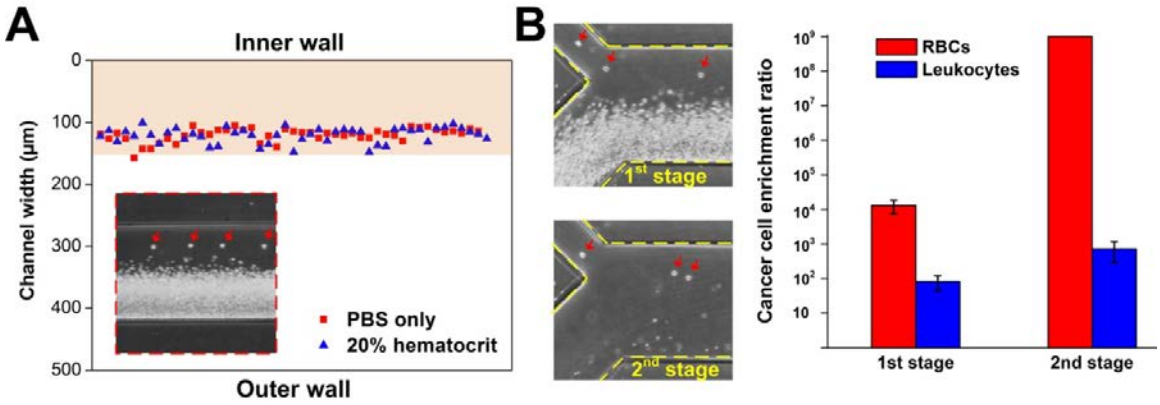

Figure 5.10. Isolation of cancer cells in a 2-spiral cascaded system. (**A**) Plot indicating the focusing positions of MCF-7 cells suspended in PBS solution and 20% hematocrit blood sample. The presence of RBCs did not affect the inertial focusing of cancer cells, leading to their efficient separation into the CTCs outlet (colour highlighted). High speed image (6400 fps) captured at the channel outlet (red dotted box) clearly illustrates the focusing of the larger MCF-7 cells at the inner wall (red arrows) as the smaller RBCs occupy the outer channel region at DC 1. (**B**) Optical images illustrating the separation of MCF-7 cells (red arrows) from 20% hematocrit samples at different stages in the 2-spiral cascaded system. Plot (log scale) indicates a high cancer cell enrichment ratio of 10^9 fold (over RBCs) and ~800 fold (over leukocytes) using the cascaded system.

To demonstrate the separation of cancer cells from blood, we spiked a high number of MCF-7 cells (~10^5/mL) into 20% hematocrit whole blood samples for testing at DC 1. Following separation, flow cytometry analysis using surface markers (EpCAM and CD45) was performed on the sorted samples to quantify CTC recovery from other hematologic cellular components. As shown in Figure 5.10A, the focusing position of MCF-7 cells remained the same in the presence of RBCs, clearly evident that the presence and lateral migration of RBCs did not affect their inertial focusing. High speed imaging also shows the distinct separation between the larger MCF-7 cells and RBCs at DC 1 in our device. Besides single cells, we also spiked multicellular MCF-7 clusters into blood samples for separation as CTCs clusters have been reported to be found in clinical samples and may yield important prognostic significance [84]. Our results also showed successful separation and collection of intact MCF-7 clusters (Figure 5.11). Although a high flow rate was used in our device, the cell clusters did not break up probably due to the short transit time in the channel.

To completely remove RBCs from the sorted CTCs sample, a 2-stage spiral cascade system was set up by connecting the CTCs outlet of the first spiral device to the sample inlet of a second spiral device. This allows subsequent removal of RBCs and leukocytes which have entered the CTCs outlet at the first stage due to RBC-RBCs interactions (Figure 5.10B). Other advantages of the cascaded system include minimal loss of rare CTCs by eliminating manual transfer of sorted CTCs solution to a new device. Moreover, throughput remains the same as both spiral devices operate in tandem. Based on FACS and hemacytometer analysis, a high cancer cell recovery of >90% with enrichment ratio of 10^9 fold (over RBCs) and ~800 fold (over leukocytes) was achieved using the cascaded system. High cell viability (>98%) based on Trypan blue assay was also observed, consistent with others reporting that the high shear rates typically used in inertial-based devices have no adverse effects on the sorted cells [205, 208]. By using a cascaded system, the overall enrichment performance is significantly better than other size-based and affinity-based CTC sorting techniques typically achieving 10^4–10^6 fold enrichment. Using this technique, we can process 1 mL of whole blood in ~20 minutes and recover >90% of the cancer cells. This, to our knowledge, is the fastest processing speed demonstrated in microfluidics systems for continuous CTCs isolation.

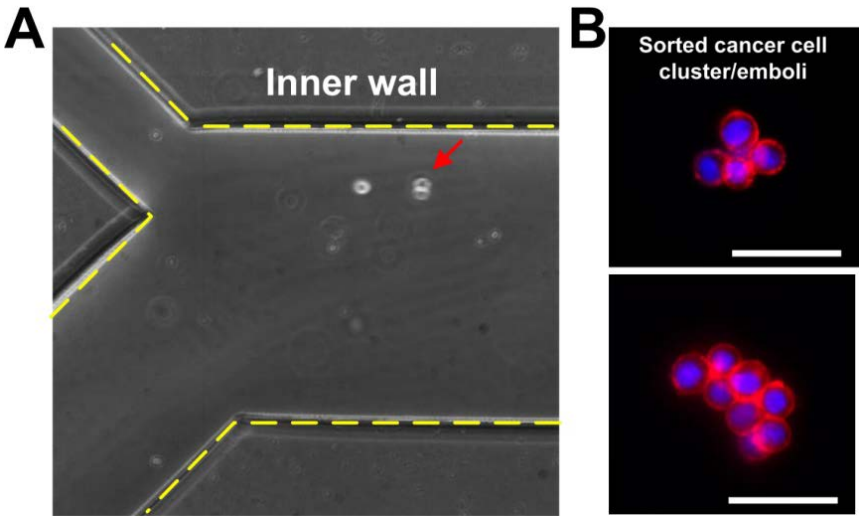

Figure 5.11. Focusing of cancer cell clusters in our device. (**A**) High speed image (6400 fps) indicating inertial focusing of MCF-7 clusters (red arrow) near the inner wall which is similar to the equilibrium positions of focused single MCF-7 cells. (**B**) Images of sorted MCF-7 clusters after passing through our device. The cells were stained with anti-EpCAM antibodies (red) and Hoechst dye (blue) to identify the cell membrane and nucleus respectively. Scale bar is 100 µm.

5.4.6 Downstream assays

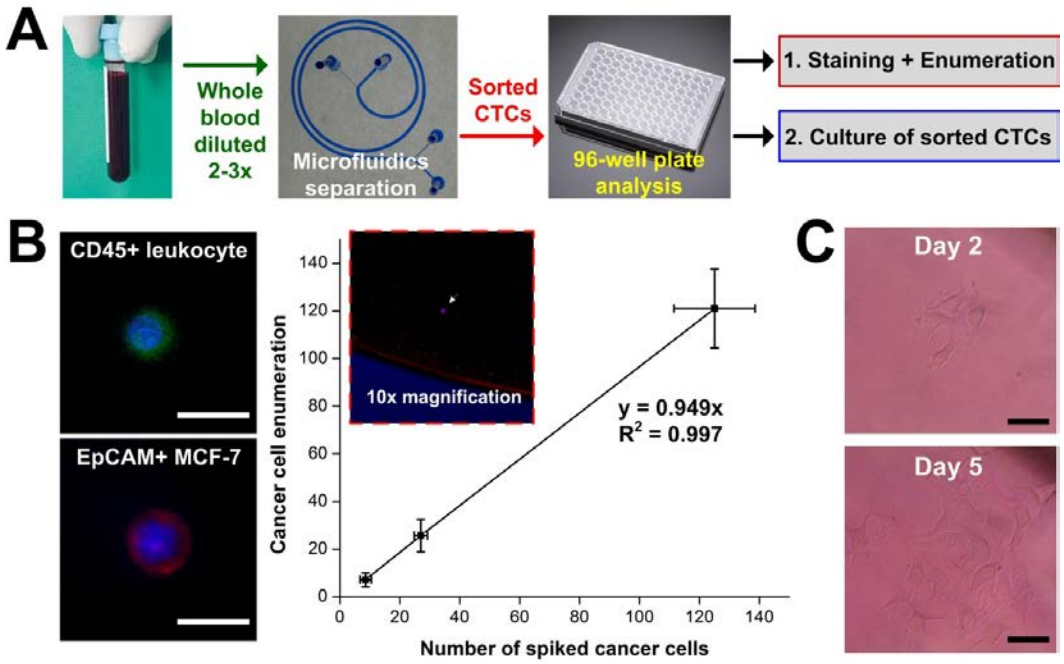

Figure 5.12. Downstream applications using convectional 96-well plate. (**A**) Flow chart illustrating the easy coupling of our microfluidic spiral device with 96-well plate for different downstream applications such as CTCs enumeration and culture of sorted CTCs. (**B**) Optical images of sorted CD45-positive (green) leukocyte and EpCAM-positive (red) MCF-7 cells after immuno-staining on the 96-well plate. Both cell types were stained with Hoechst dye for nuclei identification. Scale bar is 20 µm. Plot indicating a high cancer cell recovery (~95%) on the 96-well plate after sorting blood samples spiked with physiological relevant CTCs concentration (~10-100/ mL). Inset image (red dotted box) shows a stained cancer cell (white arrow) in a well under 10× magnification. (**C**) Images showing successful culture of sorted MCF-7 cells in 96-well plate. Scale bar is 50 µm.

Besides high-throughput processing, another key feature of our separation technique is the ability to continuously collect viable CTCs after separation in a single step which makes it ideal for subsequent biological assays on the sorted CTCs. Only a single blood dilution step is required for sample preparation and we envision the easy coupling of our microfluidic device with convectional 96-well plate for different downstream applications such as CTCs enumeration and culture of sorted CTCs (Figure 5.12A). By transferring the sorted CTCs to each well, different analysis can be readily performed on the plate by lab technicians or clinicians with little training and experience required. To demonstrate CTCs enumeration, we processed 1 mL of blood samples spiked with MCF-7 cells at physiological CTCs concentrations (~10-100/ mL) and performed immunostaining on the sorted cancer cells. The

stained cells were then resuspended in a 96-well plate and enumerated using an epifluoreoscence microscope. As shown in Figure 5.12B, MCF-7 cells can be easily distinguished from the leukocytes based on fluorescence differences. Despite spiking a small number of MCF-7 cells, a high cancer cell recovery (~95%) was achieved in all cases, illustrating minimal cell loss and the potential of our device to process clinically-relevant blood samples. In particular, the high flow rates used in our system might help to minimize settling down of cancer cells in the syringe and tubing, which is an important consideration since CTCs are extremely rare in blood and any CTCs loss will greatly affect the clinical results and evaluations. Lastly, we demonstrated the ability to culture sorted MCF-7 cells using convectional 96-well plate (Figure 5.12C). This is an important application since growth of cancer cells will produce more molecular biomarkers (DNA and proteins) for high-throughput screening or multiplexed molecular assays. Although it is widely known that actual CTCs are hard to survive *in vitro*, future work includes exploring the idea of culturing the rare CTCs from clinical samples using different kinds of extracellular matrix (Matrigel or collagen) coated on the plate to provide a more physiological environment for the CTCs.

5.5 Summary

A major limitation in current inertial-based separation devices is that the blood samples used have to be greatly diluted (~1-2% hematocrit) which increases the processing time, making them unsuitable to process milliliters of clinical blood samples. In this chapter, we presented an ultra high-throughput blood separation technique, termed as "*Dean Flow Fractionation (DFF)*", and applied it for CTCs isolation from blood. The main advantages of this technique is the continuous collection mode of viable sorted CTCs and the ability to process very high hematocrit blood samples (~20%), which is demonstrated for the first time in inertial-based separation devices.

As compared to obtaining fresh tissue biopsy which is often technically challenging and causes great inconvenience, CTCs can constitute as a ‘‘liquid biopsy” which can be carried out routinely in patients due to accessibility and ease of blood collection. More importantly, because primary tumour may not accurately represent the actual metastatic conditions, CTCs also serve as a more representative surrogate tumour biomarker for real-time monitoring of disease status and tailoring personalized therapy [209]. As pointed out in the CTCs Grand Challenge proposed by den Toonder recently [210], handling of large fluid volume and collection of viable CTCs after separation are two key unresolved issues in current CTCs separation methods. The developed device described here not only addresses the aforementioned problems, but because of the size-based separation principle, it can also potentially isolate CTCs that have low EpCAM expression due to epithelial-to-mesenchymal transition (EMT) process.

A growing amount of evidence has shown that subpopulation of carcinoma cells at the primary tumour undergo EMT, resulting in their increased motility which facilitates their intravasations into the blood circulation to form CTCs [173]. More recently, EMT has been associated with stem-like phenotype [211, 212] and this subpopulation of cancer cells, also known as cancer stem cells, are the most resistant to chemotherapy and thus regarded highly important for personalized medicine research [213]. As EMT leads to the down-regulation of epithelial markers (e.g. EpCAM) commonly used for CTCs capture in affinity-binding methods, systems such as CellSearch™ may underestimate the number of CTCs with complete EMT phenotype [214]. Moreover, several clinical studies have shown that some CTCs isolated from peripheral blood also express EMT and stem cell markers [215, 216], which further advocate the importance of using non-EpCAM CTCs enrichment methods (such as size-based separation) for more efficient CTCs isolation. As with any size-based CTC separation technique, a major limitation in this device is its inability to isolate small CTCs (10 -12 μm) when using the current design. This can be easily overcome by optimizing the channel height such that the smaller CTCs can satisfy the $a_p/h \geq 0.07$ criteria. Although

this results in collecting more leukocytes which have overlapping sizes with the smaller CTCs, preventing loss of the rare CTCs would ensure a more accurate CTCs enumeration for clinical evaluations. Furthermore, immunostaining and morphology differences enable easy CTCs identification from the leukocytes, although this method is less useful for downstream applications such as PCR or molecular analyses which are highly affected by large leukocyte background. Future work will therefore include validating the developed microdevice using clinical patient samples to evaluate its potential as a rapid CTCs isolation technique.

In conclusion, the proposed DFF technique offers many distinct advantages over other microfluidic CTCs separation methods. Firstly, the device can process 1 mL of whole blood in ~20 min with >90% CTCs recovery, offering unprecedented ultra-high throughput and separation performance. A short residence time in the device (<10 ms) also significantly shortens the CTCs exposure time to constant shear in the channel, thus minimizing any undesirable shear-induced changes to the CTCs phenotype. Due to simplicity in device setup and operation, lab technicians or clinicians can readily use the microfluidic device in clinical settings with little training and experience required. The large channel dimensions also eliminate clogging issues in the device, thus increasing the sensitivity of CTCs detection with high repeatability. Lastly, the device allows easy collection of viable CTCs after separation in a single step which makes it ideal for coupling with conventional methods such as using a 96-well plate for subsequent biological assays on the sorted CTCs.

6 Conclusions and future work

Enormous progress has been made in cell separation applications using microfluidics, leveraging its many inherent advantages such as high sensitivity and spatial resolution, low sample volume and low device cost. Despite the recent emergence of microfluidic technologies, current microfluidic approaches for blood-based separations suffer from numerous drawbacks including laborious sample preparation, low throughput and clogging issues which often compromise the separation performance.

In this dissertation, we presented several microfluidic cell separation platforms using physical biomarkers (size and deformability) for blood-related diseases including sepsis, malaria and cancer (presence of CTCs in blood). As a result of intracellular molecular and structural changes, diseased cells are often physically different from their normal counterparts in terms of cell size, shape and deformability, which can be readily exploited for cell sorting applications. However, relative abundance and morphology of each diseased cell component varies greatly for different diseases, making it difficult to achieve efficient separation performances using a single cell sorting technique (Figure 6.1). Here, we presented two newly-developed cell separation techniques using 1) cell margination and 2) inertial microfluidics for efficient separation of diseased cells from blood. Cell margination was applied for sepsis and malaria disease which are characterized by the presence of either smaller (bacteria) or stiffer (*i*RBCs) diseased cell components. Inertial microfluidics, on the other hand, was more suited for CTCs isolation from blood due to a large size differences between CTCs and other blood cell components.

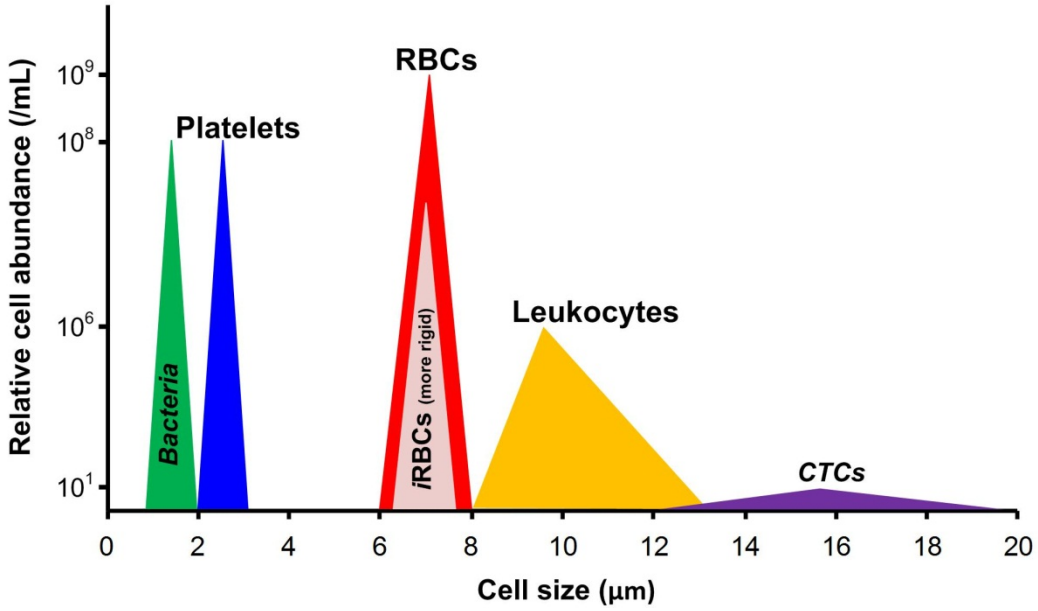

Figure 6.1. Overview of the size and relative abundance of different blood cells in whole blood. Diseased cell components such as bacteria (in sepsis), malaria-infected RBCs (*i*RBCs, in malaria) and CTCs (in cancer) are included in the plot to illustrate the heterogeneity in cell number and morphology in different diseases.

For sepsis, we developed a novel microfluidic technique for non-specific removal of both microbes and inflammatory cellular components from whole blood based on microcirculatory phenomenon such as leukocyte margination and Fahreaus effect. As microbes are smaller but much stiffer than RBCs, we postulate that margination of microbes occurs at high shear conditions due to the formation of a well-defined RBCs core at the channel centre (Fahreaus effect) and hydrodynamic forces arising from intercellular microbe-RBCs interactions. Using a cascaded straight channel design, we demonstrated high removal efficiency of microbes (>80%), platelets and leukocytes (~90%) from whole blood, which can help to modulate the host inflammatory responses and potentially as a blood cleansing method for sepsis treatment. To illustrate multiplexing, we also designed a larger filtration device (6 channels in parallel) to achieve higher throughput (6mL/hr) with similar filtration performance. In the next stage of work, we plan to carry out pilot studies using state-of-the-art models of disease in mice and rats *in vivo* to determine the feasibility of applying the developed blood filtration microdevice as a blood cleansing therapy for sepsis treatment. Unlike conventional tissue culture system,

these rodent models of sepsis will fully reproduce the risk factors and biological effects of sepsis, such as alterations in inflammation, blood pressure/blood flow etc., thus bringing us closer to treatment of human disease.

Besides sepsis, the margination technique was also applied for deformability-based separation of malaria-infected RBCs (*i*RBCs) for rapid *i*RBCs enrichment from whole blood. By using a low aspect ratio microchannel, we showed that the stiffer *iRBCs* were laterally displaced to the channel sides at physiological hematocrit and can be collected for downstream enrichment purposes. The hemodynamic significance of *i*RBCs margination in microcirculation was also demonstrated with another microfluidic device consisting of a capillary-like channel network, which showed an uneven *i*RBCs distribution and sequestration pattern in the capillary network after margination. Future work include coating the capillary channels with endothelial cells or different proteins such as ICAM-1 and CD36 to create a more *in vivo* microenvironment that reproduce both biological (main ligands involved in *i*RBCs cytoadherence) and physical aspects (physiological shear conditions and geometrical constraints) for more accurate cytoadherence studies. Overall, the technique is ideal for on-site *i*RBCs enrichment in resource-limited settings and can be readily applied to other blood cell diseases such as sickle cell anemia and leukemia which are also characterized by changes in cell stiffness. Finally, unlike conventional chemical synchronization methods such as sorbitol or Percoll treatment which are time-consuming and expose *i*RBCs to sub-lytic osmotic stress, the margination technique can also be applied for *i*RBCs synchronization based on intrinsic deformability differences. This will be useful for the malaria community as any undesirable modifications of the ring stage *i*RBCs after synchronization remains an open question and the margination technique may serve as a better alternative as it has the ability to separate out both the late stages (late trophozoites or schizonts) and ring stage *i*RBCs simultaneously.

For CTCs isolation in cancer, inertial microfluidics using straight and spiral channel geometry were employed for continuous, size-based separation of CTCs from whole blood. To work with higher hematocrit blood samples, we first developed a high aspect ratio microchannel patterned with an array of expansion and contraction regions and a "pinching" region at the channel end. By employing high aspect ratio channels, blood cells preferentially equilibrated along the sidewalls due to shear-modulated inertial focusing and the longer channel height also provided more "room" for blood cells to focus, thereby allowing processing of high hematocrit blood samples (~2%). At the pinching region, the larger CTCs were selectively "pinched" to the channel centre upon exit, achieving a high CTCs recovery (>80%) and enrichment factor (~10^{4-5} fold) at the centre outlet.

Lastly, we presented a new CTCs separation technique termed as *Dean Flow Fractionation (DFF)* using a spiral microfluidic device. In this method, the additional Dean vortices due to spiral geometry resulted in the Dean migration of smaller blood components to the channel outer wall as larger CTCs focused at the inner wall due to inertial focusing. The large channel dimensions enable processing of very high hematocrit blood samples (~20%), which is demonstrated for the first time in inertial-based microfluidic devices. In terms of device performance, this translates to processing 1 mL of whole blood under 20 minutes with >90% CTCs recovery. To our knowledge, this is the one of the fastest processing speed demonstrated in microfluidics systems for continuous CTCs isolation. As future work, both developed CTCs isolation techniques would need to be validated using clinical patient samples to evaluate its potential as a CTCs isolation technique.

In conclusion, we have shown that using microfluidic approaches, physical biomarkers can be used to effectively separate different types of diseased cells from blood for diagnostic and therapeutic applications. More importantly, the microfluidic technologies developed in this work clearly address several key issues in current microfluidic blood-related separations.

Firstly, minimal blood sample preparation is required in all techniques, which helps to shorten processing time and reduce loss of rare cells (e.g. CTCs) through minimal human manipulations. Secondly, the developed devices operate at high flow rate which is important for blood processing applications since high flow rates and short processing time would minimize blood contact with “external surfaces” and hence reduce platelets activation/ blood clotting. Moreover, the developed devices only require syringe pumps to operate which significantly simplifies the device setup and operation. This is a key consideration for successful commercialization and implementation in clinical settings as technicians and clinicians should be able to operate the systems with little training and experience required. Finally, as the planar designs facilitate mass fabrication and integration with other microfluidic modules, we envision that with all these aforementioned advantages, the technologies presented in this work will eventually benefit the medical community and contribute in realizing point-of-care (POC) diagnostics.

References

1. Toner, M. and D. Irimia, *Blood-on-a-chip*, in *Annual Review of Biomedical Engineering*. 2005, Annual Reviews: Palo Alto. p. 77-103.
2. Diez-Silva, M., et al., *Shape and Biomechanical Characteristics of Human Red Blood Cells in Health and Disease.* MRS Bulletin, 2010. **35**: p. 382-388.
3. Waugh, R.E. and R.M. Hochmuth, *Mechanics and Deformability of Hematocytes.* 2nd Edition ed. The Biomedical Engineering Handbook, ed. J.D. Bronzino. 2000: CRC Press LLC.
4. Schmid-Schonbein, G.W., Y.Y. Shih, and S. Chien, *Morphometry of human leukocytes.* Blood, 1980. **56**(5): p. 866.
5. Schmid-Schönbein, G.W., et al., *Passive mechanical properties of human leukocytes.* Biophysical journal, 1981. **36**(1): p. 243-256.
6. Haga, J.H., et al., *Quantification of the Passive Mechanical Properties of the Resting Platelet.* Annals of Biomedical Engineering, 1998. **26**(2): p. 268-277.
7. White, J., et al., *Micropipette aspiration of human platelets: influence of microtubules and actin filaments on deformability*. Blood, 1984. **64**(1): p. 210-214.
8. Lipowsky, H.H. *Microvascular rheology and hemodynamics*. in *Spring Symposium on Half a Century of Discovery and Innovation*. 2005. Tokyo, JAPAN: Taylor & Francis Inc.
9. Popel, A.S. and P.C. Johnson, *Microcirculation and hemorheology.* Annual Review of Fluid Mechanics, 2005. **37**: p. 43-69.
10. Pries, A.R., T.W. Secomb, and P. Gaehtgens, *Biophysical aspects of blood flow in the microvasculature.* Cardiovascular Research, 1996. **32**(4): p. 654-667.
11. Fåhraeus, R., *The suspension stability of the blood.* Physiological Reviews, 1929. **9**(2): p. 241-274.
12. Fåhræus, R. and T. Lindqvist, *Viscosity of blood in narrow capillary tubes.* American Journal of Physiology 1931. **96**(3): p. 562-568.
13. Goldsmith, H.L., G.R. Cokelet, and P. Gaehtgens, *Fahraeus, Robin- Evolution of his concepts in cardiovascular physiology*. American Journal of Physiology, 1989. **257**(3): p. H1005-H1015.
14. Pries, A.R., D. Neuhaus, and P. Gaehtgens, *Blood viscosity in tube flow: dependence on diameter and hematocrit.* American Journal of Physiology - Heart and Circulatory Physiology, 1992. **263**(6): p. H1770-H1778.
15. Angus, D.C., et al., *Epidemiology of severe sepsis in the United States: Analysis of incidence, outcome, and associated costs of care.* Critical Care Medicine, 2001. **29**(7): p. 1303-1310.
16. Cohen, J., *The immunopathogenesis of sepsis.* Nature, 2002. **420**(6917): p. 885-891.
17. Beyor, N., et al., *Immunomagnetic bead-based cell concentration microdevice for dilute pathogen detection.* Biomedical Microdevices, 2008. **10**(6): p. 909-917.
18. Snow, R.W., et al., *The global distribution of clinical episodes of Plasmodium falciparum malaria.* Nature, 2005. **434**(7030): p. 214 - 217.
19. Miller, L.H., et al., *The pathogenic basis of malaria.* Nature, 2002. **415**(6872): p. 673-679.
20. Maier, A.G., et al., *Malaria parasite proteins that remodel the host erythrocyte.* Nature Reviews Microbiology, 2009. **7**(5): p. 341-354.
21. Ho, M. and N.J. White, *Molecular mechanisms of cytoadherence in malaria.* American Journal of Physiology-Cell Physiology, 1999. **276**(6): p. C1231-C1242.
22. Lee, G.Y.H. and C.T. Lim, *Biomechanics approaches to studying human diseases.* Trends in Biotechnology, 2007. **25**(3): p. 111-118.
23. Cranston, H.A., et al., *Plasmodium falciparum maturation abolishes physiologic red cell deformability.* Science, 1984. **223**(4634): p. 400-403.

24. Suresh, S., et al., *Connections between single-cell biomechanics and human disease states: gastrointestinal cancer and malaria.* Acta Biomaterialia, 2005. **1**(1): p. 15-30.
25. Paulitschke, M. and G.B. Nash, *Membrane rigidity of red blood cells parasitized by different strains of Plasmodium falciparum.* Journal of Laboratory and Clinical Medicine, 1993. **122**(5): p. 581-589.
26. Shelby, J.P., et al., *A microfluidic model for single-cell capillary obstruction by Plasmodium falciparum infected erythrocytes.* Proceedings of the National Academy of Sciences of the United States of America, 2003. **100**(25): p. 14618-14622.
27. Dondorp, A.M., et al., *Abnormal Blood Flow and Red Blood Cell Deformability in Severe Malaria.* Parasitology Today, 2000. **16**(6): p. 228-232.
28. Dondorp, A.M., E. Pongponratn, and N.J. White, *Reduced microcirculatory flow in severe falciparum malaria: pathophysiology and electron-microscopic pathology.* Acta Tropica, 2004. **89**(3): p. 309-317.
29. Rogerson, S.J., G.E. Grau, and N.H. Hunt, *The microcirculation in severe malaria.* Microcirculation, 2004. **11**(7): p. 559-576.
30. Dondorp, A.M., et al., *Red blood cell deformability as a predictor of anemia in severe falciparum malaria.* American Journal of Tropical Medicine and Hygiene, 1999. **60**(5): p. 733-737.
31. Suresh, S., *Biomechanics and biophysics of cancer cells.* Acta Biomaterialia, 2007. **3**(4): p. 413-438.
32. Cross, S.E., et al., *Nanomechanical analysis of cells from cancer patients.* Nat Nano, 2007. **2**(12): p. 780-783.
33. Lekka, M., et al., *Elasticity of normal and cancerous human bladder cells studied by scanning force microscopy.* European Biophysics Journal with Biophysics Letters, 1999. **28**(4): p. 312-316.
34. Li, Q.S., et al., *AFM indentation study of breast cancer cells.* Biochemical and Biophysical Research Communications, 2008. **374**(4): p. 609-613.
35. Wittekind, C. and M. Neid, *Cancer invasion and metastasis.* Oncology, 2005. **69**(1): p. 14-16.
36. Budd, G.T., et al., *Circulating tumor cells versus imaging - Predicting overall survival in metastatic breast cancer.* Clinical Cancer Research, 2006. **12**(21): p. 6403-6409.
37. Cristofanilli, M., et al., *Circulating Tumor Cells, Disease Progression, and Survival in Metastatic Breast Cancer.* N Engl J Med, 2004. **351**(8): p. 781-791.
38. Hayes, D.F., et al., *Circulating tumor cells at each follow-up time point during therapy of metastatic breast cancer patients predict progression-free and overall survival.* Clinical Cancer Research, 2006. **12**(14): p. 4218-4224.
39. Pantel, K., R.H. Brakenhoff, and B. Brandt, *Detection, clinical relevance and specific biological properties of disseminating tumour cells.* Nature Reviews Cancer, 2008. **8**(5): p. 329-340.
40. Pamme, N., *Continuous flow separations in microfluidic devices.* Lab on a Chip, 2007. **7**(12): p. 1644-1659.
41. Hou, H.W., et al., *Microfluidic Devices for Blood Fractionation.* Micromachines, 2011. **2**(3): p. 319-343.
42. Miltenyi, S., et al., *High gradient magnetic cell separation with MACS.* Cytometry, 1990. **11**: p. 231-238.
43. Bhagat, A., et al., *Microfluidics for cell separation.* Medical and Biological Engineering and Computing, 2010. **48**(10): p. 999-1014.
44. Squires, T.M. and S.R. Quake, *Microfluidics: Fluid physics at the nanoliter scale.* Reviews of Modern Physics, 2005. **77**(3): p. 977-1026.
45. Whitesides, G.M., *The origins and the future of microfluidics.* Nature, 2006. **442**(7101): p. 368-373.
46. Mitchell, P., *Microfluidics - downsizing large-scale biology.* Nature Biotechnology, 2001. **19**(8): p. 717-721.

47. Paguirigan, A.L. and D.J. Beebe, *Microfluidics meet cell biology: bridging the gap by validation and application of microscale techniques for cell biological assays.* Bioessays, 2008. **30**(9): p. 811-821.
48. El-Ali, J., P.K. Sorger, and K.F. Jensen, *Cells on chips.* Nature, 2006. **442**(7101): p. 403-411.
49. Yager, P., et al., *Microfluidic diagnostic technologies for global public health.* Nature, 2006. **442**(7101): p. 412-418.
50. Miura, Y., et al., *Defective osteogenesis of the stromal stem cells predisposes CD18-null mice to osteoporosis.* Proceedings of the National Academy of Sciences of the United States of America, 2005. **102**(39): p. 14022-14027.
51. Li, D.Q., C.S. De Paiva, and S.C. Pflugfelder, *Cell size correlates with phenotype and proliferative capacity in human corneal epithelial cells.* Stem Cells, 2006. **24**(2): p. 368-375.
52. Colter, D.C., I. Sekiya, and D.J. Prockop, *Identification of a subpopulation of rapidly self-renewing and multipotential adult stem cells in colonies of human marrow stromal cells.* Proceedings of the National Academy of Sciences of the United States of America, 2001. **98**(14): p. 7841-7845.
53. Guilak, F., et al., *Viscoelastic properties of human mesenchymally-derived stem cells and primary osteoblasts, chondrocytes, and adipocytes.* Journal of Biomechanics, 2008. **41**(2): p. 454-464.
54. Wang, M.M., et al., *Microfluidic sorting of mammalian cells by optical force switching.* Nature Biotechnology, 2005. **23**(1): p. 83-87.
55. Chen, C., et al., *Design and operation of a microfluidic sorter for Drosophila embryos.* Sensors and Acuators B, 2003. **102**: p. 59-66.
56. Kruger, J., et al., *Development of a microfluidic device for flurescence activated cell sorting.* J. Micromech. Microeng., 2002. **12**: p. 486-494.
57. Berger, M., et al., *Design of a microfabricated magnetic cell separator.* Electrophoresis, 2001. **22**: p. 3883-3892.
58. Inglis, D.W., et al., *Continuous microfluidic immunomagnetic cell separation.* Applied Physics Letters, 2004. **85**(21): p. 5093-5095.
59. Pamme, N. and C. Wilhelm, *Continuous sorting of magnetic cells via on-chip free-flow magnetophoresis.* Lab on a Chip, 2006. **6**(8): p. 974-980.
60. Cheng, J., et al., *Preparation and hybridization analysis of DNA/RNA from E. coli on microfabricated bioelectronic chips.* Nature Biotechnology, 1998. **16**: p. 541-546.
61. Becker, F.F., et al., *Separation of human breast cancer cells from blood by differential dielectric affinity.* Proc. Natl. Acad. Sci., 1995. **92**: p. 860-864.
62. Vahey, M.D. and J. Voldman, *An Equilibrium Method for Continuous-Flow Cell Sorting Using Dielectrophoresis.* Analytical Chemistry, 2008. **80**(9): p. 3135-3143.
63. Vahey, M.D. and J. Voldman, *High-Throughput Cell and Particle Characterization Using Isodielectric Separation.* Analytical Chemistry, 2009. **81**(7): p. 2446-2455.
64. Petersson, F., et al., *Free Flow Acoustophoresis: Microfluidic-Based Mode of Particle and Cell Separation.* Analytical Chemistry, 2007. **79**(14): p. 5117-5123.
65. Evander, M., et al., *Noninvasive Acoustic Cell Trapping in a Microfluidic Perfusion System for Online Bioassays.* Analytical Chemistry, 2007. **79**(7): p. 2984-2991.
66. Chiou, P.Y., A.T. Ohta, and M.C. Wu, *Massively parallel manipulation of single cells and microparticles using optical images.* Nature, 2005. **436**: p. 370-372.
67. Huang, L.R., et al., *Continuous particle separation through deterministic lateral displacement.* Science, 2004. **304**(5673): p. 987-990.
68. Davis, J.A., et al., *Deterministic hydrodynamics: Taking blood apart.* Proceedings of the National Academy of Sciences of the United States of America, 2006. **103**(40): p. 14779-14784.
69. Tan, S., et al., *Microdevice for the isolation and enumeration of cancer cells from blood.* Biomedical Microdevices, 2009. **11**(4): p. 883-892.
70. Mohamed, H., et al., *Isolation of tumor cells using size and deformation.* Journal of Chromatography A, 2009. **1216**(47): p. 8289-8295.

71. Sethu, P., A. Sin, and M. Toner, *Microfluidic diffusive filter for apheresis (leukapheresis).* Lab on a Chip, 2006. **6**(1): p. 83-89.
72. Wilding, P., et al., *Integrated cell isolation and polymerase chain reaction analysis using silicon microfilter chambers.* Analytical Biochemistry, 1998. **257**(2): p. 95-100.
73. Chen, X., et al., *Microfluidic chip for blood cell separation and collection based on crossflow filtration.* Sensors and Actuators B-Chemical, 2008. **130**(1): p. 216-221.
74. Yamada, M., M. Nakashima, and M. Seki, *Pinched flow fractionation: Continuous size separation of particles utilizing a laminar flow profile in a pinched microchannel.* Analytical Chemistry, 2004. **76**(18): p. 5465-5471.
75. Takagi, J., et al., *Continuous particle separation in a microchannel having asymmetrically arranged multiple branches.* Lab on a Chip, 2005. **5**(7): p. 778-784.
76. Maenaka, H., et al., *Continuous and size-dependent sorting of emulsion droplets using hydrodynamics in pinched microchannels.* Langmuir, 2008. **24**(8): p. 4405-4410.
77. Morijiri, T., et al., *Sedimentation pinched-flow fractionation for size- and density-based particle sorting in microchannels.* Microfluidics and Nanofluidics, 2011. **11**(1): p. 105-110.
78. Larsen, A.V., et al., *Pinched flow fractionation devices for detection of single nucleotide polymorphisms.* Lab on a Chip, 2008. **8**(5): p. 818-821.
79. Yamada, M. and M. Seki, *Hydrodynamic filtration for on-chip particle concentration and classification utilizing microfluidics.* Lab on a Chip, 2005. **5**(11): p. 1233-1239.
80. Yamada, M., et al., *Microfluidic devices for size-dependent separation of liver cells.* Biomedical Microdevices, 2007. **9**(5): p. 637-645.
81. Sugaya, S., M. Yamada, and M. Seki, *Observation of nonspherical particle behaviors for continuous shape-based separation using hydrodynamic filtration.* Biomicrofluidics, 2011. **5**(2).
82. Murthy, S.K., et al., *Effect of flow and surface conditions on human lymphocyte isolation using microfluidic chambers.* Langmuir, 2004. **20**(26): p. 11649-55.
83. Nagrath, S., et al., *Isolation of rare circulating tumour cells in cancer patients by microchip technology.* Nature, 2007. **450**(7173): p. 1235-1239.
84. Stott, S.L., et al., *Isolation of circulating tumor cells using a microvortex-generating herringbone-chip.* Proceedings of the National Academy of Sciences, 2010.
85. Gleghorn, J.P., et al., *Capture of circulating tumor cells from whole blood of prostate cancer patients using geometrically enhanced differential immunocapture (GEDI) and a prostate-specific antibody.* Lab on a Chip, 2010. **10**(1): p. 27-29.
86. Choi, S. and J.K. Park, *Continuous hydrophoretic separation and sizing of microparticles using slanted obstacles in a microchannel.* Lab on a Chip, 2007. **7**(7): p. 890-897.
87. Choi, S., et al., *Continuous blood cell separation by hydrophoretic filtration.* Lab on a Chip, 2007. **7**(11): p. 1532-1538.
88. Cho, B.S., et al., *Passively driven integrated microfluidic system for separation of motile sperm.* Analytical Chemistry, 2003. **75**(7): p. 1671-1675.
89. Kuntaegowdanahalli, S.S., et al., *Inertial microfluidics for continuous particle separation in spiral microchannels.* Lab on a Chip, 2009. **9**(20): p. 2973-2980.
90. Yang, S., A. Undar, and J.D. Zahn, *A microfluidic device for continuous, real time blood plasma separation.* Lab on a Chip, 2006. **6**(7): p. 871-880.
91. Hou, H.W., et al., *Deformability based cell margination-A simple microfluidic design for malaria-infected erythrocyte separation.* Lab on a Chip, 2010. **10**(19): p. 2605-2613.
92. Bhagat, A.A.S., et al., *Pinched flow coupled shear-modulated inertial microfluidics for high-throughput rare blood cell separation.* Lab on a Chip, 2011. **11**(11): p. 1870-1878.
93. Martin, G.S., et al., *The Epidemiology of Sepsis in the United States from 1979 through 2000.* New England Journal of Medicine, 2003. **348**(16): p. 1546-1554.

94. Legrand, M., et al., *The response of the host microcirculation to bacterial sepsis: does the pathogen matter?* Journal of Molecular Medicine, 2010. **88**(2): p. 127-133.
95. Harbarth, S., et al., *Inappropriate initial antimicrobial therapy and its effect on survival in a clinical trial of immunomodulating therapy for severe sepsis.* The American Journal of Medicine, 2003. **115**(7): p. 529-535.
96. Valles, J., et al., *Community-acquired bloodstream infection in critically ill adult patients: Impact of shock and inappropriate antibiotic therapy on survival.* Chest, 2003. **123**(5): p. 1615-1624.
97. Neu, H.C., *The Crisis in Antibiotic Resistance.* Science, 1992. **257**(5073): p. 1064-1073.
98. Edmond, K. and A. Zaidi, *New Approaches to Preventing, Diagnosing, and Treating Neonatal Sepsis.* PLoS Med, 2010. **7**(3): p. e1000213.
99. Rimmelé, T. and J. Kellum, *Clinical review: Blood purification for sepsis.* Critical Care, 2011. **15**(1): p. 1-10.
100. Hoffmann, J.N., et al., *Hemofiltration in human sepsis: Evidence for elimination of immunomodulatory substances.* Kidney Int, 1995. **48**(5): p. 1563-1570.
101. Cole, et al., *High-volume haemofiltration in human septic shock.* Intensive Care Medicine, 2001. **27**(6): p. 978-986.
102. Boldt, J., et al., *Volume replacement strategies on intensive care units: results from a postal survey.* Intensive Care Medicine, 1998. **24**(2): p. 147-151.
103. Druml, W., *Metabolic aspects of continuous renal replacement therapies.* Kidney Int, 1999. **56**(S72): p. S56-S61.
104. Moerer, O., et al., *Direct costs of severe sepsis in three German intensive care units based on retrospective electronic patient record analysis of resource use.* Intensive Care Medicine, 2002. **28**(10): p. 1440-1446.
105. Pratt, E.D., et al., *Rare cell capture in microfluidic devices.* Chemical Engineering Science, 2010. **66**(7): p. 1508-1522.
106. Wu, Z.G., et al., *Soft inertial microfluidics for high throughput separation of bacteria from human blood cells.* Lab on a Chip, 2009. **9**(9): p. 1193-1199.
107. Mach, A.J. and D. Di Carlo, *Continuous Scalable Blood Filtration Device Using Inertial Microfluidics.* Biotechnology and Bioengineering, 2010. **107**(2): p. 302-311.
108. Xia, N., et al., *Combined microfluidic-micromagnetic separation of living cells in continuous flow.* Biomedical Microdevices, 2006. **8**(4): p. 299-308.
109. Yung, C.W., et al., *Micromagnetic-microfluidic blood cleansing device.* Lab on a Chip, 2009. **9**(9): p. 1171-1177.
110. Fiebig, E., K. Ley, and K.E. Arfors, *Rapid leukocyte accumulation by spontaneous rolling and adhesion in the exteriorized rabbit mesentery* International Journal of Microcirculation-Clinical and Experimental, 1991. **10**(2): p. 127-144.
111. Goldsmith, H.L. and S. Spain, *Margination of leukocytes in blood flow through small tubes* Microvascular Research, 1984. **27**(2): p. 204-222.
112. Fan, R., et al., *Integrated barcode chips for rapid, multiplexed analysis of proteins in microliter quantities of blood.* Nature Biotechnology, 2008. **26**(12): p. 1373-1378.
113. Jaggi, R.D., R. Sandoz, and C.S. Effenhauser, *Microfluidic depletion of red blood cells from whole blood in high-aspect-ratio microchannels.* Microfluidics and Nanofluidics, 2007. **3**(1): p. 47-53.
114. Shevkoplyas, S.S., et al., *Biomimetic autoseparation of leukocytes from whole blood in a microfluidic device.* Analytical Chemistry, 2005. **77**(3): p. 933-937.
115. Lima, R., et al., *Radial dispersion of red blood cells in blood flowing through glass capillaries: The role of hematocrit and geometry.* Journal of Biomechanics, 2008. **41**(10): p. 2188-2196.
116. Aarts, P., et al., *Blood platelets are concentrated near the wall and red blood cells, in the center in flowing blood.* Arteriosclerosis, Thrombosis, and Vascular Biology, 1988. **8**(6): p. 819-824.
117. Zhao, R., M.V. Kameneva, and J.F. Antaki, *Investigation of platelet margination phenomena at elevated shear stress.* Biorheology, 2007. **44**(3): p. 161-177.

118. Yeh, C. and E.C. Eckstein, *Transient lateral transport of platelet-sized particles in flowing blood suspensions.* Biophysical Journal, 1994. **66**(5): p. 1706-1716.
119. Zhao, R., et al., *Micro-flow visualization of red blood cell-enhanced platelet concentration at sudden expansion.* Annals of Biomedical Engineering, 2008. **36**(7): p. 1130-1141.
120. Turitto, V. and H. Weiss, *Red blood cells: their dual role in thrombus formation.* Science, 1980. **207**(4430): p. 541-543.
121. AlMomani, T., et al., *Micro-scale dynamic simulation of erythrocyte-platelet interaction in blood flow.* Annals of Biomedical Engineering, 2008. **36**(6): p. 905-920.
122. Boulbitch, A., B. Quinn, and D. Pink, *Elasticity of the Rod-Shaped Gram-Negative Eubacteria.* Physical Review Letters, 2000. **85**(24): p. 5246.
123. Huang, K.C., et al., *Cell shape and cell-wall organization in Gram-negative bacteria.* Proceedings of the National Academy of Sciences, 2008. **105**(49): p. 19282-19287.
124. Dulinska, I., et al., *Stiffness of normal and pathological erythrocytes studied by means of atomic force microscopy.* Journal of Biochemical and Biophysical Methods, 2006. **66**(1-3): p. 1-11.
125. Klis, F.M., et al., *Dynamics of cell wall structure in Saccharomyces cerevisiae.* FEMS Microbiology Reviews, 2002. **26**(3): p. 239-256.
126. Smith, A.E., et al., *The mechanical properties of Saccharomyces cerevisiae.* Proceedings of the National Academy of Sciences, 2000. **97**(18): p. 9871-9874.
127. Faivre, M., et al., *Geometrical focusing of cells in a microfluidic device: An approach to separate blood plasma.* Biorheology, 2006. **43**(2): p. 147-159.
128. Adams, M.L., et al., *Polydimethylsiloxane based microfluidic diode.* Journal of Micromechanics and Microengineering, 2005. **15**(8): p. 1517.
129. Stone, H.A., A.D. Stroock, and A. Ajdari, *Engineering flows in small devices.* Annual Review of Fluid Mechanics, 2004. **36**(1): p. 381-411.
130. McDonald, J.C. and G.M. Whitesides, *Poly(dimethylsiloxane) as a Material for Fabricating Microfluidic Devices.* Accounts of Chemical Research, 2002. **35**(7): p. 491-499.
131. Jain, A. and L.L. Munn, *Determinants of Leukocyte Margination in Rectangular Microchannels.* PLoS ONE, 2009. **4**(9): p. e7104.
132. Lima, R., et al., *In vitro blood flow in a rectangular PDMS microchannel: experimental observations using a confocal micro-PIV system.* Biomedical Microdevices, 2008. **10**(2): p. 153-167.
133. Yeh, C. and E.C. Eckstein, *Transient lateral transport of platelet-sized particles in flowing blood suspensions.* 1994. **66**(5): p. 1706-1716.
134. Buras, J.A., B. Holzmann, and M. Sitkovsky, *Animal Models of sepsis: setting the stage.* Nat Rev Drug Discov, 2005. **4**(10): p. 854-865.
135. Sun, C. and L.L. Munn, *Influence of erythrocyte aggregation on leukocyte margination in postcapillary expansions: A lattice Boltzmann analysis.* Physica A: Statistical Mechanics and its Applications, 2006. **362**(1): p. 191-196.
136. Pearson, M.J. and H.H. Lipowsky, *Effect of Fibrinogen on Leukocyte Margination and Adhesion in Postcapillary Venules.* Microcirculation, 2004. **11**(3): p. 295-306.
137. Baskurt, O.K. and H.J. Meiselman, *Blood Rheology and Hemodynamics.* Semin Thromb Hemost, 2003. **29**(05): p. 435,450.
138. Freund, J.B., *Leukocyte margination in a model microvessel.* Physics of Fluids, 2007. **19**(2): p. 13.
139. *World Malaria Report 2008*. 2008, World Health Organization: Geneva.
140. Glenister, F.K., et al., *Contribution of parasite proteins to altered mechanical properties of malaria-infected red blood cells.* Blood, 2002. **99**(3): p. 1060-1063.
141. Nash, G.B., et al., *Abnormalities in the mechanical properties of red blood cells caused by Plasmodium falciparum.* Blood, 1989. **74**(2): p. 855-861.
142. Herricks, T., M. Antia, and P.K. Rathod, *Deformability limits of Plasmodium falciparum-infected red blood cells.* Cellular Microbiology, 2009. **11**(9): p. 1340-1353.

143. Marinkovic, M., et al., *Febrile temperature leads to significant stiffening of Plasmodium falciparum parasitized erythrocytes.* American Journal of Physiology-Cell Physiology, 2009. **296**(1): p. C59-C64.
144. Shevkoplyas, S.S., et al., *Direct measurement of the impact of impaired erythrocyte deformability on microvascular network perfusion in a microfluidic device.* Lab on a Chip, 2006. **6**(7): p. 914-920.
145. Fujiwara, H., et al., *Red blood cell motions in high-hematocrit blood flowing through a stenosed microchannel.* Journal of Biomechanics, 2009. **42**(7): p. 838-843.
146. Ho, M., et al., *Visualization of Plasmodium falciparum-endothelium interactions in human microvasculature: Mimicry of leukocyte recruitment.* Journal of Experimental Medicine, 2000. **192**(8): p. 1205-1211.
147. Safeukui, I., et al., *Retention of Plasmodium falciparum ring-infected erythrocytes in the slow, open microcirculation of the human spleen.* Blood, 2008. **112**(6): p. 2520-2528.
148. Murray, C.K., et al., *Update on rapid diagnostic testing for malaria.* Clinical Microbiology Reviews, 2008. **21**(1): p. 97-110.
149. Wongsrichanalai, C., et al., *A review of malaria diagnostic tools: Microscopy and rapid diagnostic test (RDT).* American Journal of Tropical Medicine and Hygiene, 2007. **77**(6): p. 119-127.
150. Demirev, P.A., et al., *Detection of malaria parasites in blood by laser desorption mass spectrometry.* Analytical Chemistry, 2002. **74**(14): p. 3262-3266.
151. Malhotra, I., et al., *Real-time quantitative PCR for determining the burden of Plasmodium falciparum parasites during pregnancy and infancy.* Journal of Clinical Microbiology, 2005. **43**(8): p. 3630-3635.
152. Doleman, L., et al., *Bioluminescence DNA hybridization assay for Plasmodium falciparum based on the photoprotein aequorin.* Analytical Chemistry, 2007. **79**(11): p. 4149-4153.
153. Grimberg, B.T., et al., *Monitoring Plasmodium falciparum growth and development by UV flow cytometry using an optimized Hoechst-thiazole orange staining strategy.* Cytometry Part A, 2008. **73A**(6): p. 546-554.
154. Stevens, D.Y., et al., *Enabling a microfluidic immunoassay for the developing world by integration of on-card dry reagent storage.* Lab on a Chip, 2008. **8**(12): p. 2038-2045.
155. Moody, A., *Rapid Diagnostic Tests for Malaria Parasites.* Clin. Microbiol. Rev., 2002. **15**(1): p. 66-78.
156. Gascoyne, P., et al., *Microsample preparation by dielectrophoresis: isolation of malaria.* Lab on a Chip, 2002. **2**(2): p. 70-75.
157. Gascoyne, P., et al., *Dielectrophoretic detection of changes in erythrocyte membranes following malarial infection.* Biochimica Et Biophysica Acta-Biomembranes, 1997. **1323**(2): p. 240-252.
158. Zimmerman, P.A., et al., *Diagnosis of malaria by magnetic deposition microscopy.* American Journal of Tropical Medicine and Hygiene, 2006. **74**(4): p. 568-572.
159. Karl, S., et al., *Enhanced detection of gametocytes by magnetic deposition microscopy predicts higher potential for Plasmodium falciparum transmission.* Malaria Journal, 2008. **7**(1): p. 66.
160. Bhagat, A.A.S. and I. Papautsky, *Enhancing particle dispersion in a passive planar micromixer using rectangular obstacles.* Journal of Micromechanics and Microengineering, 2008. **18**(8): p. 9.
161. Cooke, B.M., M. Wahlgren, and R.L. Coppel, *Falciparum malaria: Sticking up, standing out and out-standing.* Parasitology Today, 2000. **16**(10): p. 416-420.
162. Wong, C.W., et al., *Apoptosis: An Early Event in Metastatic Inefficiency.* Cancer Research, 2001. **61**(1): p. 333-338.
163. Weiss, L., *Metastatic Inefficiency*, in *Advances in Cancer Research*, F.V.W. George and K. George, Editors. 1990, Academic Press. p. 159-211.

164. Ashworth, T.R., *A case of cancer in which cells similar to those in the tumors were seen in the blood after death.* Australian Medical Journal, 1869. **14**: p. 146.
165. Hayes, D.F. and J. Smerage, *Is there a role for circulating tumor cells in the management of breast cancer?* Clinical Cancer Research, 2008. **14**(12): p. 3646-3650.
166. Vona, G., et al., *Isolation by size of epithelial tumor cells - A new method for the immunomorphological and molecular characterization of circulating tumor cells.* American Journal of Pathology, 2000. **156**(1): p. 57-63.
167. Zheng, S., et al., *Membrane microfilter device for selective capture, electrolysis and genomic analysis of human circulating tumor cells.* Journal of Chromatography A, 2007. **1162**(2): p. 154-161.
168. Gascoyne, P.R.C., et al., *Isolation of rare cells from cell mixtures by dielectrophoresis.* Electrophoresis, 2009. **30**(8): p. 1388-1398.
169. Adams, A.A., et al., *Highly efficient circulating tumor cell isolation from whole blood and label-free enumeration using polymer-based microfluidics with an integrated conductivity sensor.* Journal of the American Chemical Society, 2008. **130**(27): p. 8633-8641.
170. Xu, Y., et al., *Aptamer-Based Microfluidic Device for Enrichment, Sorting, and Detection of Multiple Cancer Cells.* Analytical Chemistry, 2009. **81**(17): p. 7436-7442.
171. Saliba, A.-E., et al., *Microfluidic sorting and multimodal typing of cancer cells in self-assembled magnetic arrays.* Proceedings of the National Academy of Sciences, 2010. **107**(33): p. 14524-14529.
172. Spizzo, G., et al., *High Ep-CAM Expression is Associated with Poor Prognosis in Node-positive Breast Cancer*. Breast Cancer Research and Treatment, 2004. **86**(3): p. 207-213.
173. Lee, J.M., et al., *The epithelial-mesenchymal transition: new insights in signaling, development, and disease.* Journal of Cell Biology, 2006. **172**(7): p. 973-981.
174. Thompson, E.W., D.F. Newgreen, and D. Tarin, *Carcinoma Invasion and Metastasis: A Role for Epithelial-Mesenchymal Transition?* Cancer Res, 2005. **65**(14): p. 5991-5995.
175. Segre, G. and A. Silberberg, *Radial Particle Displacements in Poiseuille Flow Of Suspensions.* Nature 1961. **189**: p. 209-210.
176. Di Carlo, D., et al., *Continuous inertial focusing, ordering, and separation of particles in microchannels.* Proceedings of the National Academy of Sciences of the United States of America, 2007. **104**(48): p. 18892-18897.
177. Di Carlo, D., *Inertial microfluidics.* Lab on a Chip, 2009. **9**(21): p. 3038-3046.
178. Asmolov, E.S., *The inertial lift on a spherical particle in a plane Poiseuille flow at large channel Reynolds number*. Journal of Fluid Mechanics, 1999. **381**: p. 63-87.
179. Bhagat, A.A.S., S.S. Kuntaegowdanahalli, and I. Papautsky, *Enhanced particle filtration in straight microchannels using shear-modulated inertial migration.* Physics of Fluids, 2008. **20**: p. 101702.
180. Park, J.S., S.H. Song, and H.I. Jung, *Continuous focusing of microparticles using inertial lift force and vorticity via multi-orifice microfluidic channels.* Lab on a chip, 2009. **9**(7): p. 939-948.
181. Zabaglo, L., et al., *Cell filtration-laser scanning cytometry for the characterisation of circulating breast cancer cells.* Cytometry Part A, 2003. **55**(2): p. 102-108.
182. Chun, B. and A.J.C. Ladd, *Inertial migration of neutrally buoyant particles in a square duct: An investigation of multiple equilibrium positions.* Physics of Fluids, 2006. **18**: p. 031704.
183. Bhagat, A.A.S., S.S. Kuntaegowdanahalli, and I. Papautsky, *Inertial microfluidics for continuous particle filtration and extraction.* Microfluidics and Nanofluidics, 2009. **7**(2): p. 217-226.
184. Park, J.S. and H.I. Jung, *Multiorifice Flow Fractionation: Continuous Size-Based Separation of Microspheres Using a Series of Contraction/Expansion Microchannels.* Anal. Chem, 2009. **81**(20): p. 8280-8288.

185. Delamarche, E., et al., *Stability of molded polydimethylsiloxane microstructures.* Advanced Materials, 1997. **9**(9): p. 741-746.
186. Xia, Y. and G.M. Whitesides, *Soft lithography.* Annual Review of Materials Science, 1998. **28**(1): p. 153-184.
187. Gupta, A., et al. *Effect of aspect ratio on inertial migration of neutrally buoyant spheres in a rectangular channel.* in *47th AIAA Aerospace Sciences Meeting*. 2009. Orlando.
188. Lincoln, B., et al., *Deformability-based flow cytometry.* Cytometry Part A, 2004. **59**(2): p. 203-209.
189. Hou, H.W., et al., *Deformability study of breast cancer cells using microfluidics.* Biomedical microdevices, 2009. **11**(3): p. 557-564.
190. Downey, G.P., et al., *Retention of leukocytes in capillaries: role of cell size and deformability.* Journal of Applied Physiology, 1990. **69**(5): p. 1767.
191. Paterlini-Brechot, P. and N.L. Benali, *Circulating tumor cells (CTC) detection: clinical impact and future directions.* Cancer letters, 2007. **253**(2): p. 180-204.
192. Stathopoulos, N.A. and J.D. Hellums, *Shear stress effects on human embryonic kidney cells in vitro.* Biotechnology and Bioengineering, 1985. **27**(7): p. 1021-1026.
193. Dharmasiri, U., et al., *Microsystems for the Capture of Low-Abundance Cells.* Annual Review of Analytical Chemistry, 2010. **3**: p. 409-431.
194. Marrinucci, D., et al., *Case study of the morphologic variation of circulating tumor cells.* Human pathology, 2007. **38**(3): p. 514-519.
195. De Giorgi, V., et al., *Application of a Filtration- and Isolation-by-Size Technique for the Detection of Circulating Tumor Cells in Cutaneous Melanoma.* J Invest Dermatol, 2010. **130**(10): p. 2440-2447.
196. Bhagat, A.A.S., S.S. Kuntaegowdanahalli, and I. Papautsky, *Continuous particle separation in spiral microchannels using dean flows and differential migration.* Lab on a Chip, 2008. **8**(11): p. 1906-1914.
197. Ookawara, S., D. Street, and K. Ogawa, *Numerical study on development of particle concentration profiles in a curved microchannel.* Chemical Engineering Science, 2006. **61**(11): p. 3714-3724.
198. Berger, S.A., L. Talbot, and L.S. Yao, *Flow in curved pipes.* Annual Review of Fluid Mechanics, 1983. **15**: p. 461-512.
199. Sudarsan, A.P. and V.M. Ugaz, *Multivortex micromixing.* Proceedings of the National Academy of Sciences, 2006. **103**(19): p. 7228-7233.
200. Sudarsan, A.P. and V.M. Ugaz, *Fluid mixing in planar spiral microchannels.* Lab on a Chip, 2006. **6**(1): p. 74-82.
201. Mao, X., et al., *Hydrodynamically tunable optofluidic cylindrical microlens.* Lab on a Chip, 2007. **7**(10): p. 1303-1308.
202. Seo, J., M.H. Lean, and A. Kole, *Membrane-free microfiltration by asymmetric inertial migration.* Applied Physics Letters, 2007. **91**(3): p. 3.
203. Gossett, D.R. and D. Di Carlo, *Particle Focusing Mechanisms in Curving Confined Flows.* Analytical Chemistry, 2009. **81**(20): p. 8459-8465.
204. Russom, A., et al., *Differential inertial focusing of particles in curved low-aspect-ratio microchannels.* New Journal of Physics, 2009. **11**: p. 9.
205. Lee, W.C., et al., *High-throughput cell cycle synchronization using inertial forces in spiral microchannels.* Lab on a Chip, 2011. **11**(7): p. 1359-1367.
206. Hur, S.C., et al., *Deformability-based cell classification and enrichment using inertial microfluidics.* Lab on a Chip, 2011. **11**(5): p. 912-920.
207. Ookawara, S., et al., *Feasibility study on concentration of slurry and classification of contained particles by microchannel.* Chemical Engineering Journal, 2004. **101**(1-3): p. 171-178.
208. Mach, A.J., et al., *Automated cellular sample preparation using a Centrifuge-on-a-Chip.* Lab on a Chip, 2011. **11**(17): p. 2827-2834.
209. Punnoose, E.A., et al., *Molecular Biomarker Analyses Using Circulating Tumor Cells.* PLoS ONE, 2010. **5**(9): p. e12517.

210. den Toonder, J., *Circulating tumor cells: the Grand Challenge*. Lab on a Chip, 2011. **11**(3): p. 375-377.
211. Mani, S.A., et al., *The Epithelial-Mesenchymal Transition Generates Cells with Properties of Stem Cells.* Cell, 2008. **133**(4): p. 704-715.
212. Al-Hajj, M., et al., *Prospective identification of tumorigenic breast cancer cells.* Proceedings of the National Academy of Sciences, 2003. **100**(7): p. 3983-3988.
213. Li, X., et al., *Intrinsic Resistance of Tumorigenic Breast Cancer Cells to Chemotherapy*. Journal of the National Cancer Institute, 2008. **100**(9): p. 672-679.
214. Mego, M., S.A. Mani, and M. Cristofanilli, *Molecular mechanisms of metastasis in breast cancer[mdash]clinical applications.* Nat Rev Clin Oncol, 2010. **7**(12): p. 693-701.
215. Theodoropoulos, P.A., et al., *Circulating tumor cells with a putative stem cell phenotype in peripheral blood of patients with breast cancer*. Cancer Letters, 2010. **288**(1): p. 99-106.
216. Aktas, B., et al., *Stem cell and epithelial-mesenchymal transition markers are frequently overexpressed in circulating tumor cells of metastatic breast cancer patients.* Breast Cancer Research, 2009. **11**(4): p. R46.